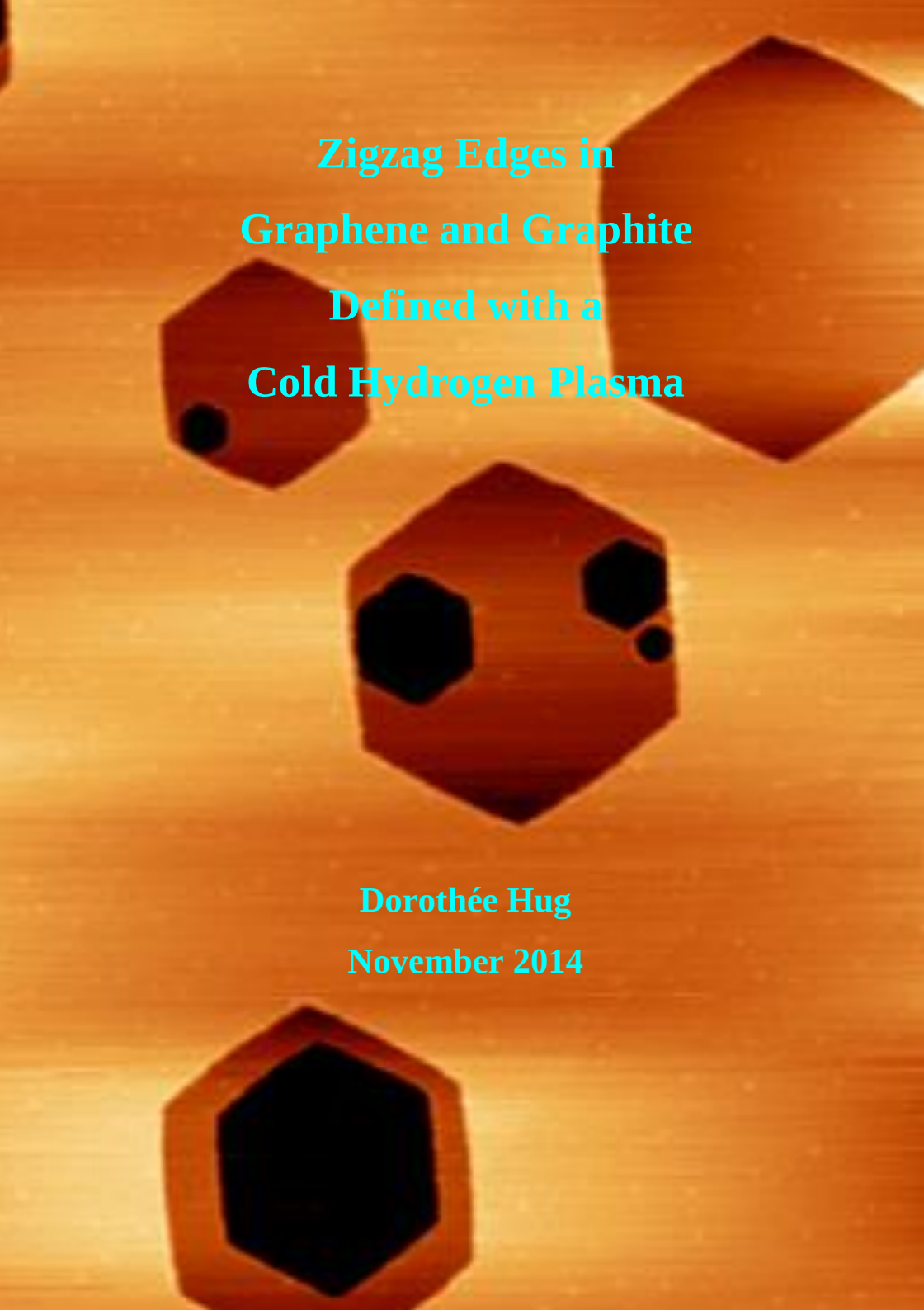

Zigzag Edges in Graphene and Graphite Defined with a Cold Hydrogen Plasma

Dorothée Hug

November 2014

Zigzag Edges in Graphene and Graphite defined with a Cold Hydrogen Plasma

Inauguraldissertation

zur

Erlangung der Würde eines Doktors der Philosophie

vorgelegt der

Philosophisch-Naturwissenschaftlichen Fakultät

der Universität Basel

von

Dorothée Hug

aus **Büchseln, Schweiz**

Basel, 2014

Genehmigt von der Philosophisch-Naturwissenschaftlichen Fakultät auf Antrag von

Prof. L. M. K. Vandersypen

Prof. D. M. Zumbühl

Basel, den 12. November 2013

Prof. Dr. Jörg Schibler (Dekan)

Abstract

Graphene has been considered to be an intriguing playground for novel physics, especially since its isolation ten years ago. For the investigation of the predicted properties of graphene, however, clean samples with crystallographically defined edges are crucial. Here, we explore the interaction of graphite and graphene on silicon dioxide (SiO_2) and hexagonal boron nitride (hBN) substrates with hydrogen ions and radicals in two different pressure regimes, searching for a reliable fabrication method for zigzag edged graphene nanoribbons. The samples are prepared by exfoliating graphite and depositing graphitic material on the substrate of interest. Subsequently the samples are exposed to the plasma at various gas pressures and sample-plasma distances.

Exposing graphite flakes to a pure hydrogen plasma at pressures around 0.03 mbar, leads to the intercalations of hydrogen atoms in between the top graphite layers where the atoms recombine to hydrogen molecules. This process is reversible as the gas molecules can be released from within the substrate when the samples are heated to elevated temperatures. In this regime a partial hydrogenation of the graphite and graphene

surfaces is measured and indicates the formation of graphane. Its band structure is expected to be gapped, opening the way for atomically thin devices employable in electronic industry.

Increasing the gas pressure of the plasma to $0.4-1.7\,\mathrm{mbar}$, the graphitic samples are etched by hydrogen radicals at intrinsic or predefined defects, evolving into hexagonally shaped holes, indicating an anisotropic etching process. The anisotropy of the etching process is, however, strongly dependent on the substrate and the amount of graphite layers exposed. The edges of the hexagons are expected to be of zigzag type and can be employed to fabricate graphene nanoribbons with well define edges. Zigzag graphene nanoribbons were predicted to have magnetic edge states and a band gap, opening the possibility of investigating spin filter devices in graphene structures.

Stimulated by the unanswered question of strongly differing c-axis resistivities (ρ_c) of natural and highly oriented pyrolytic graphite (HOPG), transport experiments, following older investigation, are pursued. Reducing the sample height of natural graphitic flakes to micrometer sized samples, noticeably enlarges its ρ_c, approaching it to the measured HOPG values. A recent theory unveils the discrepancy in ρ_c of natural

graphite and HOPG, linking the density of bulk disorder with the value of ρ_c. The measurement results of the micrometer sized natural graphitic samples with increased ρ_c, distinctly point to a strong influence of the bulk disorder in the graphite flakes on ρ_c, confirming the recent theory put forward.

Acknowledgements

First and foremost my thanks goes to Dominik Zumbühl, who supported and encouraged my experimental work in the last few years. I appreciate greatly the time he spent with me in the lab, explaining to me the measurement setups and the little tricks one can apply for better results. At any time, he enjoyed sharing his profound and considerable knowledge about physics and I appreciated discussions with him truly. It allowed me to learn fascinating physics and widened my knowledge markedly.

I would like to thank Prof. Lieven Vandersypen for his interest in my work and for coming to Basel for my defense.

The ambience in the group is highly motivating in many different ways. I would like to thank Lucas Casparis, Florian Dettwiler, Dario Maradan and Dominikus Koelbl for the good

time in our office. The time we spent enjoying our "after lunch breaks", talking about important and less important political and social issues are as unforgettable as the laughs we had about chocolate marshmallows amongst others. Lucas, I would like to thank you also for being my first and very good master student. I appreciated working with you during this time, as well as later on, when you joined the group as a PhD student. You were always willing to help. Florian, many thanks for all the help with the lock-ins! You were always there, with a lot of patience, to help me check the measurement setup. For the questions about practical work in the lab I had, I would like to thank you Dario. I am also deeply grateful to you for the encouraging words you found for me. Thanks go also to Dominikus for his patience with me, talking about graphene theory: discussing with you was always intense and very instructive. I would also like to thank Christian Scheller, Daniel Biesinger, Lucas and Florian for the helpful inputs concerning IGOR. Really, I saved many hours thanks to you guys. I would further like to thank Myrsini Lafkioti for the fruitful discussion about graphene we had. Simon and Mirko, you accompanied me during the last phase of my PhD and I am very grateful for all the work you

have mastered, leading to some great results. Many thanks to Tai-Min Liu also, who introduced me to Taiwanese cooking style at the grill, I absolutely loved it.

Furthermore, I would like to thank Laurent Marot, Baran Eren and Roland Steiner for the support with the measurements performed at the ESCA3 and the tips for the building of surfatrons. Without the Schönenberger group, something would have been missing! Many thanks go to Romain Maurand, always encouraging and ready for a fruitful conversation about the experimental trouble I encountered. Julia, thank you so much for all the listening you have done. I really enjoyed spending time with you at the university as well as after work. Further I would like to thank Dmitrii Maslov for the conversations we had during BBQ on the physics department roof top and at the rhine. Thanks go also to the mechanics workshop: I always felt welcome and you tried your best to finish the orders we made as quick as possible. Also I would like to thank Barbara Kammermann and Astrid Kalt for helping whenever it was needed.

Last, I would also like to thank Manuel Meng and my family for being highly supportive throughout the last four years. Its thanks to you that this work could be done.

Contents

Chapter 1

Introduction

Graphene has been a well-known theoretical model material, used as a starting point for theoretical investigations of other, more complicated graphitic structures such as graphite and carbon nanotubes [1, 2]. When graphene was isolated and its electrical properties were presented in 2004 by Novoselov and co-workers, the experimental interest in graphene rose quickly [3–5]. Fascinated by the two dimensionality and the possibilities of this newly isolated material, the community interpreted graphene as a possible replacement for the semiconducting devices in the industry. However, the charge carriers of graphene behave, at low density, like massless Dirac fermions, making it a gapless semiconductor, as seen already in early transport measurements[3]: The conductivity in pris-

tine graphene unexpectedly reaches a minimum value, without vanishing at zero charge carrier density. This demonstrates a fundamental impediment for the fabrication of electrical devices, due to the missing "off-state". However, an energy gap of a few tens of meV is predicted by theory, if the two dimensional sheet is cut into ribbons of widths in the range of 10 nm [6–10]. First experiments, measuring the electrical conductivity through graphene nanoribbons of different widths, demonstrated a width dependent transport gap, induced by an interplay of edge disorder and a small band gap opening rather than only through a larger band gap [11–14]. Additionally, the substrate induces charge carrier density modulation throughout the graphene sheet [15]. Considerable investigations of the influence of the edges and the substrate on the transport properties of the charge carriers in graphene need to be conducted before graphene could be used as a material in the semiconducting industry.

It has already been shown that the negative influence of the substrate and polar molecules absorbed to the sample surface on the transport properties of the flakes, can be removed by suspending and current annealing the samples [16, 17]. A similar result is achieved by adding a hexagonal boron nitride

(hBN) flake in between the single layer (SL) graphene and the SiO_2 substrate, lowering the disorder in the samples [18–20]. Attenuating the disorder induced by rough graphene edges, however, is more complex. A reduction of the edge roughness in the graphene nanoribbon samples can be reached by, instead of physically patterning the flakes, chemical means[21–26]. Graphene nanoribbons obtained from un-zipping carbon nanotubes for example or intercalation of graphite flakes and bottom-up approaches, are elaborate chemical procedures, involving several reaction steps and are difficult to implement [21, 22, 26]. The dimensions of as-fabricated ribbons are only a few nanometers in width and a few tens of nanometers in length. Additionally, except for bottom-up approaches, the size of the ribbons fabricated in a chemical approach, is difficult to control. Exposure of graphene flakes to a hydrogen (H) plasma, on the other hand, involves no chemical fluids and the ribbon dimensions are determined by the size and distance between pre-patterned holes on the flake, as well as by the etching time [23–25]. The anisotropic hydrogen radical etching is expected to form crystallographically terminated hexagonal structures at intrinsic or pre-defined defects, allowing the fabrication of zigzag edged ribbons. How-

ever, SL graphene deposited on a SiO_2 substrate is etched isotropically and no reliable etching of SL graphene using an H plasma could be achieved up to date [23, 24, 27]. Hence it is important to understand the interaction of graphitic samples with the H atoms as well as the impact of the substrate on the etching to establish a reliable fabrication process for graphene nanoribbons using an H plasma and, in the end, to allow a gateable current flow through graphene devices.

In this work, graphite and graphene etching in an H plasma is implemented in a home-built plasma enhanced chemical vapor deposition (CVD) oven and the influence of the plasma parameters on the strength and type of chemical etching is investigated systematically. The aim of the work is to gain deeper understanding of the interaction of hydrogen atoms with graphitic surfaces, allowing the tuning of the plasma parameters for the fabrication of crystallographically edged ribbons. The influence of the SiO_2 and the hBN substrates on the anisotropy of the SL and bilayer graphene etching is further investigated, to achieve reliable anisotropic etching of SL graphene flakes. For future experiments on H plasma etched ribbons, changes in the mobility of exposed samples is investigated, to further improve the plasma parameters,

reaching the non-destructive and non-hydrogenating regime.

Another method to induce a band gap in graphene is its hydrogenation. When exposing graphene to the downstream region of an H plasma, the chemical transformation of the graphene flake into graphane through hydrogenation can occur [28]. Graphane has been observed in various experiments, exposing graphene to hydrogen/argon gas mixtures [28, 29]. The parameters influencing the hydrogenation are not clearly known and the process is not fully understood. Due to their larger mass, the argon atoms can cool the H plasma which reduces the amount of H atoms available for the reaction, enlarging the exposure time and hence the probability of damaging the graphene sheet.

The usability of a pure H plasma for the hydrogenation process of graphitic surface is investigated in this work in a metallic plasma chamber. The length of the exposure time is varied, to investigate if full hydrogenation can be performed in this system. Further, graphite exposure to the same plasma is performed, to investigate the hydrogen storage capacity of the material. Subsequent thermal release of the chemisorbed H on graphene and trapped H in graphite samples reveals the usefulness of graphite as hydrogen storage material.

A fundamental difference has been seen between the c-axis resistivity values of natural graphite [30, 31] and highly ordered pyrolytic graphite (HOPG) [32, 33]. However, known theories have not found a satisfying explanation for the contradicting data [34–36]. A new theory has been put forward recently, linking the effects seen in natural graphite and HOPG by comparing the disorder in the two systems [37]. Understanding the difference of ρ_c in HOPG and natural graphite contributes to the resolution of a long-lasting condense matter physics puzzle.

Micrometer sized macroscopic natural graphite and HOPG samples are fabricated and the room temperature (RT) as well as the temperature dependent c-axis resistivity is measured and compared to literature values. The intention of this work is to investigate the dependence of the resistivity of natural graphite and HOPG samples on their size and disorder and give experimental evidence for the theory developed in [37].

This thesis is organised as follows:

- **Chapter 2:** Before starting with the experiments, the theoretical and experimental background to the different subjects is given. In the first part of this chapter, the theoretical properties of graphene are listed. In the second part, an introduction to plasma physics in general, as well as to the generation and characterisation of surface wave plasmas is given. Possible interactions of H atoms in the plasma and chemical reactions with graphitic surfaces is included.

- **Chapter 3:** Measurements of graphene Hall bars are discussed in view of the impact of rough edges and charged inhomogeneities on the transport properties of graphene nanoribbons. Possible sources of charged impurities and the influence of the rough edges are explained.

- **Chapter 4:** The hydrogen etching of graphite and graphene samples is discussed in dependence of the sample-plasma distance as well as the gas pressure. Both parameters were found to have a similar influence on the etching strength and type. The effect of the

SiO_2 and hBN substrates on the anisotropy of SL graphene etching is investigated, clearly demonstrating a reproducible anisotropic etching for hBN, in strong contrast to SiO_2 substrates.

- **Chapter 5:** Influences of the environment on the mobility of SL graphene samples are investigated. Electrical transport measurements at 4.2 K of SL graphene flakes before, after annealing at different temperature in vacuum and in H_2 gas, as well as after H plasma exposure are performed. Annealing in vacuum positively affects the measurements, whereas exposure to H reduces the mobility values. The copper contamination of the quartz tube is assumed to influence the results heavily.

- **Chapter 6:** In this chapter, the influence of a pure H plasma on the hydrogenation process of SL graphene samples is investigated and the formation of graphane is observed. Hydrogen accumulations underneath the first few atomic layers in graphite is examined as well as the thermal release of the gas during annealing at elevated temperatures.

- **Chapter 7:** The c-axis resistivity in dependence of the graphite sample size is investigated for natural graphite, as well as for HOPG, indicating a drastic influence of the sample size on the ρ_c for natural graphite. The temperature dependence of the c-axis resistivity is measured and results are compared to previous experiments. A recent theoretical model of the difference of ρ_c for natural graphite and HOPG adequately describes the results reported.
- **Chapter 8:** Here, future experiments are proposed, on the background of the findings of this thesis.

Chapter 2

Theoretical and Experimental Background

In the following chapter, an overview of the theoretical and experimental background employed in this thesis is given, starting with a summary of the physical properties of graphene, where first its band structure is discussed. The Landau level signature of graphene is addressed before the electrical properties of zigzag and armchair edged graphene ribbons is summarized. Further, the Raman signature of graphene is discussed, its most prominent peaks and their origin. In the last paragraph of this section, the calculations for the mobility of the graphene flakes are explained. The second part of this chapter outlines the generation of surface wave plasmas using a so

called surfatron and the origin and the propagation of surface waves in such systems. Also, the characterisation of plasmas in general is presented, explaining the operation of a Langmuir probe, with which the particle energies and densities in the plasma can be evaluated. In the last part of this chapter, the interaction of the plasma particles with graphitic surfaces is discussed. The different interactions inside and outside of the discharge region is elucidated and a discussion of the recombination processes occurring along the discharge tube, inside and outside the glowing plasma is appended.

2.1 Physical Properties of Graphene

A great portion of the physical properties of graphene, such as the band structure of a 2D graphene sheet [1] as well as its modification upon ribbon fabrication [6] was already known long before its isolation in 2004 by Kostya Novoselov and coworkers [3–5]. Since then, the research interest in graphene has not stopped growing and numerous experimental but also theoretical work has been performed on its subject, deepening our understanding of this exciting material [38, 39].

2.1.1 Graphene Band Structure

From chemistry classes it is known that a carbon atom has four valence electrons in the second shell, whereof three populate the three hybridized sp^2 orbitals, built up by the s and the p_{xy} orbitals, and one resides in the p_z orbital. The sp^2 orbitals of neighboring atoms form strong, in-plane σ bonds and the p_z atomic orbital of neighboring atoms overlap and form two weak π bonds [40]. Charge carriers populating the π (bonding) and π^* (antibonding) bands are fully delocalized over the graphene plane and contribute, in contrast to

the charge carriers in the σ band, to conductivity. Hence, the π-bands contain the information needed to understand the electrical transport properties of graphene in the low energy regime. To calculate the band structure of the π-orbitals the hexagonal lattice of graphene is examined (see Fig. 2.1) [1, 41, 42].

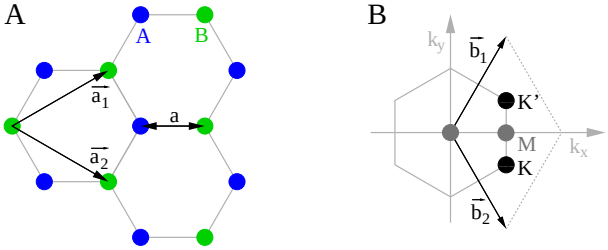

Figure 2.1: The crystal structure of graphene in direct (panel A) and reciprocal (panel B) space, adapted from Ref [43]. Panel A: Graphene lattice in real space with the unit cell, spanned by the two unit vectors $\vec{a}_1$ and $\vec{a}_2$. It contains two atoms, shown in blue and green, therefore two bands are expected in the band structure. The crystal lattice of graphene can be thought of being made by two separate lattices, also called sublattice A and B, each containing a single atom. Panel B: Reciprocal lattice of graphene with the unit vectors $\vec{b}_1$ and $\vec{b}_2$. At the six corners of the first Brillouin zone (grey hexagon in panel B) the valence and conduction band touch each other. Only two corners are inequivalent, namely the K and K' points.

The unit cell of graphene contains two atoms A (blue) and B (green), as shown in Fig 2.1A [1]. In Eq. 2.1a the lattice

vectors for the direct space and in Eq. 2.1b the reciprocal lattice vectors of graphene are displayed,

$$\vec{a}_1 = \frac{a}{2}(3, \sqrt{3}), \qquad \vec{a}_2 = \frac{a}{2}(3, -\sqrt{3}) \tag{2.1a}$$

$$\vec{b}_1 = \frac{2\pi}{3a}(1, \sqrt{3}), \qquad \vec{b}_2 = \frac{2\pi}{3a}(1, -\sqrt{3}). \tag{2.1b}$$

with $a = 0.246\,\text{nm}$ being the distance between neighboring atoms (lattice constant). The total wave function for the p_z orbital in graphene includes the description of both atoms in the unit cell, as described by [1]

$$\Psi = \phi_A + \lambda\phi_B \tag{2.2a}$$

with

$$\phi_A = \sum_A \exp\left[2\pi i\vec{k}\vec{r}_A\right] X(\vec{r} - \vec{r}_A) \tag{2.2b}$$

$$\phi_B = \sum_B \exp\left[2\pi i\vec{k}\vec{r}_B\right] X(\vec{r} - \vec{r}_B) \tag{2.2c}$$

where $\vec{k}$ is the wave vector in k-space, $X(\vec{r})$ are the p_z orbitals of atoms in sublattice A or B and ϕ_A (ϕ_B) is the sum of the wave function of atom A (B) and all equivalent position in the crystal generated by primitive lattice translation [1]. Further, the Hamiltonian considering only nearest neighbor hopping is

given by

$$H = -t \sum_{<i,j>,\sigma} (a^{\dagger}_{\sigma,i} b_{\sigma,j} + a_{\sigma,i} b^{\dagger}_{\sigma,j}), \tag{2.3}$$

where $t \approx 2.8\,\text{eV}$ is the nearest neighbor hopping integral and $a_{\sigma,i}$ ($a^{\dagger}_{\sigma,i}$) annihilates (creates) an electron on sublattice A with spin $\sigma(\sigma = \uparrow, \downarrow)$ on site $\vec{r}_i$ [1]. Solving the eigenvalue problem leads to the energy bands of the following form

$$E_{\pm}(\vec{k}) = \pm t\sqrt{3 + f(\vec{k})} \tag{2.4a}$$

with

$$f(\vec{k}) = 2\cos(\sqrt{3}k_y a) + 4\cos\left(\frac{\sqrt{3}}{2}k_y a\right)\cos\left(\frac{\sqrt{3}}{2}k_x a\right) \tag{2.4b}$$

where a is the lattice constant. The minus sign in Eq. 2.4a describes the valence band (π band) and the plus sign the conduction band (π^* band) [1]. At the six corners of the Brillouin zone the two bands touch at the Fermi energy E_F, making graphene a zero band gap semiconductor (see Fig. 2.2A). In the low energy regime (see Fig. 2.2B), the dispersion relation is linear and the electrons behave similar to relativistic massless Dirac fermions with a velocity of $v_f \approx 10^6 \frac{m}{s}$, 300 times smaller than the speed of light.

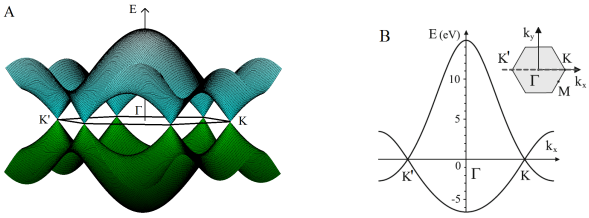

Figure 2.2: Band structure of graphene. Panel A: The conduction band ($\pi*$) is shown in blue, the valence band (π) in green. Only nearest neighbor hopping has been taken into account in the calculation. Adapted from [44]. Panel B: Cut through the band structure in $\vec{k}_x$ direction as shown in the inset. Adapted from [44].

The electronic states in the low energy regime can hence be described with the Dirac equation [1], giving the K and K' points their second name, the Dirac points. The wave vector of graphene in the vicinity of the K point can be written as $\vec{q} = \vec{K} + \vec{k}$, where $\vec{K}$ is the reciprocal lattice vector from the center of the Brillouin zone to the K point and $|\vec{k}|a << 1$ (small $\vec{k}$). The Taylor expansion of $E(\vec{q})$ near the K point results in [1]

$$E_{\pm}(\vec{k}) = \pm v_f \hbar \vec{k} \tag{2.5}$$

with the Fermi velocity $v_f \approx 10^6 \frac{m}{s}$.

The density of states in graphene also shows a linear dependence on energy, given by $D(E) = 2|E|/(\pi\hbar^2 v_F^2)$, and van-

ishes at E_F. Other 2D systems such as electrons confined at the interface of semiconducting heterostructures forming a two dimensional electron gas, have a quadratic dispersion relation leading to a constant density of states [38, 39].

When using the Dirac equation to calculate the low energy states of graphene, the wave function at the K and K' points can be described by a two component spinor, accounting for the two sublattices A and B and the two conical points K and K':

$$\Psi = \begin{pmatrix} \Psi_{KA} \\ \Psi_{KB} \\ \Psi_{K'A} \\ \Psi_{K'B} \end{pmatrix} = \frac{1}{\sqrt{2}} \tag{2.6}$$

Interestingly, the direction of $\vec{k}$ is tightly bound to the amplitude of the sublattice degree of freedom of the particle, meaning that for a certain direction of $\vec{k}$, the particle wave function has a well defined amplitude to be in each of the sublattices (also called pseudospin) [39, 42]. Further, the projection of the direction of this pseudospin onto $\vec{k}$ defines the chirality of the particle. For a parallel alignment of the pseudospin projection on $\vec{k}$, the chirality of the particle is positive and, similarly, for an antiparallel alignment the chirality is nega-

tive. At the K point e.g., all particles in the conduction band have positive, whereas the particles in the valence band have negative chirality. In the K' valley, the particle chiralities are just the inverted [45]. The chirality of the charge carriers in graphene also affects its scattering behavior at potential barriers (Klein tunneling [46]) and its energy quantization in a perpendicular magnetic field, as will be shown in the following.

2.1.2 Landau Levels in Graphene

The charge carriers, flowing through a $3D$ conducting sample, get separated by a perpendicularly applied magnetic field, leading to the generation of a Hall voltage between opposite sides of the sample [47]. In two dimensional electron gas systems, not only a Hall voltage builds up, but also the density of states is influenced by the magnetic field. In a semiclassical picture, the charge carriers are deflected by the Lorentz force and perform cyclotron orbits in the bulk of the sample [45, 48]. However, only orbits enclosing an integer number of flux quanta $\phi_0 = h/e$, are allowed, leading to the quantisation

of the cyclotron radius, which is given by [45, 48]

$$r_c = \sqrt{2n}\ell_B = \sqrt{2n}\sqrt{\frac{\hbar}{eB}} \tag{2.7}$$

where n is an integer value, called the Landau level index, ℓ_B is the magnetic length and B is the magnetic field. This quantization of the charge carrier movement leads to the quantization of the density of states into so called Landau levels (LL). The Landau levels are highly degenerate states and the degeneracy per level, n_{LL}, is B field dependent: $n_{LL} = \frac{|e|B}{h}$. If the charge carrier density is known, the number of filled LLs, namely the filling factor ν, can be calculated by dividing the carrier density by the LL degeneracy: $\nu = \frac{n_D}{n_{LL}}$. The number of filled LLs decreases, at a fixed density, when increasing the value of the applied B-field, as more states are available in each LL. Increasing the charge carrier density, however, increases the number of filled LLs.

The Energy separation between two LLs in a two dimensional electron gas system is given by $E_n = \hbar\omega_c(n+\frac{1}{2})$, $\omega_c = eB/m_e$ being the frequency (cyclotron frequency) of the cyclotron movement of the electrons (mass m_e) in the magnetic field [45, 49]. Between two LLs, no states are available for the

charge carriers and the energy separation increases with the B-field. Hence, the conductivity σ_{xy} does not increase linearly with the applied magnetic field, contrary to the classical Hall effect. σ_{xy} increases in steps with increasing B-field, occurring at values of $\sigma_{xy} = \frac{g_s g_v e^2}{h} \cdot n$, with σ_{xy} measured perpendicularly to the applied current and g_s and g_v being the spin and valley degeneracies of the system (see Fig. 2.3a) [45]. Even though graphene can be described as a $2D$ electron gas system, its quantum Hall effect has a different sequence: it is shifted by $1/2$, appearing at conductivity values of $\sigma_{xy} = \frac{4e^2}{h}(n + \frac{1}{2})$, being a direct consequence of the chiral nature of the charge carriers in the low energy regime of graphene [4, 5, 50].

The reason for the shift can be seen by looking at the Landau level energy for each sublattice as listed in Eq. 2.8 where $E_{A,\pm}(E_{B,\pm})$ is the LL sequence for sublattice A (B) and E_+ describes the electron-like whereas E_- stands for the hole-like LLs [44]. The Landau level index for sublattice A (B) is given by n_A (n_B).

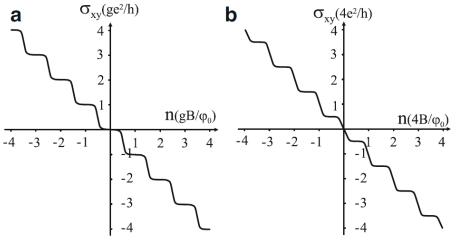

Figure 2.3: The quantization of the conductivity in two dimensional electron gas system (panel a) and single layer graphene (panel b) with degeneracy g and flux quantum $\phi_0 = h/(2e)$ plotted against the filling factor n. The missing of an energy gap in the band structure of graphene allows a direct transition from the valence into the conduction band, leading to the absence of a plateau in the conductivity trace at zero density. Adapted from [44].

$$E_{A,\pm} = \pm\sqrt{2e\hbar v_F^2 B(n_A + 1)}, \qquad \text{for} \qquad n_A = 0, 1, 2, ... \tag{2.8a}$$

$$E_{B,\pm} = \pm\sqrt{2e\hbar v_F^2 B n_B}, \qquad \text{for} \qquad n_B = 0, 1, 2, ... \tag{2.8b}$$

The zeroth Landau level occurs at zeroth energy, for which only Eq. 2.8b has a solution at the K point. Therefore, only sublattice B is populated at the K points at $E = 0$. Calculating the energy levels for the K' points gives the same solutions for the energy levels but with exchanged sublattices. Similarly to the situation just mentioned, solely sublattice A is

populated in the K' valley at zero energy. Hence, only half the states are available in the zeroth LL for both, electrons and holes: each type of charge carrier can only populate one sublattice per valley, leading to the 1/2 shift in the quantization values. Also, the Landau level indices for the different sublattices, n_A and n_B, have different values at the same energy. In other words, particles in different sublattices, A or B, belong to other Landau levels at the same energy. However, every LL in graphene has the same degeneracy of $g = 4$, namely 2 for the valley (K and K') and 2 for the spin ($\uparrow$ and $\downarrow$) of the particles [43–45]. In general, the energy quantization of the Landau levels in graphene is given by [44, 50]

$$E_{n,\pm} = \pm\sqrt{2\hbar|e|Bv_F^2 n} = \pm\hbar\omega_c\sqrt{n} \tag{2.9a}$$

with

$$\omega_c = \sqrt{2}\frac{v_F}{\ell_B} \qquad \text{where} \qquad \ell_B = \sqrt{\frac{\hbar}{|e|B}} \tag{2.9b}$$

ω_c being the cyclotron frequency of graphene and ℓ_B the magnetic length in the system.

With the probed Hall and longitudinal resistivities, the charge carrier density and further, the mobility of the sample can be calculated. The next section lists different possibilities to extract mobility and density values from experimental data.

2.1.3 Mobility evaluation methods

For graphene devices, various ways to calculate their mobilities exist. As for other 2D materials, the mobility can be extracted from (quantum) Hall measurements for samples in the Hall geometry (see **Hall mobility** below). For samples of random shape, on the other hand, the van der Pauw method can be employed to calculate the mobility, as described in **"van der Pauw" mobility**. Further, the field effect is also used as a measure for the mobility in graphene, as the applied back gate voltage is in fact, up to a conversion factor, the charge carrier density (see **Field effect mobility**).

In general, the mobility for a 2D semiconductor is given by [45]

$$\mu = \frac{\sigma_{xx}}{n_D e} \tag{2.10}$$

with n_D being the charge carrier density, e the charge, and σ_{xx} the conductivity of the sample at zero magnetic field.

Using one of the three methods explained below, the electron (hole) density is extracted and utilized to evaluate the mobility of the sample, as performed in chapters 3 and 5.

Field Effect Mobility

The charge carrier density in graphene can be altered by applying a back gate voltage to the graphene sheet. Changing its magnitude, one can tune the charge carrier density from high electron all the way to high hole densities as shown in Fig. 2.4A.

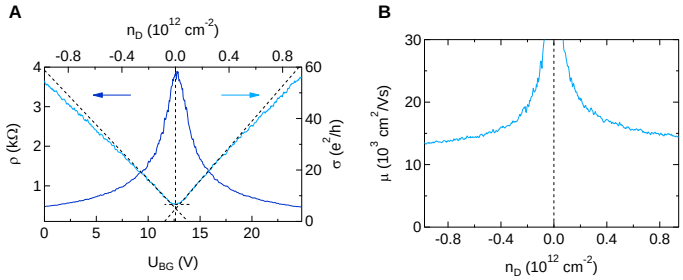

Figure 2.4: A four point measurement of a van der Pauw sample probed at 4.2 K and $B = 0$ T (measurements shown in chapter 5 stem from the same sample). Holes are induced for $n_D < 0$, whereas electrons populate the conduction band for $n_D > 0$.

To calculate the mobility from such a trace, the back gate voltage has first to be converted to a charge carrier density.

Assuming the graphene-SiO_2-Si system to be a parallel plate capacitor [3, 4], the charge carrier density can be written as

$$n_D = \frac{\epsilon_0 \epsilon_r}{ed} \cdot U \tag{2.11}$$

where $\epsilon_0 \approx 8.85..\cdot 10^{-12}\,\mathrm{F/m}$ is the permittivity of free space, $\epsilon_r = 3.9$ the permittivity of SiO_2, e is the unit of charge, $d = 280\,\mathrm{nm}$ the thickness of the oxide and U the effectively applied voltage. As indicated in Eq. 2.11, the charge carrier density has a linear dependence on U. For intrinsic graphene the change from electron to hole density should occur at zero back gate voltage, where the Fermi energy exactly lies in between the valence and conduction band [3]. However, the electron-hole transition is often shifted from $U_{BG} = 0$, displaying the influence of charge fluctuations in the surrounding of the graphene sheet (see Fig. 2.4 and chapter 3 for more details). To calculate the effectively induced charge density at a specific U_{BG}, one has to account for this shift of the Dirac peak by subtracting the voltage U_D, at which the charge carrier transition occurs, from every back gate voltage value U_{BG}: $U = U_{BG} - U_D$. Subsequently, U can easily be transformed into a charge carrier density by using Eq. 2.11. The

mobility can now be calculated using

$$\mu = \frac{1}{\rho_{xx} n_D \cdot e}. \tag{2.12}$$

Due to the transition through zero charge carrier density, $n_D = 0$, the mobility diverges at low n_D, as seen in Fig. 2.4B and relevant μ values are obtained at high n_D only.

Hall Mobility

In Fig. 2.5 a sketch of a Hall bar is shown, together with the voltage and current connections. A current is applied in longitudinal (x) direction and U_{xx} is acquired parallel to the current. The magnetic field B is applied perpendicular to the current direction and the sample plane. Due to the applied magnetic field, the Hall voltage U_{xy} builds up as the electrons get deflected by the Lorentz force $\vec{F_L} = q\vec{v} \times \vec{B}$. An equilibrium value is obtained when the electric field, occurring due to the charge separation, reaches the same magnitude as F_L.

The resistivity ρ_{xx} is then calculated by multiplying the resistance R_{xx} with the ratio w/ℓ, where w is the width and ℓ

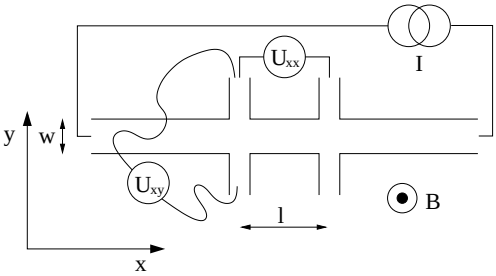

Figure 2.5: Hall configuration to measure the charge carrier density and evaluate their mobility.

the distance between the voltage probes, as shown in Fig. 2.5. Further, U_{xy} is measured perpendicular to U_{xx} in dependence of B_z. Measuring the Hall resistivity $R_{xy} = U_{xy}/I$ enables one to calculate the charge carrier density n_D in the sample for a specific back gate voltage, as n_D is given by

$$n_D = \frac{1}{e}\frac{d\rho_{xy}}{dB}. \tag{2.13}$$

where $d\rho_{xy}/dB$ is the slope to the Hall resistivity plotted against the magnetic field. The slope represents the classical Hall resistivity and is performed in the linear regime of ρ_{xy} as shown in Fig2.6. Hence, Eq. 2.13 results in the charge carrier density at a specific back gate voltage. For the estimation of $n_D(U)$, the calculation of n_D is repeated at several back gate voltages. The charge carrier density is then given by a linear

fit to the calculated n_D values at different U_{BG}.

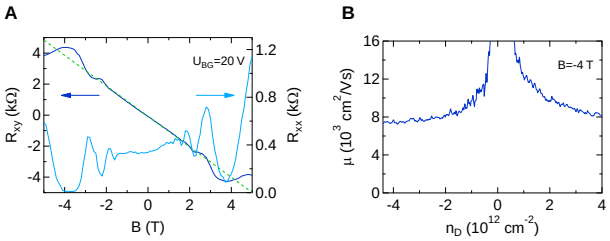

Figure 2.6: Hall and longitudinal resistivity traces, measured at 1.6 K, for the sample shown in chapter 5. The green dashed line is a linear fit to the Hall resistivity and its slope is used for the density calculation. In the right panel the calculated mobility is depicted, indicating high n_D mobilities of around 7500 $cm^2/(Vs)$

The mobility can now be calculated as explained above in the field effect mobility section, using $\mu = (\rho_{xx}|n_D|e)^{-1}$, where ρ_{xx} is the longitudinal resistivity at zero B-field. In Fig. 2.6, a Hall and longitudinal resistivity trace at $U = 0$ are shown in panel A. The measurement stem from the same van der Pauw sample used for the field effect mobility calculations shown in Fig. 2.4. Measurement results of a van der Pauw sample are employed here to depict the mobility calculation using the Hall method. As mentioned below, the van der Pauw results should correspond to the Hall mobility measurements, if density fluctuations in the sample are corrected by averaging several van der Pauw resistivities measurements. How-

ever, the misalignment of the ρ_{xx}-peaks and ρ_{xy} plateaus in Fig. 2.6 could not be corrected as not all relevant traces were measured.

"van der Pauw" Mobility

If the sample has an arbitrary geometry, its dimensions are not easily determined, increasing the difficulty for the calculation of the sample resistivities. With the van der Pauw method, the mobility and charge carrier density of samples with almost any geometry can be well approximated. There are a few constraints, however, which should be considered [51]:

- The sample should be homogenous (constant density) and of uniform thickness
- The sample should by no means contain holes
- The contacts should be placed at the edge of the sample
- The contacts should be small compared to the sample

In Fig. 2.7A an example of a possible sample geometry is shown. Four contacts, A, B, C and D, are positioned at the edge of the sample. The resistivity of such a sample can

be evaluated using [51]:

$$\rho = \frac{\pi d}{\ln(2)} \frac{R_{AB,CD} + R_{BC,DA}}{2} f \tag{2.14}$$

where d is the sample thickness (for 2D samples $d = 1$), f is a proportionality factor, related to $\frac{R_{AB,CD}}{R_{BC,DA}}$ as follows: $cosh\left[\frac{R_{AB,CD}/R_{BC,DA}-1}{R_{AB,CD}/R_{BC,DA}+1}\frac{ln(2)}{f}\right] = \frac{1}{2}exp\left(\frac{ln(2)}{f}\right)$ and depicted in Fig. 2.7B.

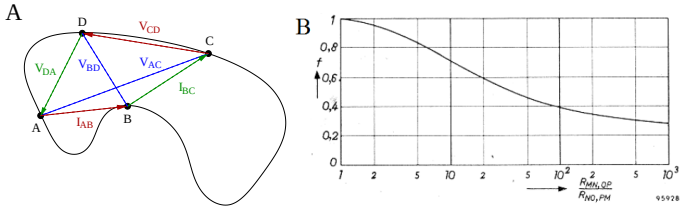

Figure 2.7: van der Pauw sample and proportionality factor f. Panel A: Possible sample geometry for the measurement of the mobility and charge carrier concentration using the van der Pauw method. The points at the edge of the sample represent the contacts. Lines between contacts indicate the measurements performed, in order to acquire the needed data for the mobility and charge carrier density calculations. Panel B: Plottet proportionality factor f. Adapted from [51].

$R_{AB,CD}$ ($R_{BC,DA}$) is the resistance measured by applying a current between contacts A and B (B and C) and measuring the voltage drop from C to D (D to A). To reduce the

effect of charge inhomogeneities in the samples on the resistance measurement, one can apply the reciprocity theorem [52] by exchanging the current and voltage probes ($R_{AB,CD} \rightarrow R_{CD,AB}$), repeating the measurement and averaging both values obtained. Further improvement can be attained by measuring the above mentioned resistivities again, reversing the current and voltage polarities ($R_{AB,CD} \rightarrow R_{BA,DC}$). This reduces influences from thermoelectric (Seebeck) effects, where a temperature gradient in the sample can induce an electric current. Including all the correction measurements, equation 2.14 is modified respectively:

$$\rho = \frac{\pi d}{ln(2)} \frac{R_{vertical} + R_{horizontal}}{8} f \tag{2.15a}$$

where

$$R_{vertical} = R_{AB,CD} + R_{CD,AB} + R_{BA,DC} + R_{DC,BA} \tag{2.15b}$$

$$R_{horizontal} = R_{BC,DA} + R_{DA,BC} + R_{CB,AD} + R_{AD,CB} \tag{2.15c}$$

To evaluate the charge carrier density and the mobility, the Hall voltage

$$V_H = \frac{IB}{en_D} \tag{2.16}$$

has to be measured, where I is the applied current and B the applied magnetic field perpendicular to the current flow and the sample plane. Probing V_H allows one to calculate n_D with which the mobility can be quantified. The current and voltage probes need to be chosen in an alternating way to ensure that the voltage measurement crosses the current paths (see Fig. 2.7A, blue traces). Again, more accurate results are obtained if several contact configurations are measured and averaged. As before, the reciprocity theorem is assumed to hold and one expects the same result for inverted current and voltage probes: $I_{AC}, V_{BD} \rightarrow I_{BD}, V_{CA}$. Furthermore, one should measure the same Hall voltage for reversed polarities of the magnetic field: $V_{AC,p} = V_{AC,n}$, where n (p) is the negative (positive) magnetic field side. Again, the average of all the performed measurements should reduce the influence of charge inhomogeneities in the sample. Therefore, the density is then given by Eq. 2.17

$$n_D = \frac{IB}{e}((V_{AC} + V_{CA} + V_{BD} + V_{DB})/4)^{-1} \tag{2.17}$$

The depicted mobility calculations are employed in the different chapters to evaluate the mobilities of the samples measured.

2.1.4 Graphene Nanoribbons

Graphene nanoribbon are very interesting for the investigation of fascinating quantum phenomena, next to their possible application in semiconducting industry. Armchair (AC) graphene nanoribbons could be employed to investigate spin physics in graphene [53, 54]. Applying a spatially varying magnetic field along the ribbon edge, large Rashba-type spin orbit fields are expected to form, leading to helical modes being robust against edge disorder [53]. Calculations also predict the generation of Majorana fermions in AC nanoribbon devices coupled to an s-wave superconductor, subjected to an alternating in-plane magnetic field [53]. For zigzag (ZZ) ribbons the confinement of the 2D sheet does not induce a band gap. Including the spin degree of freedom and accounting for electron-electron interactions, an antiferromagnetic spin alignment occurs at the ribbon edges [7, 10]. With the help of an in-plane magnetic field (perpendicular to the current

flow), spin filter devices could be fabricated in ZZ edged ribbons [55]. In this subsection the electronic properties of crystallographic AC and ZZ edged ribbons and the influence of disorder on their transport properties are discussed.

Graphene nanoribbons with crystallographic edges

In Fig. 2.8 the two crystallographic edge types of graphene nanoribbons are shown. The AC edge runs along the x-axis and its width is defined by the number of dimer lines N_{AC} along the y-axis. The zigzag axis runs perpendicular to it and its width is given by N_{ZZ}, the number of zigzag lines along the x-axis (see dashed lines in Fig. 2.8A) [6–9]. The dangling bonds at the edge of the ribbons are assumed to be saturated with hydrogen atoms.

Due to the reduced dimension, the $\vec{k}$ vector along the width of the ribbon gets quantized (k_x for the ZZ ribbon, k_y for the AC ribbon in Fig. 2.8A) and only well defined values for the respective $\vec{k}$ vectors are allowed. The number of allowed $\vec{k}$ vectors is directly influenced by the width of the ribbon, namely by N_{AC} or N_{ZZ}, depending on the edge type.

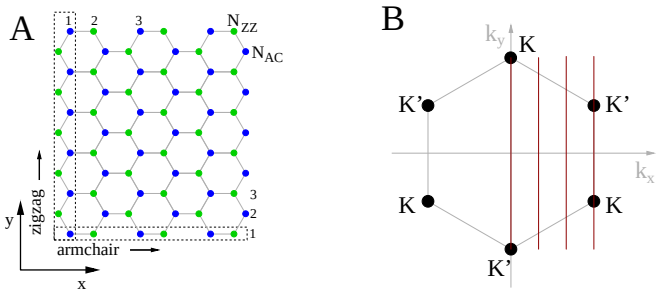

Figure 2.8: PanelA: Illustration of a ZZ and AC ribbon. The direction along the ribbon edges is indicated by the arrows and the zigzag and dimer lines are outlined by the dashed boxes along the respective edges. N_{AC} and N_{ZZ} indicate the number of zigzag and dimer lines along the ribbon widths. Panel B: Upon reducing the width of the 2D graphene sheet to a ribbon, the available states get quantized along the width of the ribbon. Here, the available $\vec{k}_x$ states for a zigzag ribbon aligned along the y direction is shown.

Due to symmetry arguments [56], three different types of ribbons are expected [7]:

$$N_{AC/ZZ} = 3M, \quad N_{AC/ZZ} = 3M + 1, \quad N_{AC/ZZ} = 3M + 2 \tag{2.18}$$

where M is a positive integer, resulting in different ribbon band gaps as seen below.

Armchair Graphene Nanoribbons

AC ribbons with $N_{AC} = 3M + 2$ are metallic (Fig. 2.9(c)) whereas the $N_{AC} = 3M$ and $N_{AC} = 3M + 1$ ribbons show a semiconducting behaviour (Fig. 2.9(b)) with almost the same width dependence of the energy gap [6, 7, 9]. However, applying a local density approximation method for the calculation of the gap and including the spin degree of freedom (LSDA), the width dependence is different for every type of armchair ribbon and none is metallic anymore [9]. The induced band gap clearly depends on the ribbon width and is in the range of a few tens of meV for ribbons of experimentally achievable widths [8, 9].

Zigzag Graphene Nanoribbons

The band structure of zigzag ribbons, as shown in Fig. 2.9(a), does not show any band gap, independent of the number of zigzag lines, when using the tight-binding approximation for the calculations. However, as visible in Fig. 2.9(a), flat bands appear in the region between the K and K' points, indicating strongly localized states at the edge of the ribbons [6–9]. Interestingly, investigations of the band structure by LSDA

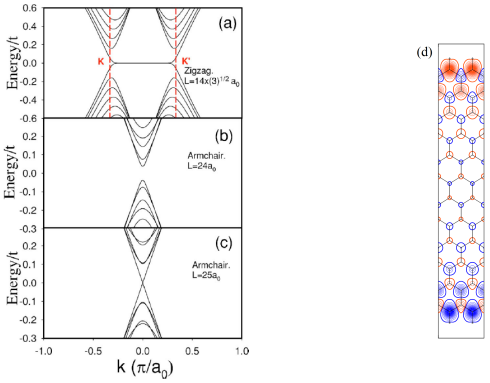

Figure 2.9: Band structure for ZZ and AC graphene nanoribbons and spin alignment in a ZZ edged ribbon. Panel (a): Band structure of a ZZ ribbon, depicting the flat bands appearing between the K and K' points. Panel (b) and (c): width dependence of the band gap induced into AC graphene nanoribbons. Panel (d): Localized electron density at the lattice sites of a ZZ ribbon. The size of the circles indicate the strength of the localization whereas the color indicates the orientation of the spin. Left panel: Adapted from Ref. [9]. Right panel: Adapted from Ref. [8]

and including electron-electron interactions, induces antiferromagnetic spin ordering at opposite edges of the ribbon and a band gap[9]. In Fig. 2.9(d) the spin density for spin up (blue) and spin down (red) are shown, indicating the antiferromagnetic alignment. The spin states decay exponentially inside the ribbon bulk (see Fig. 2.9(d) and caption of Fig. 2.9). Further, the strength of the antiferromagnetic coupling be-

tween the edges does depend on the width of the ribbon and increases for smaller ribbon widths [9].

Both types of ribbons show interesting properties for further investigations: obviously, the band gap induction in AC ribbons is a high priority goal, if graphene should be used for electronic applications. However, also fundamental research topics such as Majorana Fermions could be addressed in AC ribbons in the presence of an alternating magnetic field at the ribbon edge [53]. Further, spin polarisation using ZZ edged ribbons could open the way to investigate spin physics in graphene [55].

Graphene Nanoribbons with Edge Disorder

The theoretical predictions mentioned above assume ribbons with perfect edges. With the established fabrication methods (e-beam lithography and RIE), however, no crystallographically edged ribbons can be produced and their minimum widths are limited to the resolution limits of the e-beam lithography process ($\approx 15\,\mathrm{nm}$) [57–59]. However, calculations have also been done on such ribbons [14, 60], indicating a strong influence of disordered edges on the electrical trans-

port. Even a small amount of edge roughness reduces the conductance at low charge carrier densities by a few orders of magnitude [11, 60]. The reduction in conductance could have several reasons: constrictions along the graphene nanoribbon locally reduce the number of conductance channels available as the charge carriers get localized at the ribbon edge. Hence, the ribbon decays into small quantum dots, increasing the resistance of the ribbon at low charge carrier densities [14]. Another explanation for the reduced conductance includes a small, width dependent band gap and the varying potential landscape (electron-hole puddles) due to the underlying SiO_2 substrate [15, 61]. Together, they form a landscape of quantum dots of a few tens of nanometers in diameter, in which electrons or holes are locally confined [15]. To reduce their influence on the transport measurement through the ribbon, high carrier densities are needed [61].

To investigate the quality and the number of layers of a sample, Raman measurements are extremely useful: disordered samples have a distinct Raman signature compared to clean graphene flakes. In the next section, the most important features of Raman traces for clean and disordered single layer flakes are explained.

2.1.5 Raman Signature of Graphene

Detection of SL graphene using only optical microscopy is time consuming as the visibility of single layer graphene strongly depends on the SiO_2 thickness [62, 63]. Also, experience is needed to see the difference between a single layer (SL) and a bilayer (BL) flake. Atomic force microscopy (AFM) is often used to confirm the choices made beforehand with the optical microscope. Even thought step heights of a few Ångstroms can be resolved with an AFM, a clear distinction between SL and BL flakes is not straight forward, as adsorbed water [64] or PMMA residues [65] can change or blur the effective height of a graphene flake. The features in the Raman traces of SL and BL flakes, on the other hand, can more clearly be discerned, indicating with more certainty the number of layers and the quality of the flake as shown below [66–68].

The Raman signal of a sample is acquired by shining a laser onto the graphene flake surface and measuring the inelastically scattered light from the sample. The positions of the Raman peaks depend on the activated vibrational states of the molecules in the sample and the energy of the laser. For

defect free graphene two prominent peaks are measured: the G-peak at around $1580\,\mathrm{cm}^{-1}$ and the second order $2D$-peak at a Raman shift of about $2710\,\mathrm{cm}^{-1}$ [66]. The G-peak is the only first order process peak in the defect free Raman spectrum of graphene. It is associated with a doubly degenerate E_{2g} breathing mode vibration, activated by an in-plane transverse optical (iTO) or an in-plane longitudinal optical (iLO) phonon (see Fig. 2.10A) [67]. In Fig. 2.10B, the first order Raman process is shown: (i) an electron of wave vector $\vec{k}$ absorbs a photon and an electron-hole pair is generated, (ii) the electron is inelastically scattered by a phonon (iTO or iLO) with wave vector $\vec{q} = 0$ and finally, (iii) the electron-hole pair recombines and emits a photon.

The $2D$-peak, on the other hand, is a double resonance process (second order) and the most important peak to discern a SL from a BL graphene sheet. It involves both, the K and K' points in the reciprocal lattice and is therefore an intervalley process. In Fig. 2.12A the double resonance process of the $2D$ peak measured for a SL graphene sheet is shown: (i) generation of an electron-hole pair, (ii) inelastic scattering of the electron by a phonon with wave vector $\vec{q}$, (iii) inelastic back scattering of the electron by another phonon with wave vec-

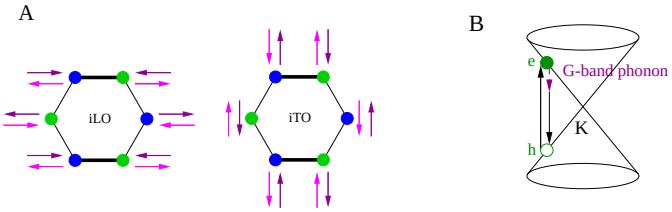

Figure 2.10: Panel A: Here, the iTO and the iLO phonon modes are shown. The transverse and longitudinal directions are generally defined with respect to the nearest neighbor connections and correspond in this image to atomic movements perpendicular or parallel to the bold AB carbon-carbon bond shown, respectively [67]. Panel B: The scattering process occurring for the G-peak signature are shown. The purple arrow indicates the inelastic scattering between an electron and a phonon. Adapted from [67]

tor $-\vec{q}$ and (iv) recombination of the electron-hole pair. The peak is expected to consist of a single Lorentzian, in stark contrast to the $2D$ peak of BL graphene. BL graphene has two π (π^*) bands near the Dirac point, both involved in the scattering processes as shown in Fig. 2.11. Hence, four different electron-phonon interactions can take place, hence four peaks at slightly shifted energies ($2650 - 2725\,\mathrm{cm}^{-1}$) which add up to the BL $2D$-peak are expected [66, 67]. Therefore, the BL $2D$ peak is presumed to be fitted by four Lorentzian shaped peaks forming the $2D$ line shape seen in the inset of panel B in Fig 2.14 [66, 67].

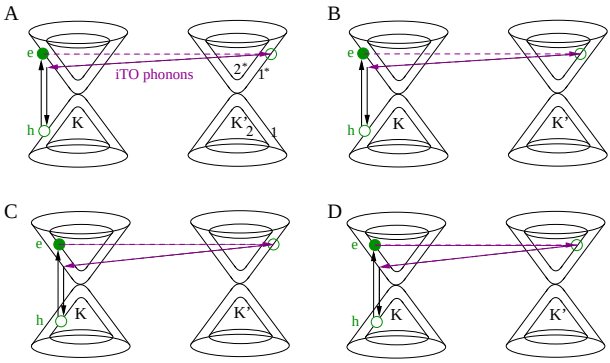

Figure 2.11: Double resonance process occurring in a bilayer graphene flake. The dispersion relation for bilayer graphene is parabolic and in the low energy regime two valence (1 and 2) and conduction bands (1^* and 2^*)are present. Hence, four different double resonance processes can occur: $\pi_1(K) \rightarrow \pi_1^*(K) \rightarrow \pi_1^*(K')$ (panel A), $\pi_1(K) \rightarrow \pi_1^*(K) \rightarrow \pi_2^*(K')$ (panel B), $\pi_2(K) \rightarrow \pi_2^*(K) \rightarrow \pi_1^*(K')$ (panel C) and $\pi_2(K) \rightarrow \pi_2^*(K) \rightarrow \pi_2^*(K')$ (panel D). All four resonances lead to a Raman peak, forming the $2D$ Raman peak for bilayer graphene. Adapted from [67].

For defective SL graphene additional peaks show up in the Raman spectra. At $1350\,\mathrm{cm}^{-1}$ the D-peak arises, being the first order peak of the $2D$-peak and is also a double resonance, intervalley process (see Fig. 2.12B) [69]. However, here, the double resonance needs the presence of a defect for the electron to be inelastically scattered by a phonon. Next to the D-peak, also a D'-peak arises at $1600\,\mathrm{cm}^{-1}$ if defects are present in the sample. Again, it is a double resonance process but,

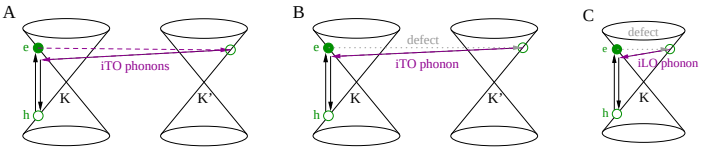

Figure 2.12: Panel A: the $2D$-peak signature arises due to the inelastic scattering processes involving two iTO phonons. No defect is needed for the intervalley scattering to occur, hence it is always visible in Raman spectra of graphene. The D-peak (Panel B) as well as the D'-peak (Panel C) require the presence of defects [67]. The grey dashed lines display scattering of electrons at defects, the purple dashed lines scattering of electrons at phonons. Adapted from [67].

in contrast to the D-peak, it is due to intravalley scattering, as only one Dirac cone is involved (see Fig. 2.12C) [67]. Such processes arise at AC and disordered edges or at defect sites in the bulk of the graphene sample. A defect can be e.g. a vacancy in the graphene lattice or broken π-orbital networks, as observed at hydrogenated carbon atoms [28]. Hence, the D and D'-peaks contain information about the quality of the graphene flake, as the peak intensity is proportional to the amount of disorder in the sample.

Furthermore, one can investigate the type of edge of the graphene flake or ribbon: only the AC edge is expected to show a D-peak, whereas at perfect ZZ edges, no D-peak is

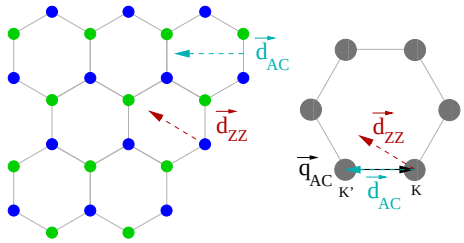

Figure 2.13: Angle dependence of the G peak. In the real space (left side), the defect back-scattering wave vector is shown. The back-scattering wave vector must be perpendicular to the graphene edge to fulfill back scattering conditions [70]. In the reciprocal space (right side), one can see that only the defect wave vector $\vec{d_{AC}}$ for the armchair edge connects the K and K' points, leading to an intervalley scattering.

seen [70]. First, an electron-hole pair is generated by the incoming light and the electron is scattered by a phonon with wave vector $\vec{q}$, see Fig. 2.13. For the generation of a D-peak, the electron needs to be back-scattered by a defect with wave vector $\vec{d} = -\vec{q}$. Further, $\vec{q}$ must connect two different cones in the reciprocal space, K and K' which is only ensured for the armchair edge, as seen in Fig. 2.13. For the ZZ edge however, intervalley scattering can not occur as the wave vector connects two K (K') points, not fulfilling the intervalley conditions needed for the D-peak. Hence, no D-peak is expected to arise for a perfect ZZ edge. Nevertheless, a D'-peak should be measured for both type of edges, due to the intravalley

type of scattering, involving only one of the cones. The angle dependence of the D-peak can also be understood with Fig. 2.13 [71]: varying the polarization angle of the incoming light changes the direction of $\vec{q}_{AC}$, leading to a increase of the D-peak signal whenever a phonon vector is available for backscattering [67].

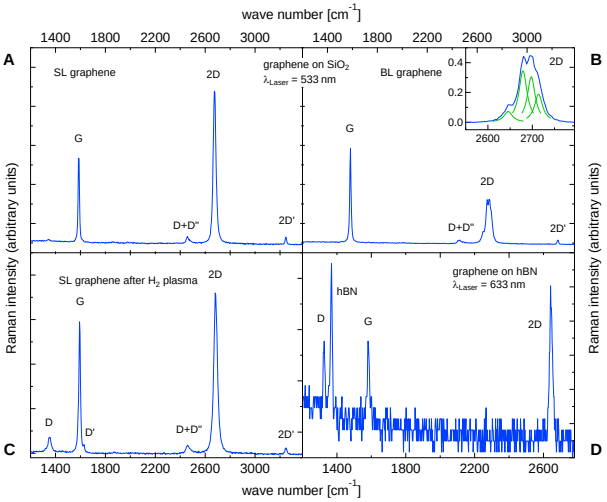

Figure 2.14: Raman traces of graphene flakes. Raman measurement in the bulk region of a pristine SL (panel A) and BL (panel B) graphene flake, employing a 533 nm laser and an laser power of 2 W. Panel C: Raman measurement in the bulk of a SL graphene flake exposed to a H plasma at 0.03 mbar. Panel D: Raman trace at the edge of a graphene flake on hBN, exposed to an H plasma at 0.47 mbar.

In Fig. 2.14 Raman traces for different graphene samples are shown, depicting the relevant peaks to determine the number of graphene layers and the quality of the samples. The traces were acquired using a green (533 nm, panels A-C) or a red (633 nm, panel D) laser (spot size $\approx$ 300 nm) at a power of 2 mW. The position of the D and $2D$ peaks change with the laser wave length [69]. The reason for this dispersive behavior can be found in the double resonance nature of the scattering processes, where the phonon rather interacts with an electron with a $\vec{k}$ vector being half the phonon wave vector: $\vec{q} = 2\vec{k}$ [67]. Therefore, if the laser energy (wave length) is changed, the condition for double resonance is met at an other $\vec{k}$, shifting the peak in the Raman spectra. The height of the peaks do depend on the laser power used to acquire the traces. To allow a comparison between the traces, the back ground of each trace was subtracted and the traces were divided by the height of the G peak.

In panel A, a Raman trace of a SL graphene flake acquired in the bulk of the sample, is shown. The intensity ratio I(2D):I(G) between the $2D$ and the G peak is altering with the doping of the flake and has been found to vary between 8.7 (suspended) and 3.9 (on substrate) [72]. The two satellite

peaks to the left and right of the $2D$ peak, are the $D+D''$ peak at $2450\,\mathrm{cm}^{-1}$ and the second order $2D'$ peak at $3250\,\mathrm{cm}^{-1}$ [67, 68]. Their properties will not further be addressed here, as both peaks are also seen in defect free graphene and graphite samples. In panel B, a trace taken in the bulk of a BL flake is shown and the Lorentz fits to the $2D$ peak are shown in the inset, indicating the BL nature of the flake.

Next to the distinction between a SL and a BL flake, the defect density can be identified, as shown in panels C and D of Fig. 2.14. The presence of the D peak points to a small defect density in the sample or a close-by disordered or armchair edge. A small shoulder is observed at the right flank of the G peak, pointing towards disorder in the graphene flake. This signature is attributed to the D' peak, also visible in the presence of sp^3 hybridized carbon atoms [28]. As the trace shown in panel C of Fig. 2.14 stems from a SL flake exposed to an H plasma ($p = 0.03\,\mathrm{mbar}$), the D' peak possibly arose due to hydrogenation of the flake. In panel D, the Raman trace at an edge of a SL sample on a hexagonal boron nitride (hBN) flake is shown. Here, a red laser with a wave length of 633 nm was used to acquire the traces, leading to the above mentioned shift of the D and $2D$ peaks in the Raman trace.

Investigation of small ribbons with widths in the range or below the spot size of the laser ($\approx 300\,\mathrm{nm}$) might be difficult to investigate, as not only the bulk of the ribbons is probed, but also both edges simultaneously. Raman measurements without any D peak signature would only be expected for crystallographic ZZ edged graphene nanoribbons without bulk defects. At pristine AC edges, the Raman signature of the D peak is expected to vanish for light polarized perpendicular to the edges. The bulk and edge disorder give an angle independent, non vanishing contribution to the D peak.

As shown in the last paragraph and in Fig. 2.14, investigating graphene samples using Raman measurements allows one to quickly get an overview of the quality and the number of layers of the flake of interest. The quality of the flakes can be determined by looking at the defect peaks, including the D and D' peaks, whereas the number of layers is amounted by the $2D$ Raman peak shape. Also, the percentage of AC and ZZ type of edges can be determined by evaluating the angle dependence of the D peak.

2.2 Surface Wave Plasmas

In semiconductor fabrication, plasmas are mostly used to dry etch surfaces of wafers or sputter material onto samples. In those systems the plasma is mostly localized to a well defined area, either due to finite sized capacitor plates, used to ignite the plasma, or by magnetic fields. Such systems are difficult to build as the capacitor plates need to be inside the plasma chamber. Surface wave plasmas on the other hand, are easily implemented e.g using an RF generator and a match box, a quartz tube and a metal ring surrounding the tube. The metal ring couples the RF signal to the gas in the quartz tube and leads to the ionization of the gas. Due to the formation of a surface wave, the plasma extends away from the launcher (copper plate) and can be used over long distances, in contrast to other capacitively coupled plasmas [73].

In the next sections the fabrication and characterization of a capacitively coupled plasmas using a surfatron [73–76], interacting with the gas via a surface wave, as used in this work is elucidated. The interaction of H radicals with graphitic material is discussed, explaining the reaction mechanisms possibly found in the measurements performed in chapters 4 and 6.

2.2.1 Surfatrons

As mentioned above, a surfatron is a device used to generate long plasma columns at various plasma conditions. Such surface wave generated plasmas are different than other capacitively coupled plasmas: Instead of coupling the electric field of the RF generator perpendicularly to the gas in the quartz tube, the electric field interacts with the gas parallel to the plates. The interaction of the electric field with the gas leads first to an ionization and further, to the propagation of the electric field along the quartz tube, generating a surface wave. Hence, long plasma columns can be generated without the use of magnetic fields or extended structures surrounding the outside of the discharge vessel as the power needed to ionize the gas is transported by the surface wave along the quartz tube. The launcher can be small compared to the discharge container, as the surface wave and the ionized gas interact with each other, mutually sustaining one another. It is a very flexible device in terms of dimensions, as the ignition condition for the plasma is independent of the frequency of the applied RF signal and only depends on the RF power (see below) [73–75]. The length of the plasma can be changed by

tuning the gas pressure, the RF power or frequency, producing columns of various lengths [73, 74].

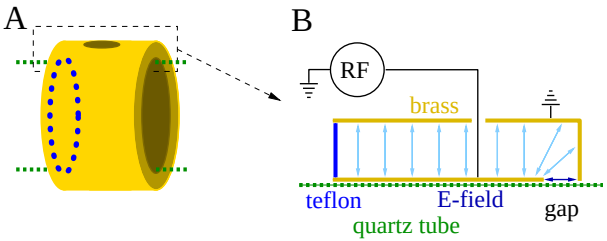

Figure 2.15: Surfatron and setup of the system used for the experiments described in chapters 4 5. Panel A: Sketch of the coupling structure. Panel B: Cross section of the coupling structure shown in panel A.

One way to fabricated a surfatron, is to arrange two metal rings coaxially to each other as shown in Fig. 2.15A, isolating them using a insulating material such as teflon (blue in Fig. 2.15) at one edge and leaving a gap between the inner and outer capacitor plate at the other edge. The surfatron is placed around the quartz tube (green in Fig. 2.15) in which the plasma will be generated. In Fig. 2.15B a cross section of the surfatron in Fig. 2.15A (black dashed lines) is shown, together with the RF connector, applying the RF signal to the inner surfatron ring, with the outer ring being on ground. The applied RF signal generates an AC electric field perpendicular to the surface of the surfatron (light blue arrows inside

surfatron). The RF signal is coupled to the gas in the quartz tube at both ends of the surfatron shown in Fig. 2.15B, however, more efficiently on the gapped side as the electric field is parallel to the quartz [76]. On the other side of the surfatron, however, the coupling is less effective, as only the parallel parts of the stray field to the quartz tube transfer the RF power into the hydrogen gas. In our setup, the surfatron has no gap region on either side of the metal rings, as the inner and outer ring have the same length. Therefore, the electric field is perpendicular to the quartz tube at both ends of the surfatron (see Fig. 2.15A). Hence, only the parallel parts of the stray fields of the applied RF signal couple at both sides to the gas in the quartz tube.

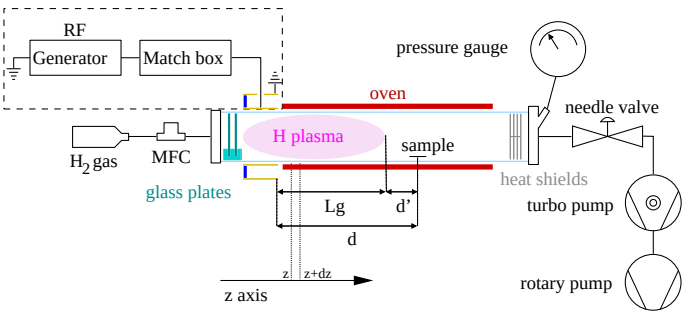

Figure 2.16: Setup of the system used for the experiments described in chapter 45. The tube has a length of 1 m and a diameter of 8 cm.

In Fig. 2.16 the setup used for the experiments explained in chapter 4 is shown. A hydrogen gas bottle supplies the gas for the process and with a mass flow controller, the gas flow through the system can be adjusted between $0-20$ standard cubic centimeters per minute (sccm). At the inlet side of the quartz tube, two glass plates (turquoise) hinder the plasma (purple) to interact with the metallic closure of the tube, reducing the loss of H atoms at the plasma end [77]. The plasma is generated with an 13.56 MHz RF signal applied to the surfatron (yellow), located outside of the quartz tube just in front of the furnace (red), with operating temperatures in the range of $50-1200^{\circ}C$. The sample is placed inside the tube at adjustable distances, as explained in chapter 4 and indicated by d in Fig. 2.16. L_g indicates the length of the glowing plasma and $d' = d - L_g$ denotes the distance between the end of the discharge region and the sample. Downstream of the tube, a pressure gauge and a needle valve are mounted to adjust the pressure inside the tube. A turbo pump and a rotary pump follow, used to pump the system down to a base pressure of $2 \cdot 10^{-3}$ mbar before adjusting the processing pressure using the needle valve.

Even if the generation of a hydrogen plasma is implemented relatively easily, its properties and the interactions taking place in the plasma, are highly non trivial. Therefore, a few important properties of surface wave plasmas are introduced in the next section.

2.2.2 Plasma Generation Using a Surface Wave

In general, a plasma can be described by a quasi neutral gas containing electrons and ions, interacting via scattering processes and behaving as a collective [78]. The energy needed to ionize the gas can be taken from an RF electric field, which can be described by $E_{RF} = E_0 e^{i\omega_{RF}t}$ where E_0 is the amplitude of the electric field and ω_{RF} is the frequency of the applied RF signal. Via a coupling device (here we used a surfatron, see subsection 2.2.1), the electric field is coupled to the hydrogen gas in the quartz tube and interacts with the gas particles. This interaction takes place via the valence electrons (e^-) and the positively charged molecular cores (H_2^+). The electrons follow the oscillations of the RF signal with a frequency $\omega_{pe} = \sqrt{\frac{n_e e^2}{m_e \epsilon_0}}$, the ions with the frequency

$\omega_{pi} = \sqrt{\frac{n_i e^2}{m_i \epsilon_0}}$, where m_e and m_i are the respective electron and ion masses [78]. The density of electrons (n_e) and ions (n_i) in the plasma are equal and the plasma is said to be in a quasi neutral state: locally, charge imbalances can occur but the total charge state of the plasma is zero. As the frequency of the RF signal is larger than ω_{pi} but smaller than the electron frequency ($\omega_{pi} < \omega_{RF} < \omega_{pe}$) at a constant charge density n, only the electrons interact with the RF signal [79]. The energy the electrons gain by interacting with the electric field does not suffice to ionise the gas [79]. Due to scattering events of electrons with neutral particles, the electrons get out of phase with the applied field and additionally gain or lose energy. Ultimately, the energy transfer from the electron to the ions during scattering events leads to the ignition of the plasma. The electron density in the plasma n_e is linearly dependent on the RF power coupled into the gas (P_{eff}):

$$P_{eff} = \frac{n_e e^2 E_0^2}{2m_e(\omega_{RF}^2 + \nu^2)} \tag{2.19}$$

with ν the electron neutral collision frequency in the plasma. If the electrons reach the ionization energy of 13.5 eV, n_e raises since further electrons are generated via electron-

neutral scattering processes (see below). However, to ignite a plasma, the cut-off condition has to be overcome [80]:

$$\omega_{pe} = \sqrt{\frac{n_{e,min}e^2}{m_e\epsilon_0}} = \omega_{RF}\sqrt{(1+\epsilon_d)} \tag{2.20}$$

where ϵ_0 and ϵ_d are the permittivity of free space and of the quartz tube respectively. The only variable in Eq. 2.20 is the electron density, which is directly related to the power of the RF signal applied to the surfatron at a frequency ω_{RF} as seen in Eq. (2.19b) [75, 79, 80]. Therefore, the cut-off condition can also be formulated by saying that a minimum P_{eff} is needed to ignite a plasma with an RF signal of frequency ω_{RF}.

Plasmas generated via a surfatron, have the useful ability to expand in the quartz tube they were ignited in. By the evolution of a surface wave, moving along the quartz tube, the energy for the ionization of the gas is distributed. In the next section, this phenomena is explained in more detail.

2.2.3 Propagation of the Surface Wave

After the ignition of the plasma ($n_e \geq n_{e,min}$), the electric field of the RF signal and the plasma electrons interact and

form a propagating surface wave at the quartz tube - plasma interface. This surface wave propagates along the interface due to the presence of ionizable particles. During propagation, the surface wave ionizes the gas particles, leading to the extension of the plasma away from the coupler device [81]. If the total power of the RF wave is coupled into the gas ($P_{appl} = P_{eff}$), the surface wave can be described by [82]

$$E_{SW} = E_0 e^{i(\omega_{RF} t + m\phi - \beta z)} \tag{2.21}$$

where m is the azimuthal mode of the electric field in the plasma, β is the wave number ($\frac{2\pi}{\lambda}$) and z is the position in axial direction. The waves considered here, are in the azimuthally symmetric mode ($m = 0$), such that the second term in the exponent of Eq. 2.21 vanishes [83].

During its propagation along the quartz tube, the surface wave transfers its RF power into the gas, ionizing it and allowing itself to propagate further [81]. To sustain the plasma, the power absorbed by the electrons in the cross section (z, z+dz) must equal the energy loss of the electrons due to radiation or scattering with heavy particles (ions or neutrals) in the plasma or at the walls. The local power transfer from

the surface wave to the electrons can be calculated using the following formula:

$$\frac{dP_{eff}}{dz} = -2\alpha(z)P_{eff}(z) \tag{2.22}$$

where $\frac{dP_{eff}}{dz}$ denotes the decrease of the power of the surface wave along the axial length of the tube and $\alpha(z)$ is the attenuation factor, effectively dependent on the electron density n_e and the electron-neutral collision frequency ν [81, 82, 84]. The average power transferred from the surface wave into the plasma per electron, θ_a, and the average power loss per electron to the plasma, θ_L, at some axial position z, must be equal to sustain the plasma (see Eq. 2.22). Therefore, Eq. 2.22 can also be formulated in terms of

$$\frac{dP_{eff}}{dz} = \theta_a(z)n_e(z)S = \theta_L(z)n_e(z)S \tag{2.23}$$

Looking at a specific position along the tube axis, one can see that n_e depends linearly on the applied power (see Eq. (2.19)). Further, as the surface wave propagates, less power is available for the compensation of n_e lost during scattering process, leading to an overall decreasing of the electron density. As soon as the power of the surface wave is too low to sustain

the minimum electron density $n_{e,min}$ (cut-off condition), the plasma column breaks down [80]. Hence, the electron and ion concentration at the end of a plasma column is not changed by varying the applied power [81]. However, the column length is altered: as more power is available to compensate for energy losses due to collisions, the surface wave can generate $n_{e,min}$ at larger distances from the plasma source [81].

Not only the applied power but also the pressure inside the tube changes the length of the column and the density of the electrons in the plasma at a fixed position. The density of the hydrogen molecules in the quartz tube increases linearly with the applied pressure, as described by the ideal gas law $n_{H_2} = \frac{p_{H_2}}{k_B T}$, with the pressure p_{H_2}, the temperature T of the gas and the Boltzmann factor k_B. A pressure raise increases the scattering frequency in the plasma and lowers the mean free path $\lambda_{mfp} = (\sigma n_{H_2})^{-1}$ of the particles in the gas. The $H - H_2$ scattering cross section is given by $\sigma = \pi(r_H + r_{H_2})^2 = 2.64 \times 10^{-15}\,\mathrm{cm}^2$, assuming that the hydrogen atoms and molecules are hard spheres [77]. Due to the increasing number of collisions, the surface wave transfers more power to the electrons in the gas, leading to shorter plasma columns.

The type of collisions occurring in a plasma strongly depend on the parameters of the plasma: especially the energy of the plasma particles define the probability of a certain collision to occur. A characterization of the particles and their energy is therefore crucial.

2.3 Plasma Characterization

Depending on the parameters used to generate a plasma, the properties of the ionized gas can vary strongly. The electron and ion temperatures can reach similar values in a high pressure plasma, whereas in a low p plasma, also called cold plasma, the ions are significantly colder than the electrons. The ion thermalization occurs by energy transfer during scattering processes with electrons. For plasmas at pressures around $1\,bar$, the amount of scattering events is large enough to allow thermalization of the ions whereas for the pressure range used here ($0.03 - 1.7\,\mathrm{mbar}$), the ions have comparable temperatures as their surrounding, hence $750\,\mathrm{K}$ in chapter 4. Depending on the energies of the various particle species in the plasma, a range of reactions can occur. It is crucial to know the energy distribution of the ions and electrons in the

plasma, to fully understand the interaction of the plasma with the surface of a sample in the vicinity or even in the discharge region. In this section, first a method for the determination of the energies of the particles in the plasma is discussed, before the most probable particle species created and their reactions are listed and clarified.

2.3.1 Langmuir probe investigations

One possibility to characterize a plasma is to investigate the electron and ion density in the system by performing Langmuir probe measurements, enabling one to calculate the energy and temperature of the particles and estimate the percentage of neutrals in the ionized gas [85, 86]. The Langmuir probe is in principle a simple wire, inserted into the glowing region of a plasma, to which a variable voltage is applied. The resulting current, flowing from the plasma through the probe, is then measured and analyzed as explained below.

When inserting an object into a plasma, the object gets negatively or positively charged by the electrons or ions, depending on the potential difference between the object and the plasma [85, 86]. If the object itself is not biased, elec-

trons will accumulate on its surface, due to their considerably higher kinetic energy, compared to the ions (see above and 2.2.2). Therefore, an electric field between the plasma and the inserted object is generated, repelling further electrons and attracting ionic species. Thus the plasma screens inserted objects and minimizes its interaction with it to ensure quasi neutrality inside the bulk of the plasma [86]. Between the accumulated positive and negative charges, the plasma is dark due to the electrons not acquiring enough energy in the dark region for ionization processes. This "non-glowing" region is called a sheat and can also be observed at the interface between the plasma and the container walls or any object (sample) inserted into the plasma [86]. The extent of the sheat is defined by the electron Debye length which is given by $\lambda_{De} = \sqrt{\frac{\epsilon_0 T_e}{q^2 n_e}} \approx 7.43 \times 10^3 \sqrt{\frac{T_e}{n_e}}$, where T_e and n_e is the electron temperature and density. (For a positively biased object, the size of the sheat would be given by the ion Debye length, respectively.) Therefore, the screening length is shorter for larger densities and smaller temperature [78, 86].

The current measured at the Langmuir probe shows a characteristic dependence on the applied voltage (see Figs. 2.17). For negative applied voltages, $V_B < 0$, the probe attracts

ions and an ion current I_i is measured. I_i saturates for ideal probes at large negative applied voltages, giving the ion saturation current I_{is}. For real measurements, I_{is} decreases with increasing negative voltage (panel (c) in Fig. 2.17), due to the expansion of the sheat with decreasing V_B [85].

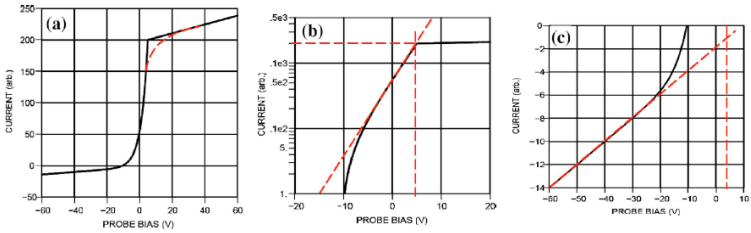

Figure 2.17: Model Langmuir probe traces adapted from [85]. When plotting the I-V characteristics obtained from Langmuir probe scans, the ion current I_i (I_e) is defined to be negative (positive). Panel (a): Ideal Langmuir probe trace showing the sharp kink at the electron saturation current. The red trace indicates the softening of the kink due to the sheat expansion. Panel (b): Semi log plot of the measure current in the transition region at the positive voltage region. The coordinates at the crossing point of the horizontal and vertical fits indicate the electron saturation current and the plasma potential. The electron temperature is given by the slope of the fit to the transition region. Panel(c): I/V characteristics of the Langmuir probe at negative applied voltage. The coordinates at the crossing of the fits indicates the plasma potential and the ion saturation current.

When increasing the applied voltage to more positive values, one observes a sign change of the measured current. The

floating potential V_f of the probe is directly given at $I = 0\,\mathrm{A}$. (see Fig. 2.17(a), $V_f = -10\,\mathrm{V}$). At this point V_B and the plasma potential V_p are equal, hence the recorded current is zero. For strongly positive applied voltages, electrons are attracted to the wire of the probe and an electron current I_e is measured. Again, the electron current saturates for ideal Langmuir measurements, giving the electron saturation current I_{es} (see panel (b) in Fig. 2.17). Similar as for I_{is}, for real Langmuir traces the sheat expansion softens the sharp kink in the I-V characteristics and I_{es} increases further with increasing V_B. In the transition region, the electron and ion current decay as shown in Eqs. (2.24):

$$I_e(V_B) = I_{es} exp\left[-\frac{e(V_p - V_B)}{k_B T_e}\right]$$

$$I_{es} = \frac{1}{4} q n_e v_{e,Th} A_{probe} \qquad with \quad V_B \leq V_p \tag{2.24}$$

$$I_i(V_B) = -I_{is} exp\left[\frac{e(V_p - V_B)}{k_B T_e}\right]$$

$$I_{is} = 0.6 q n_i \sqrt{\frac{k_B T_e}{m_i}} A_{probe} \qquad with \quad V_B \geq V_p \tag{2.25}$$

where T_e and T_i are the electron and ion temperatures, $v_{e,Th}(T_e)$ is the thermal velocity of the electrons, A_{probe} is the surface area of the Langmuir probe and k_B is the Boltzmann constant. For thermalized plasmas, I_{is} depends on n_i and $v_{i,Th}(T_i)$, comparable to I_{es}, as shown in Eq. 2.24a. However, in low pressure plasmas, as used in this work, the ions usually are cold, having a similar temperature as their surrounding [85, 86]. The ion current measured with the Langmuir probe depends on the strength of the electric field in the sheat region, as this field accelerates the ions towards the probe [85]. As mentioned above, the extent of the sheat (Debye length) depends on the electron temperature, therefore the ion current in cold plasmas is directly influenced by T_e, replacing $v_{i,Th}$ by $\sqrt{k_b T_e/m_i}$ in Eq. 2.24.

To evaluate V_p and I_{es}, the measured current is plotted on a semi log scale against the applied voltage, changing Eq. 2.24a to $\ln(I_e) = \ln(I_{es})\frac{-e(V_p-V_B)}{k_B T_e}$. To evaluate I_{es} and V_p exponential fits are performed in the electron saturation region of the I-V curve and in the transition region (between $-5\,\mathrm{V}$ and $5\,\mathrm{V}$ in Fig. 2.17b). The crossing point of the fits indicate the value of I_{es} and V_p. Further, the electron temperature

is given by the slope of the exponential fit in the transition region. Knowing V_p the ion saturation current I_{is} can be found. A linear fit is performed to the ion saturation current region in Fig. 2.17a. The value of the linear fit to I_{is} at the plasma potential is an approximated value for the ion saturation current (see Fig. 2.17c).

From the difference of V_p and V_f, the acceleration energy of the ions in the sheat region is calculated. This value is important for the interaction of the ions with the graphitic surface inside the plasma. For potential differences reaching 38 eV, the ions have enough energy to physically sputter the graphitic surface. In the plasma used in chapter 6, the potential difference amounts to $V_p - V_F \approx 12.6\,\mathrm{V}$, forbidding the physical etching of graphitic surfaces in the discharge and hence also in the downstream plasma region.

Another value used to characterise a plasma is the degree of ionization of the plasma, n_i/n_n, where n_n is the density of neutrals and n_i the density of ionized particles in the plasma. The density of neutral atoms can be approximated by the ideal gas law: $n_n = \frac{p_{H_2}}{k_B T}$, where p is the pressure in the system and T is the surrounding temperature. From Eq. 2.24b n_i can be evaluated and the degree of ionization can be found. The

degree of ionization of the plasma used in chapter 6 amounted to $n_i/n_n < 1\%$.

Further, the energy distribution of the particles in the system is described by a Maxwellian distribution with which the percentage of radicals in the system can be estimated [86]:

$$f(E) = \left(\frac{m_e}{2\pi T_e}\right)^{3/2} exp\left(\frac{-E}{T_e}\right) exp\left(\frac{-q(V_p - V_B)}{T_e}\right) \quad (2.26)$$

where E is the energy of the electrons. To generate a radical, an electron-molecule scattering process in the plasma needs at least an energy transfer of 4.52 eV being the dissociation energy for a H_2 molecule. Evaluating the amount of electrons having this energy from the energy distribution, the percentage of radicals can be calculated.

Using the Langmuir probe, several important parameters of a plasma can be evaluated: the plasma potential, the floating potential, the electron energy, the ion density, as well as the ionization degree of the gas. However, better results are obtained in plasmas with a high density of ionized particles. If the degree of ionization is too low, the Langmuir probe is not sensitive enough to measure I_e and I_i which are the basic values needed for the evaluation of the plasma parameters

listed above. Hence, the number of ionised species interacting with the Langmuir probe must be high enough to obtain reasonable results.

Comparing the electron and neutral energies from the Langmuir probe measurement results, to the energies required for the divers scattering processes, one can evaluate the most probable events occurring in the respective system. Further, outside of the plasma, the particles also interact with surfaces, e.g. the walls of the discharge container and the sample surface. In the next section, a list of possible interactions inside and outside the discharge region is listed.

2.3.2 Gas Phase and Surface Interaction of Plasma Particles

When generating a plasma inside a discharge vessel, two main regions can be distinguished: the glowing and the non-glowing, also called downstream plasma region. In the glowing part of the plasma the electrons have enough energy to create reactive particles by scattering events with H atoms or H_2 molecules (see below). As the distance to the surfatron increases, the density of newly generated reactive particles in

the plasma decrease linearly, since less power is available for the particle generation (see subsection 2.2.2) [81]. Outside of the glowing plasma region, however, an exponential reduction of the density of ions and neutrals is observed, as no new ionized particles are generated [77, 87, 88].

Knowing the energy distribution of the particles, possible interactions of the gas particles with the discharge container walls or a sample inside the tube can be estimated. As mentioned above, the power of the surface wave decreases with increasing distance to the launcher and the total number of available electrons diminishes linearly. Therefore, the amount of reactions taking place in the plasma also drops and, farther away from the surfatron, less reactions are possible. Outside of the plasma region, the energy of the particles is reduced exponentially (see below) and no new particles can be generated. However, the density of a species present at a specific point in the discharge tube can be altered by tuning parameters such as the gas pressure, the gas flow, the temperature or the power of the RF electric field. In the next few paragraphs, interactions between the particles inside the glow discharge are enumerated as well as the chemical reactions occurring at graphitic surfaces within and in the vicinity of the plasma.

Scattering Processes in the Glowing Plasma

The particles in the plasma interact via scattering events, leading to energy exchanges and ionization of H atoms and molecules. Thereby, various plasma constituents are generated, such as electrons, H^+, H_2^+, H_3^+ as well as H^- ions [89]. The energy transfers between the particles can lift molecules into higher vibrational states leading to dissociation events of H_2 molecules when scattering with electrons in the plasma. H_2 molecules in excited vibrational states can subsequently dissociate into H atoms. Next to collisions producing neutral and charged particles also recombination events occur, reducing the number of ions and radicals. The probability to measure a specific scattering event in a plasma depends on the cross section of the respective event and on the energy of the particles involved. In most of the scattering processes, the particles only exchange energy, facilitating further generation of hydrogen atoms. Dissociation events, increasing the hydrogen atom concentration in the plasma, are also in the energy range investigated in this thesis. As the chemical etching of graphite via hydrogen atoms and low energy hydrogen ions is of interest in this work, reactions generating

H are appreciated. The degree of ionization in chapter 6 is $< 1\%$. For the plasma in chapter 4, the degree of ionization could not be measured. However, due to the higher pressures employed in chapter 4, the degree of ionization is probably lower than $< 1\%$.

Below, a list of energetically possible scattering events are shown and the reaction mechanism of the different events is explained. Additional events, requiring for particles with higher energies, are not listed. The scattering processes taking place in the hydrogen plasmas we used, can be classified into the following groups (the particle energies as well as the grouping of the scattering events were taken from [89]):

1. Energy transferring form electrons to H_2, H, H^+, H^- and H_2^+
2. Two H atom collisions

The first group of scattering events always includes an energy transfer from an electron onto a H atom or H_2 molecule.

1.a) Excitation processes:

i. $e^- + H_2 \rightarrow e^- + H_2(\nu)$

Energy transfer in a scattering event of an electron and an H_2 can excite the H_2 molecule in a higher vibrational

state. Electrons with energies around 1 eV can excite H_2 molecules into high enough vibrational states ($\nu = 10$) such that further electron scattering allows dissociation or ionisation of the H_2 molecule.

1.b) Dissociation processes:

i. $e^- + H_2(\nu) \rightarrow e^- + H_2^+ + e$ (95 %) or $\rightarrow e^- + H(n) + H(n)$ (5 %)

ii. $e^- + H_2^+ \rightarrow e^- + H^+ + H(n)$

iii. $e^- + H_2^+ \rightarrow H(n) + H(n')$

In process i. the dissociation of H_2 molecules into two H atoms is depicted, being a follow-up scattering process of 1.a)i. Both dissociation events in i. are important for the generation of H atoms in the plasma. Depending on the electron energy, the H atoms can be transferred into an electronically excited states ($n \geq 1, n' > 1$), where n, n' denote the principal quantum number. Processes ii. and iii. do generate H atoms, hence being crucial for the experiments performed in chapter 4. The energies of the electrons need to be > 0.01 eV to lead to the interactions listed above, most probably being satisfied in the plasma of chapters 4 and 6.

1.c) Ionisation processes:

i. $e^- + H(n) \rightarrow e^- + H^+ + e^-, \quad n = 1, 2, 3$

ii. $e^- + H^- \rightarrow e^- + H + e^-$

The ionization of an H atom through a scattering event needs electron energies $> 2\,\text{eV}$ (process i.). Ions increase the chemical etching of graphite in the plasma and a low density is preferable for the controlled graphite etching. Further, the density of the ions decrease strongly outside of the plasma, making this process less relevant for chemical interactions in the downstream region of the plasma. Process ii. occurs at low particle energies ($<$1eV), the density of H^- is, however, very low, as the scattering events generating H^- atoms are not efficient.

1.d) Radiative processes:

i. $e^- + H^+ \rightarrow H(n) + h\nu, \quad n = 1 - 4$

During radiative processes, the attachment of an electron to a neutral H atom or a hydrogen ion can lead to the emission of a photon. It is a recombination process, reducing the number of ions in the system, increasing the density of wanted H atoms and being therefore a relevant process for the chemical etching of graphite.

The energy of the electrons should be larger than 0.1 eV which is fulfilled in the plasmas used in this thesis.

The second group of scattering processes involves the presence of an H^+ and an H atom and leads to the excitation of the particles via energy transfer:

2.a Energy transfer process:

i. $H^+ + H(1s) \rightarrow H^+ + H(n'), \quad n' = 2, 3, 4, 5$

ii. $H^+ + H(n) \rightarrow H^+ + H(n'), \quad n = 2, 3, \quad n' = 3, 4$

The hydrogen ion energies involved here, start at 0.2 eV (process i.) and 0.1 eV (process ii.), however strongly depend on the excitation state of the H atom. In general the particles need less energy if the H atom is already in an excited state. Even if the particles only exchange energy in this process, H atoms with higher energies are generated,

The density of ionised particles is very low in the plasma used in chapters 4 and 6 and only a small percentage (<1%) of the atoms in the plasma are ionised. The H atoms and ions generated in the plasma are used for the chemical interactions with the graphitic surface. In the gas volume between the end of the plasma and the sample, however, further reactions take

place, diminishing the concentration of ions and radicals in the gas, as elucidated next.

H Recombination in the Downstream Plasma

The ion concentration is reduced in the gas phase via recombination processes as mentioned above. The hydrogen atom concentration, on the other hand, is reduced less fast, as the H atoms are either lost by scattering in the gas phase, involving three particles, or at the surface of the quartz tube [77]. As the cross section for a three particle scattering is very low, the recombination process at surfaces is the dominant mechanism [79, 89].

The decrease of the H atom concentration in the downstream region of a plasma, with the gas particles subjected to flowing conditions, can be described by [77]:

$$[H] = [H]_0 exp(-\beta\gamma^{1/2}\eta d') \tag{2.27}$$

where $[H]_0$ is the hydrogen concentration at the border of the plasma and $[H]$ at a distance d' downstream of this point, see also Fig. 2.16. γ is the material dependent H atom recombination coefficient and $\beta = \frac{v_{Th}}{RD}$ is a geometrical factor,

depending on the thermal velocity v_{Th} and the diffusion coefficient D of the H radicals, as well as on the radius of the tube R [77]. The ratio $\eta = \frac{F}{F+v_f}$ accounts for the diffusion (F) and the flow (v_f) velocity of the plasma particles.

The parameters in the exponent of Eq. 2.27 depend on the pressure and flow rate of the gas. Table 2.1 lists the parameters influencing the exponent and their values for the pressures used in the experiments performed in chapter 4.

The diffusion velocity describes the nondirectional motion of the gas particles, whereas the flow velocity is an oriented motion, directing the gas particles along a main flow direction. Therefore, a high flow rate is favorable over a high drift velocity, such that the particles are directed along the tube, increasing their probability to hit the sample surface before interacting with the quartz tube walls. A higher density of reactive particles will also augment the chemical reaction rate at the sample surface. Increasing the flow rate might have a strong influence on the graphitic etch rate [27]. In the next section, the interaction of the hydrogen atoms reaching the surface of the graphite is explained in more detail.

Pressure p (mbar)	Flow velocity $v_f = \frac{p_1 V_1 T}{T_1 p \cdot A \cdot 60\,\mathrm{s}}$ (cm/s)	Diffusion constant $D = \frac{D'}{p}$ (cm^2/s)	Diffusion time $t = \frac{(d')^2}{D}$ (s)	Diffusion velocity $F = \sqrt{\frac{D}{2t}}$ (cm/s)	MFP $\lambda = \frac{V_1}{\sigma n_{part.}}$ (mm)
0.4	44	22750	$3 \cdot 10^{-4}$	6500	0.5
0.7	25	13000	$8 \cdot 10^{-3}$	930	0.3
1	18	9100	$2 \cdot 10^{-2}$	480	0.2
1.4	13	6500	$4 \cdot 10^{-2}$	283	0.1
1.7	10	5353	$6 \cdot 10^{-2}$	206	0.1

Table 2.1: Pressure dependent parameters and calculated values for the pressures used in the experiments of chapter 4. p denotes the pressures investigated. The flow velocity (here 20 sccm) of the gas in the system can be adjusted with a mass flow controller. Using the ideal gas law, the particle density $n_{part.}$ is calculated. $\sigma = 3.7 \cdot 10^{-15}\,\mathrm{cm}^2$ is the scattering cross section for an H atom, assuming it being a hard sphere. The flow rate is adapted for the respective pressure and temperature values: $p_1 = 1$ bar, $V_1 = 20\,\mathrm{cm}^3$, $T_1 = 273.15\,\mathrm{K}$, $T = 723.15\,\mathrm{K}$. $A = 50.27\,\mathrm{cm}^2$ is the area of the tube. The pressure independent diffusion coefficient at $T = 700\,\mathrm{K}$, $D' = 9.89\,\mathrm{atm} \cdot \mathrm{cm}^2/\mathrm{s}$, was taken from [90]

2.4 Chemical Reactions

The interaction of e.g. H atoms (H radicals) with a graphitic surface (including SL and BL graphene, as well as bulk graphite surface) can lead to a chemical modification or even to its erosion. Chemical etching of graphite surfaces can occur via different mechanisms, including only hydrogen atoms or mixed interactions of radicals with ions, depending on the energy of the respective species and on the surrounding temperature [91]. Subsequently, three most likely reaction mechanisms taking place in our setup are explained.

2.4.1 Temperature dependent chemical interactions

The surrounding temperature influences the chemical reactions at the surface of the graphitic material. The reaction is started if either an H atom reaching the graphitic surface binds to a dangling carbon bond on the sample surface or a low energetic H ion (4 eV) breaks a C-C double bond (position 1 in Fig 2.18). Further H radicals can bind to the carbon atoms until a CH_3 molecule and a neighboring sp^2 carbon

radical are formed (see Fig. 2.18, position 2A). Depending on the temperature of the system, either a H atom binds to the dangling bond of the C atom ($< 400\,\mathrm{K}$) or, at $T > 400\,\mathrm{K}$, the $\cdot CH_3$ radical leaves the surface and the carbon π network is closed again (see Fig. 2.18, position 2B and 3). The process involving the dissociation of the $\cdot CH_3$ molecule from the graphitic surface is known as the chemical erosion [91–93].

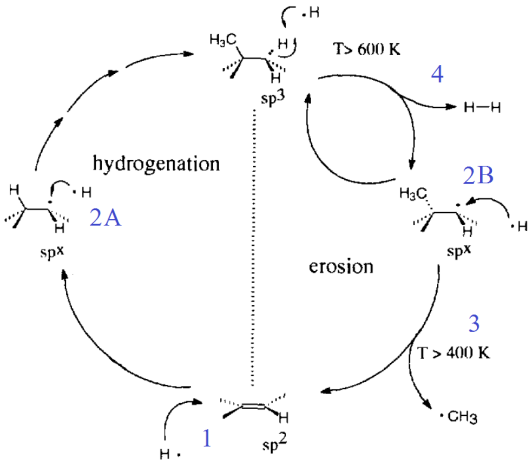

Figure 2.18: Possible carbon hydrogen interaction occurring on the surface of the graphite substrate. The interactions are temperature dependent as indicated in the figure. Adapted from [92].

For temperatures above 600 K, the etch rate diminishes again, as H atoms in the gas phase interact with H atoms bound

to the graphitic surface, forming H_2 molecules (Eley-Rideal process, Fig. 2.18, position 4) [94]. The thermal H atom split-off from the graphitic surface is a rapid process, lowering the percentage of possible $\cdot CH_3$ release [92, 93]. This temperature dependent erosion has been found to vary with the H flow in the system. For higher flow rates, the temperature at which maximal graphite etching was observed, also increased [93].

2.4.2 Interactions with Low Energetic Hydrogen Ions

The interaction of low energetic H ions with the graphitic surface is discussed in this section, before the interaction of H atoms with the graphitic edges is explained below. Inside the discharge of the plasma, not only H radicals are produced, but also ions, interacting as well with the graphitic surface. The ions in our setup have not enough energy to physically sputter the carbon network, for which about 36 eV would be needed [91, 95]. In the glowing region of the plasma, the maximum ion energy is around 12.6 eV in chapter 6 and most probably lower in chapter 4, whereas outside of the plasma the ions have even lower energies and recombine quickly to a neutral

gas. However, chemical sputtering also induces defects into the carbon network, allowing for the erosion of the graphite surface. The process of chemical sputtering takes place as follows: A low energy ion ($3 - 10\,\mathrm{eV}$) hits the graphitic surface, breaking C-C bonds [91, 93, 96]. In the presence of a large hydrogen atom concentration, the probability of hydrogen bonding to the freshly broken C-C network is enhanced and leads to the formation of stable C-H bonds. Now, additional H atoms can adsorb onto the CH molecules forming methyl (CH_3) groups. However, if the H atom concentration is low, the freshly broken C-C bonds recombine and the sp^2 network is closed [93].

Next to the chemical erosion ($E_{ion} > 3\,\mathrm{eV}$), also ion assisted chemical sputtering can occur at low ion energies [91]. Even if the ions have not enough energy to break carbon bonds ($E_{ion} < 3\,\mathrm{eV}$), positioning themselves in between two neighboring carbon atoms, weakens one of the C-C double bonds and forms a new CH link. The other carbon atom is left behind as a radical, which subsequently can interact with another hydrogen ion or atom [91]. Both reaction mechanisms explain the enhanced graphite etching when placing the samples inside the glowing region of the plasma used in chapter 4.

Depending on the systems temperature, the CH_3 bonds get thermally desorbed from the surface (see above) or another low energetic ion helps completing the erosion step. In the latter case, the ions transfer their kinetic energy onto the methyl groups on the sample surface, allowing the breaking of the methyl carbon bond. To release a methyl group (break a C-C σ bond), approximately 4 eV is required [92, 96]. However, even if the systems cannot supply the total energy the reaction can still take place: due to the release of the methyl group, a C-C π bond can be formed, lowering the energy of the system by 2 eV. Hence, the effective energy needed to release the methyl radical accounts only to 2 eV [92, 96].

2.4.3 Interaction at Graphitic Edges

Hydrogenation of the carbon atoms on the graphitic surface changes the effective bond lengths and strengths of neighboring carbon atoms [97]. Less energy is necessary for a single hydrogen to bind to a carbon atom on a ZZ edge than on a AC site. Also for a second H atom, the binding is more favorable on a ZZ than on a AC site as calculated by [97]. Looking at the type of bonding at the ZZ and AC edge, one

observes that the carbon at the ZZ edge, saturated with two hydrogen atoms, form sp^3-sp^2 bonds whereas the AC carbon atoms form weaker sp^3-sp^3 bonds. Therefore, the saturated carbon atoms at a AC edge are broken with more ease than the ones at the ZZ edge sites.

In summary, atomic hydrogen interacts strongly with the graphitic surface either by directly binding to available dangling bonds at defects in the graphitic surface or, in combination with hydrogen ions, by breaking the sp^2 carbon network anywhere on the surface. As the second process involves low energy ions, this reaction takes place in the discharge region of the plasma or in the vicinity of the plasma border. Farther downstream of the plasma, this type of reaction is negligible as the ion density decays exponentially outside of the plasma region. The first interaction process, however, not only depends on the distance to the end of the plasma, but also on the flow rate, as the recombination of the hydrogen atoms takes place mainly at the quartz tube walls. In chapter 4 the distance dependence of the graphite etching by hydrogen radicals and ions is examined.

Chapter 3

Magnetotransport in Graphene Hall Bars

The width dependence of the quantum Hall effect in graphene nanoribbons is experimentally investigated by magneto transport measurements in graphene Hall bars of various widths. Using standard reactive ion etching and electron beam lithography techniques, graphene Hall bars $550\,nm$ *in width are fabricated and magnetotransport measurements are performed in a dipstick at* $T = 4.2\,K$ *using a* $14\,T$ *magnet. The Landau fans depict the expected quantum Hall signature for single layer graphene flakes. The voltage probes of the Hall bars mostly were insulating, indicating localized electrons at constrictions in the graphene sample.*

3.1 Introduction

After the first isolation of graphene by André Geim and coworkers [3, 4], a lot of effort has been put into the formation of a band gap in graphene to make it available as a truly 2D material in electronic industry. Various theoretical calculations expected the opening of a band gap in crystallographically edged graphene ribbons of a few nanometers in width [6, 7, 9]. Several research groups [11–13] started investigating the electrical transport properties of such structures, immediately seeing the expected reduction in conductivity, as well as the inverse proportionality of the gap with the ribbon width. However, closely looking at the transport measurement reveals that, instead of solely measuring the electronic band gap of the graphene ribbons, localized charge carriers are probed additionally [98]. The energies of the measured gaps do not correspond to the theoretically expected ones. For a 5 nm wide armchair ribbon, the energy gap is expected theoretically between 100 meV−250 meV, whereas the experimentally probed gaps reach 400 meV already at a width of 15 nm [9, 11]. Further, zooming into the transport gap region of the conductivity traces measured in graphene nanoribbons,

reveals Coulomb diamonds, indicating the localization of the charge carriers [11, 13, 98–100].

Most of the graphene nanoribbons investigated electrically are fabricated using e-beam lithography and reactive ion etching techniques, generating ribbons with rough edges on a nanometer scale. Rough edges, together with a small energy gap, can lead to Anderson localization, trapping the charge carriers in the ribbon [101, 102]. Determining the size of the induced band gap is therefore difficult, if only electrical measurements are used, as the band and transport gap cannot be separated clearly [8, 9, 11].

Measuring the quantum Hall effect in graphene nanoribbons could elucidate whether only a transport gap or, additionally, a band gap is formed in the confined region. Transport measurements in a magnetic field allow the differentiation between the localized states and a band gap. If only localized states are present, the usual odd integer graphene Landau level sequence, together with the zeroth Landau level at the charge neutrality point is expected [39]. (Recently, this has been confirmed in suspended graphene nanoribbons [103].) The band structure changes when confining the 2D graphene flake to a narrow ribbon [8–10]: as in this situation

no states are available at the Dirac point, the zeroth Landau level should not be visible.

3.2 Hall Bar widths and Energy Gap Estimation

As we have seen in chapter 2, the band gaps of armchair ribbons depend on w^{-1}. Comparing experimental results with the theoretical values, one realizes that the measured gaps are significantly larger than expected [6, 8, 9, 11, 99]. However, the theoretical and experimental values agree, if one assumes localized states at the edges of the ribbons, thinning its geometrical width available for transport. Further, in the presence of a small energy gap, Anderson localization can trap the charge carriers in between two constrictions, leading to the formation of quantum dot like structures along the ribbon [14]. To hop from one ribbon segment to the next, the charge carriers need to overcome the energy barrier given by the transport gap which can be estimated by [14]

$$E_g \approx \frac{\hbar v_F}{w} \approx \frac{0.66eV}{w} \tag{3.1}$$

with w the ribbon width and $v_F \approx 10^6\,\mathrm{m/s}$. Next to the localisation of the charge carriers at the edges, charge inhomogeneities in the substrate also affects the transport through the samples. Long range scatterers deposited on the sample surface might also influence the low n_D regime in the sample, further localizing the charge carriers contributing to transport.

The localization of the charge carriers can be reduced by lowering the number of charged scatterers in the sample and by applying a magnetic field. Due to the Lorentz force, acting on the moving charged particles, the carriers get deflected and move along the edge of the sample performing skipping orbits [48]. However, the width of the devices must be at least twice the radius of the skipping orbit to reduce back scattering events [48]. The radius of the skipping orbit varies either with the B-field (constant n_D) or with n_D (constant B-field) (see also chapter 2.1): $r_c = \sqrt{\frac{2\hbar n}{eB}}$ with n the Landau level index. To attain the smallest possible cyclotron radius, low charge carrier densities (only lowest Landau levels occupied), and high magnetic fields are essential.

	Ribbon		Probes	
	Width w (nm)	Transport gap E_g (meV) [14]	Width w_p (nm)	Transport gap E_g (meV) [14]
1	20	33	20	33
2	75	9	60	11
3	250	3	70	9
4	550	1	180	4

Table 3.1: Hall bar and probe widths as well as the estimated transport gaps for the respective ribbons. The transport gap decreases with increasing ribbon width. Here, the width dependence is assumed to stem from trapped charges on island like structures separated by constrictions.

The magnet at the measurement setup used, reaches 14 T and the smallest ribbon for which the first Landau level is expected to still be visible at 14 T, has an estimated width of $w \approx 20\,\text{nm}$. In table 3.1 the Hall bar widths and the size of the probes are listed, together with the expected transport gaps arising for $B = 0\,\text{T}$ measurements. The samples are etched into Hall bars with six voltage probes on each side of the bar such that the contacts can be deposited away from the measurement region. Metal contacts tend to locally dope graphene and induce dopants in the contact region, which could smear the energy gap signature of interest [104, 105].

3.3 Device fabrication and measurement setup

Single layer graphene flakes are prepared via exfoliation and subsequent deposition onto a Si/SiO_2 wafer piece, as described in [3] and thoroughly in the appendix. With atomic force microscopy (AFM) measurements, the height and quality of the samples are investigated and flakes with clean surfaces are chosen for further device processing. Standard e-beam lithography and reactive ion etching processing is employed to pattern 550 nm wide Hall bars into the graphene flakes before titanium/gold contacts are deposited onto the samples (see appendix and table 3.1). The samples are bonded to a chip carrier using gold wires and subsequently mounted onto a dipstick which is then lowered into a liquid helium filled measurement dewar containing a 14 T magnet.

In Fig. 3.1, an AFM image of a 550 nm wide graphene nanoribbon with 180 nm wide probes is shown, being similar to the sample measured. The transport properties of the ribbon are measured in four probe configuration by driving a current between the yellow contacts and measuring the

longitudinal voltage V_{xx} between the green voltage probes as shown in Fig. 3.1. All the measurements shown here are

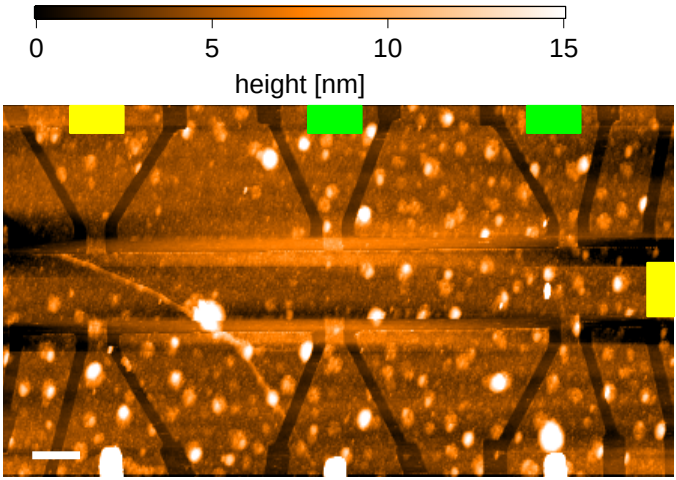

Figure 3.1: AFM image of a 550 nm wide Hall bar. At the lower side of the image, the voltage probes are visible. The white spots on the AFM image are a few tens of nanometer in height and are most probably PMMA residues form e-beam lithography patterning.

performed using standard lock-in technique, applying an AC modulation of 1 nA to the sample. The samples are first characterized at zero magnetic field before the Landau level signature of the ribbons is measured as explained below.

3.4 Transport measurements in graphene Hall bars

In Fig. 3.2 the longitudinal conductivity (blue trace) and the resistivity (red trace) plotted against the back gate voltage at $B = 0\,\mathrm{T}$ is depicted. Clearly, the Dirac point is strongly shifted from $U_{BG} = 0$, where the change of charge carriers from holes to electrons is expected for intrinsic graphene, to about $U_{BG} = 44\,\mathrm{V}$. Further, the minimum conductivity at the Dirac point has a value of approximately $9\,\mathrm{e}^2/\mathrm{h}$ as indicated by the black horizontal dashed line in Fig. 3.2. The minimum conductivity is expected to arise at a value around $4e^2/h$ for intrinsic graphene, where 4 accounts for 2 spin and 2 valley states [43].

At low charge carrier density n_D the transport properties strongly depend on long range scatterers such as Coulomb impurities, induced by the substrate or deposited molecules on the graphene substrate. Molecules deposited on the sample surface during fabrication, can dope the graphene flake and induce an overall shift of the Dirac peak to non-zero back gate voltage. As we cool our samples to 4.2 K in a dipstick,

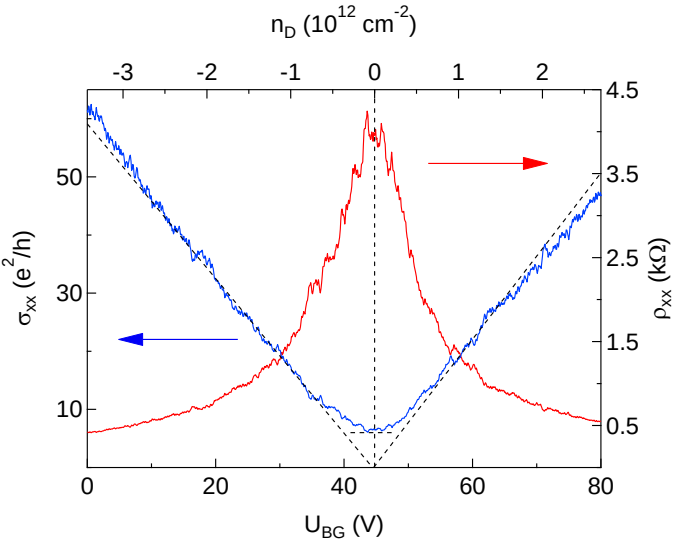

Figure 3.2: Zero magnetic field measurements of a 550 nm wide graphene Hall bar at 4.2 K. The charge carrier density is estimated assuming a parallel plate capacitor model as described in section 2.1.3.

air molecules are probably additionally deposited on the sample. During cool-down, the gas particles freeze on the sample surface and can partially be responsible for the shifts of the Dirac peak seen in Fig. 3.2. As the most abundant molecules in the air are nitrogen and oxygen, both being strongly electronegative [40], the shifts of the Dirac peak to more positive gate voltage is plausible [106, 107].

The SiO_2 substrate, on the other hand, is known to induce charge inhomogeneities in graphene and form electron and hole puddles, locally altering the density of states of the sample [15]. Hence, when probing the conductivity of the sample, the average Dirac peak position over the measured region is probed, smearing the exact position of the Dirac peak. In other words, when the back gate voltage is tuned to the Dirac peak, some regions of the flake remain doped with a small residual charge density due to the electron hole puddles. The size of the residual charge will influence the value of σ_{min} [108, 109]. Hence, the charge inhomogeneities in the SiO_2 substrate can increase the minimum conductivity at zero back gate voltage.

Not only is the Dirac peak shifted by charged impurities, such as deposited molecules, the Dirac line trace is also broadened. For samples exposed to a large density of charged impurities the Dirac peak is strongly shifted from $U_{BG} = 0$ as well as heavily broadened, as has been shown experimentally [16, 107, 109] and calculated theoretically [108, 110, 111]. Lattice defects (short range scatterers) in graphene, on the other hand, reduce the minimum conductivity below $4e^2/h$, increasing the resistivity of the samples due to the broken π network,

in contrast to Coulomb scatterers [106, 112]. As σ_{min} is larger than $4e^2/h$ in the samples measured here, Coulomb scatterers are expected to be the main reason for the shift and broadening of the Dirac peak in Fig. 3.2.

At high charge carrier density the conductivity for graphene samples with low charge impurity density deviate from the linear behavior expected ($\sigma \propto n_D$). The sublinearity of the conductivity can be explained by the stronger influence of the short range scatterers reducing the conductivity at high n_D [108, 113]. In Fig. 3.2 the sublinearity of the conductivity in the electron charge carrier regime is clearly visible, hence at large n_D, short range scatterers dominate the transport properties of the samples. The superlinear behavior of the conductivity in the hole doped regime could be explained with the distant dependent influence of the charged scatterers on the graphene transport measurement [108]. When increasing the back gate voltage to high values (positive or negative) the distance between the graphene sheet and the charged impurities alters, changing the influence of the impurities on the transport properties of the flake. When the sign of the charged particles and the back gate agree, the distance between the graphene and the Coulomb scatterers increase. The

effect of short range scatterers on the transport properties is then visible. In Fig. 3.3, the field effect mobility of the sample investigated is shown.

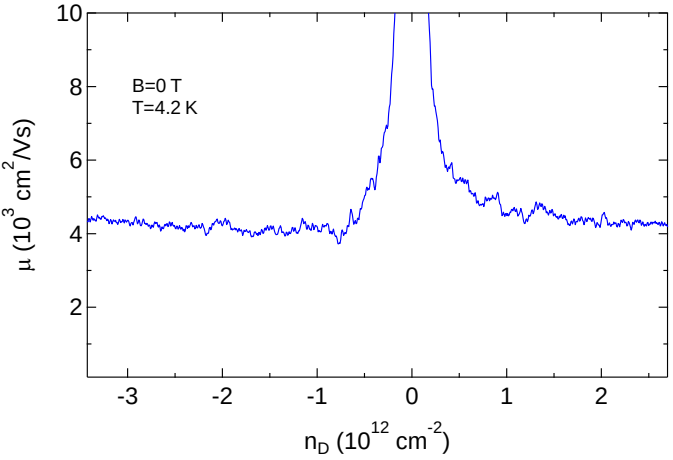

Figure 3.3: Mobility of the 550 nm sample measured in this chapter. The mobility was estimated using the field effect mobility approach mentioned in chapter 2.1.3. The mobility diverges near zero charge density and relevant mobilities are found at large n_D.

The electron and hole mobilities reach a density independent value of $\mu = 4300\,\mathrm{cm}^2/(\mathrm{Vs})$ at a charge density above $n_D = 1 \cdot 10^{12}\,\mathrm{cm}^{-2}$ ($n_D = 2 \cdot 10^{12}\,\mathrm{cm}^{-2}$) for hole (electron) charge carriers and are in the lower range compared to literature values of graphene samples on substrate [3, 107, 109]. However, mobilities of $\approx \mu = 10^5\,\mathrm{cm}^2/(\mathrm{Vs})$ have been mea-

sured in suspended samples with at charge carrier densities of $\approx 2 \cdot 10^{11}\,\mathrm{cm}^{-2}$ [16], indicating that charged impurities influences the transport properties of the system investigated here.

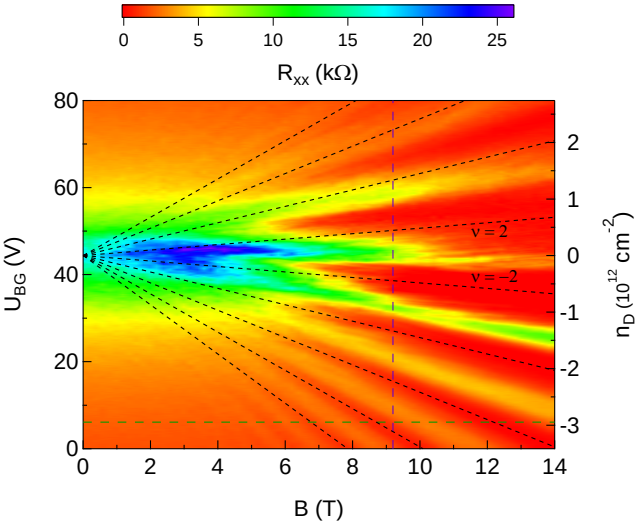

Figure 3.4: Magneto transport of the 550 nm Hall bar sample. The resistivity peaks are subjected to disorder, as seen in the zeroth LL. The black dashed lines indicate the position of the filling factors.

In a next step, magneto conductance measurements are performed, scanning the back gate voltage symmetrically around the Dirac peak and stepping the magnetic field from 0 T to 14 T. The resulting $2D$-plot of the Landau fan for positive

magnetic field is shown in Fig. 3.4. The separation of the Dirac peak into Landau levels is clearly seen for magnetic field values higher than 4 T. In the hole carrier regime ($\nu < 0$), the quantum Hall effect is more pronounced and the R_{xx} peaks are better separated than on the electron side ($\nu < 0$). The black dashed lines indicate the positions of the filling factors, $\nu = \pm 4(n + \frac{1}{2})$, n being the LL index, nicely corresponding to the resistance dips at negative ν [43]. At positive ν the resistance dips are slightly shifted to higher n_D, which could be due to the presence of hole dopants, influencing the charge density of the sample. Further, at high magnetic fields and zero charge carrier density, R_{xx} is not symmetric and larger on the hole density side. In Fig. 3.5, line cuts at a constant magnetic field of 9.2 T (panel A) and at a constant back gate voltage of 6.1 V (panel B) are depicted.

The position of the zero LL is not B field dependent, hence, the R_{xx} peak at $n_D = 0$ can be assigned to the LL$= 0$. The zero LL should not be present if an energy gap is opened in the graphene ribbon as the density of states at the Dirac point in this situation is zero. The graphene sample measured is most probably a SL graphene sample with no energy gap. In between the R_{xx} peaks depicted in Fig. 3.5A, the value of

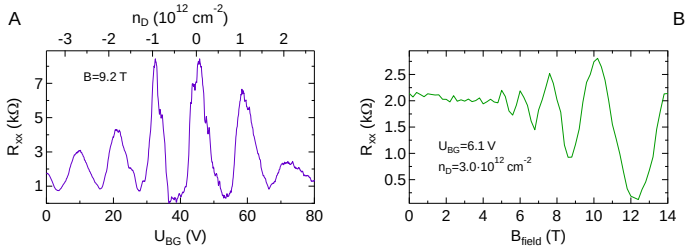

Figure 3.5: Line traces at a fixed magnetic field (9.2 T) in panel A and a fixed back gate voltage (6.1 V) in panel B, indicated in Fig. 3.4 by the green and blue dashed lines.

the longitudinal resistivity is expected to reach zero, clearly separating the LL. Only at approximately $B = 11\,\mathrm{T}$ R_{xx} reaches the base line, indicating the presence of disorder.

Magnetotransport measurements of ribbons 20 nm, 70 nm and 250 nm in width could not be investigated properly as the voltage probes (20 nm, 60 nm and 70 nm) were insulating. Hence the roughness of the edges strongly localize the charge carriers the charge carriers in the probes, indicating the importance of the edge for transport measurement in graphene ribbons.

3.5 Conclusion and outlook

Graphene Hall bars of 550 nm in width were fabricated and measured at 4.2 K and magnetic fields up to 14 T. The charge carrier mobility of the samples measured reached $\mu = 4500\,\mathrm{cm}^2/(\mathrm{Vs})$, being comparable to previously reported values for graphene samples on substrate [107, 109]. Long range scatterers probably influence the transport measurements, broadening the Dirac peak at $B0\,\mathrm{T}$ and increasing the R_{xx} minima at magnetic fields up to $B = 11\,\mathrm{T}$. Additionally, a significant amount of disorder is induced by the rough edges also leading to insulating voltage probes.

It has been shown recently that even for ribbons of a few tens of nanometer in width, the transport gap measured at $B = 0\,\mathrm{T}$ vanishes when applying a magnetic field [103]. However, the ribbons are fabricated by current annealing micrometer sized flakes, burning the samples to a few nanometers in width. Additionally to the width, the crystallographic orientation of the ribbon edge might be of importance for future electrical graphene devices.

Fabricating samples with larger probes and less charge inhomogeneity, allowing measurements at low charge carrier densities, could open the way for the investigation of the confinement gap, as well as spin alignments and Majorana fermions in graphene ribbons [9, 53]. Another fabrication method for graphene nanoribbons has been proposed using a pure hydrogen plasma [23, 25]. Exposing graphene to an H plasma leads to a chemical interaction of the graphitic surface with the H atoms. The reaction is anisotropic and intrinsic or predefined defects in the graphene flake are transformed into zigzag edged hexagonal holes [23, 25].

Chapter 4

Defining Zigzag Edges in Single Layer Graphene with a Hydrogen Plasma

D. Hug, S. Zihlmann, M. Rehmann, L. Marot, D. M. Zumbühl

4.1 Abstract

We investigate the anisotropic chemical etching of a pure hydrogen plasma on graphite samples and graphene flakes with predefined circular holes on SiO_2 substrates in dependence of the gas pressure, the sample - plasma distance and the system temperature. During the etch process, the predefined holes evolve into hexagonal pits, demonstrating the anisotropy of the etch. The pressure and distance parameters clearly influence the etching strength, indicating higher etch rates for lower pressures and smaller distances. A maximum etch rate for graphene samples is found at intermediate temperatures. The etch strength differs for single and bilayer graphene samples and the anisotropy of the etching is strongly substrate dependent for single layer graphene.

4.2 Introduction

Graphene nanoribbons (GNRs) have emerged as a promising platform for graphene nano devices, including a range of intriguing quantum phenomena beyond opening of a confinement induced band gap[6, 7, 9, 10]. In armchair GNRs, giant

Rashba spin-orbit coupling can be induced with nanomagnets, leading to helical modes and spin filtering[53]. Further, Majorana fermions localized at the ends of the ribbon were predicted in proximity of an s-wave superconductor[53]. Zigzag ribbons, on the other hand, were proposed as a promising host for spin qubits[114]. Theory showed that electronic states in zigzag ribbons are strongly confined to the edge[6, 7, 9], recently observed in experiment[115–117]. Further, edge magnetism was predicted to emerge at low temperatures[6, 7, 10, 118], with opposite GNR edges magnetized in opposite directions. High quality, crystallographic edges are very important here, since edge disorder suppresses magnetic correlations[118] and tends to cause electron localization, inhibiting transport studies. GNRs fabricated with standard electron beam lithography and Ar/O_2 etching typically exhibit **pronounced disorder** [11, 21, 60, 61, 100–102, 119], complicating transport studies.

In early fabrication techniques, GNR were produced using standard e-beam lithography and reactive ion etching, generating rough edges and inducing strongly localized states in the bulk of the samples [4, 11]. To see the predicted effects, new fabrication methods, creating ribbons with crystallographic

edges, had to be developed, such as carbon nanotube unzipping [22, 120], ultrasonication of intercalated graphite [21], chemical bottom up approaches [26, 121] or thermal etching of graphene sheets [122, 123]. Chemical bottom up approaches, however, only yield armchair GNR with lengths of a few tens of nanometer, making the production of contacts and electrical measurements of the samples difficult. Furthermore, most of these processes involve elaborate chemical steps and are laborious to implement. Anisotropic thermal [122, 123] or hydrogen plasma [23, 124, 125] etching of graphene samples is less difficult in application and allows fabrication of ribbons with crystallographic edges of adjustable dimensions. However, thermal etching requires the presence of the underlying oxide for the process to occur, blurring the influence of the edge quality on the transport properties of the ribbon. Also, reliable anisotropic hydrogen plasma etching of single layer (SL) graphene, compared to bilayer (BL) graphene, appears to be challenging [23, 27, 125]. Here, we demonstrate a method for a reproducible anisotropic etching of SL graphene on hBN flakes, opening the door to the investigation of the intrinsic graphene ribbon transport properties in dependence of the edge quality. We can control the etch rate and type

by adjusting parameters such as the gas pressure and the sample-plasma distance.

4.3 Setup and Fabrication

A pure hydrogen (H) plasma was created with an RF generator running at 13.65 MHz and 30 W coupled to a home built surfatron [74] mounted at the gas inlet side of a quartz tube of 80 mm diameter. A mass flow controller mounted upstream was used to fix the H-gas flow at 20 sccm and a pressure gauge was mounted at the downstream end of the quartz tube, closely reflecting the sample pressure. A needle valve situated downstream was used to adjust the pressure. The sample was placed a distance d from the end of the surfatron and the quartz tube was heated to the process temperature T in a three-zone furnace. In order to characterize and optimize the anisotropic etching process, we studied the influence of pressure, distance, and temperature on the etching process, generally finding good repeatability. We first investigated graphite flakes, allowing for rather simple and fast processing. The graphite specimen (NGS Naturgraphit GmbH) were cleaned by peeling with scotch tape and subsequently exposed for one hour to a pure H plasma at $T = 400\,^{\circ}\mathrm{C}$.

4.3.1 Distance dependent etching

We first present the distance dependence of the H plasma process. Figure 4.1A shows AFM topography scans for exposures of one hour at four different distances at constant pressure $p = 1\,\mathrm{mbar}$. At the larger distances, etch pits of monolayer step height are created upon plasma exposure, exhibiting a regular hexagonal shape and demonstrating a strongly anisotropic process [23, 124]. The edges of all the hexagons are in parallel alignment, pointing along the zigzag directions of the graphite basal plane, as previously established [23, 124, 125]. As the sample is brought closer to the plasma, significantly more etch pits appear, often located at the border of existing holes, sharing one common hexagon side (see Figure 4.1A, $d = 42\,\mathrm{cm}$). For the closest position $d = 37\,\mathrm{cm}$ – unlike the larger distances – the sample is located within the visible plasma glow region, resulting in a strong and several layers deep scarring of the entire surface.

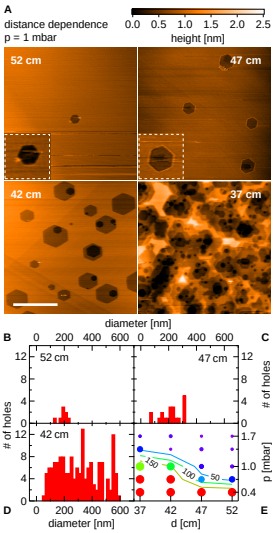

Figure 4.1: **Distance dependence of graphite plasma exposures** (A) AFM images (tapping mode) of graphite surfaces for various distances d, as labeled, all exposed for one hour at $p = 1\,\mathrm{mbar}$ and shown on the same color scale. Main panels are $3 \times 3\,\mu\mathrm{m}^2$, scale bar is $1\,\mu\mathrm{m}$, insets (dashed white boxes) are $0.25 \times 0.25\,\mu\mathrm{m}^2$. Slight hexagon distortion at 42 cm is an imaging artefact due to drift. (B-D) Histograms obtained from $10 \times 10\,\mu\mathrm{m}^2$ scans, showing the number of holes against hole diameter (bin size 20 nm) for d as labeled. (E) Summary of all exposure histograms. The size of the circles corresponds to the width of the diameter distribution. The color indicates the number of holes, with red corresponding to large number of holes. For samples located within the glowing plasma (red circles), a lower bound of 300 holes and a minimum width of distribution of diameter of 600 nm is shown.

To quantitatively study the distance dependence, we evaluated larger images to gather better statistics and plot histograms showing the number of holes as a function of diameter, see Figure 4.1B-D. The overall number of holes ob-

viously increases strongly with decreasing sample-surfatron distance d. For small distances, a wide distribution of diameters is seen, ranging from several 100 nm down to nearly vanishing hexagon size, suggesting that new defects serving as etch seeds are created throughout the exposure time. For larger d, on the other hand, the few holes seen have comparable diameters, consistent with etching proceeding predominantly from preexisting graphite defects, without adding new defects. As previously shown [23, 124, 125], exposure to ions creates defects, while exposure to hydrogen radicals results in anisotropic etching and growth of hexagons centered around preexisting defects and borders.

4.3.2 Pressure dependent etching

Next, we turn to the pressure dependence. In Figure 4.2A, AFM topography images are shown at four different pressures p at constant distance. The number of holes increases with decreasing pressure, similar to decreasing distance, giving rise to etch pits of monolayer step height at intermediate pressures. At the highest pressures, however, no etch pits where observed, in strong contrast to the lowest pressure,

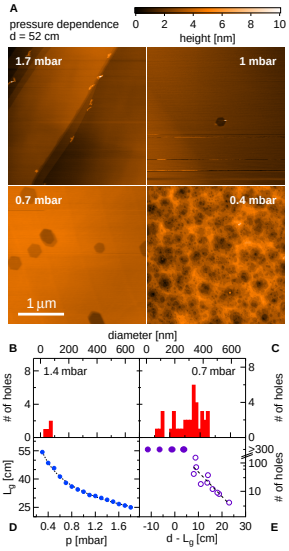

Figure 4.2: **Pressure dependence of graphite plasma exposures** (A) AFM images (tapping mode) of graphite surfaces for various p, as indicated, exposed for one hour at $d = 52\,\mathrm{cm}$, shown on the same color scale. All panels are $3 \times 3\,\mu\mathrm{m}^2$, the scale bar is $1\,\mu\mathrm{m}$. (B,C) Histograms from $10 \times 10\,\mu\mathrm{m}^2$ scans, displaying the number of holes against hole diameter (bin size 20 nm) for p as labeled. (D) Length L_g of the optically visible plasma as a function of p. The dashed curve is a $1/\sqrt{p}$ fit. (E) Number of holes versus distance from plasma edge $d - L_g$. A lower bound of 300 holes is given for the heavily etched cases where an exact hole-count was not feasible. The dashed black line is an exponential fit to the data with < 300 holes.

where ubiquitous and deep etching is seen, demonstrating the strong influence of p. Analyzing the etch pits using histograms confirms that p and d have a similar influence on the etching process, compare Fig. 4.2B, C with Fig. 4.1B-D. In addition, Figure 4.1E summarizes the histograms of all investigated graphite samples, using color to represent the num-

ber of holes, while the size of each marker is proportional to the width of the distribution of hole diameters. A clear correlation between the number of holes and the width of the distribution is seen, i.e. the largest circles (large width of distribution) are all red (large number of holes), while small circles are purple. This means that a large ion flux (creating holes) goes together with large radical flux (large anisotropic etch rate).

The analysis of the graphite exposure data leads to two qualitatively different types of processes: the direct and the remote plasma regime. In the direct plasma regime (large, red circles, Fig. 4.1E), the sample is located directly within the plasma discharge region, hence exposing it to large densities of radicals and ions, capable of inducing defects. In the remote plasma regime (small, purple circles, Fig. 4.1E), on the other hand, the sample is positioned outside, downstream of the plasma generation region, where ions have recombined and only a residual flux of radicals is present. There, anisotropic etching proceeds predominantly from preexisting defects and step edges, leaving the basal planes mostly untouched.

Further, there is an intimate connection between distance and pressure: lower pressure results in a longer gas mean free

path and therefore a larger average distance for recombination in the diffusive gas. This results in a larger size $L_g(p)$ of the plasma, measured from the edge of the visibly glowing plasma to the surfatron, see Fig. 4.2D. Thus, changing the pressure with fixed sample position modifies the distance between sample and plasma edge. Hence, it is useful to introduce an effective distance $d' = d - L_g(p)$, the distance from sample to the edge of the glowing plasma. Thus, $d' \lesssim 0$ roughly marks the direct plasma regime while $d' \gg 0$ signifies the remote plasma regime. Reactive particles are generated inside the plasma column and start recombining once they have left the plasma generation region.

The reaction kinetics in low temperature H-plasmas are highly non-trivial despite the relatively simple chemical composition[89]. Nevertheless, it is well known that at the pressures used here ($p \sim 1\,\mathrm{mbar}$), the predominant radical decay mechanism is mainly surface mediated association rather than gas collisions. Two colliding H atoms require a third body to carry away the excess energy for association to occur [126]. However, under the present conditions, three body collisions are very unlikely, thus leaving only the surface assisted process (which also leads to surface

heating[77]). Recombination of ions, in contrast, can also occur through through an additional collisional channel, in absence of a surface. Which species – ions or radicals – decay on a shorter length scale downstream of the plasma edge thus depends on both the surface properties and gas parameters. For anisotropic etching without defect creation, a flux of H radicals in absence of ions is needed, thus requiring the ion density to decay on a shorter length than the radicals.

The surface-attenuation of hydrogen thus plays an important role, and was previously studied [77, 127]. Quartz – as used in our experiments – was identified as a material with a relatively low recombination coefficient, particularly compared to some common metallic surfaces (stainless steel, Aluminum). This weak surface attenuation can open a downstream window offering a flux of H radicals (not decayed yet) in absence of ions (almost all decayed), as desired and achieved here, see e.g. Fig. 4.1B and 4.2B. We note, however, that even a relatively small amount of metallic deposition on the surface of the tube can significantly enhance the surface decay of radicals, and potentially close this window, i.e. the radicals decay before the ions.

To study the decay of the reactive species, we note that the ion intensity is proportional to the number of holes created, shown in Fig. 4.2E as a function of distance from the plasma on a log-lin plot for all 5×4 combinations of p and d parameters. We find a roughly exponential decay with distance, with a $1/e$ decay length of about 5 cm. A similar decay is seen for the width of the diameter distribution, which is also proportional to the ion intensity (see SOM), giving the same decay length within the error bars. The decay is expected to saturate once the intrinsic, preexisting graphite defect density is reached. Further, changing p also alters the decay length by affecting the mean free path and diffusion constant [77], but for the narrow range of pressures used in the present data set, this is not a very large effect.

The anisotropic etch rate, on the other hand, is related to the intensity of H radicals. However, the presence of ions (in most of the present (d, p) data set) can enhance the etch rate, impeding extraction of the decay length of radicals. Nevertheless, we extract the anisotropic etch rate, defined as the growth per unit time of the radius of a circle inscribed to the hexagonal etch pit, averaged over several holes, shown in Fig. 4.4A. Only the largest set of hexagons of each exposed

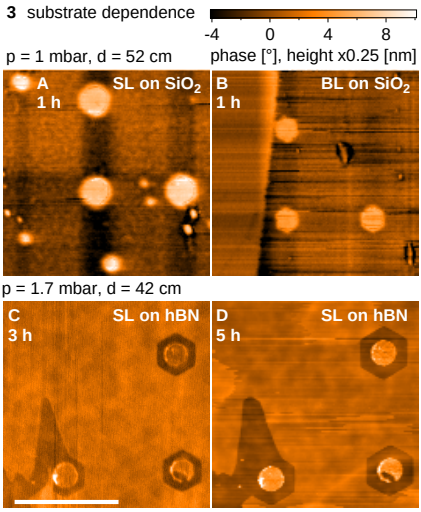

Figure 4.3: **SL/BL and substrate dependence**(A,B) AFM phase contrast images of a SL (A) and BL (B) section of the same flake on a Si/SiO_2 substrate, etched for 1 h at $T = 450\,°C$. Holes of 50 nm diameter were defined before etching. (C,D) AFM topography images of a SL flake on hBN etched for 3 h (C) and 5 h (D). Holes of 200 nm were defined before etching. All images are $2 \times 2\,\mu m^2$, the scale bar is $1\,\mu m$.

graphite sample were evaluated to obtain the etch rate, since smaller holes might not have etched from the beginning of the exposure. As expected, the anisotropic etch rate is largest for small distances, falling off with increasing separation from the plasma edge.

4.4 SL and BL graphene etching

Next, we study the plasma exposure of single layer (SL) and bilayer (BL) graphene exfoliated onto a SiO_2 substrate using the established tape method[4]. We patterned disks using standard e-beam lithography (EBL) and reactive ion etching with an Ar/O_2 plasma, resulting in circular graphene holes which were subsequently exposed to the remote H plasma. BL graphene grows regular hexagons with parallel sides (see Figure 4.3B), as expected from the graphite results. The SL, on the other hand, displayed mostly round holes (see Figure 4.3A), though some weakly developed, irregular hexagonal shapes are also occasionally seen. Further, several additional, not EBL defined holes appear on the SL after exposure, all smaller than the EBL initiated etch pits. After a second plasma exposure, the number of holes increased further, indicating generation of new defects, while only the EBL defined holes are seen on the BL. In addition, the average hole diameter on SL is visibly larger than on the BL (Figure 4.3A and B), indicating a faster etch rate on SL. Thus, the plasma is clearly more reactive and no longer anisotropic when exposed to SL on SiO_2. This was previously reported[23, 27],

and attributed to the well known charge inhomogeneities in the SiO_2 substrate[128–130]. Note that the SL and BL regions shown in Figure 4.3A and B are located on the same graphene flake, ensuring identical plasma conditions. A broad range of plasma parameters in the remote regime were investigated for SL and BL samples on Si/SiO_2, giving qualitatively similar results (isotropic SL etching).

The etch rate for SL and BL on SiO_2 is shown in Fig. 4.4B. For the SL samples, only the EBL defined holes were evaluated, ignoring the plasma induced defects, since these do not etch from the beginning of the exposure. Clearly, for all plasma parameters studied, SL exhibits a significantly larger etch rate compared to BL [23, 27], as already visible from the AFM images in Fig. 4.3A,B. For the SL and BL samples on SiO_2, the scaling of etch rates is not seen, presumably due to variations in the SiO_2 substrates. Thus, the SL/BL etch rates are shown as function of location d, see Figure 4.4B.

4.5 Substrate dependent etching

To study the substrate dependence, we investigate SL graphene on high-quality hexagonal boron nitride (hBN)

crystals, obtained from the Taniguchi group (NIMS, Japan), see Ref. [18]. SL and BL graphene were aligned and deposited onto areas covered with serval 10 nm thick hBN lying on a SiO_2 substrate, following the recipe of Ref. [19]. Then, the same fabrication steps were repeated as before to fabricate circular graphene holes. Figure 4.3C shows an AFM topography image of a SL on hBN after 3 h exposure, Figure 4.3D after five 5 h. Clearly, regular and well aligned hexagonal holes are visible, indicating a highly anisotropic etch. This is also seen for BL on hBN, giving roughly the same etch rate as SL (not shown). The amplitudes of charge fluctuations are considerably smaller in hBN compared to SiO_2[129, 130], and overall doping is expected to be small, reducing the reactivity of graphene compared to Si/SiO_2 substrates [23, 27, 131].

The growth of the hole radius (inscribed circle) as a function of exposure time is shown in Fig. 4.4D. A linear fit (dashed red) is clearly of poor quality, deviating from the data by more than a standard deviation. (The solid blue curve is a tanh fit show as a guide for the eye). Hence a constant etch rate – corresponding to a reaction rate limited model with abundant H radicals – can probably be excluded, hinting

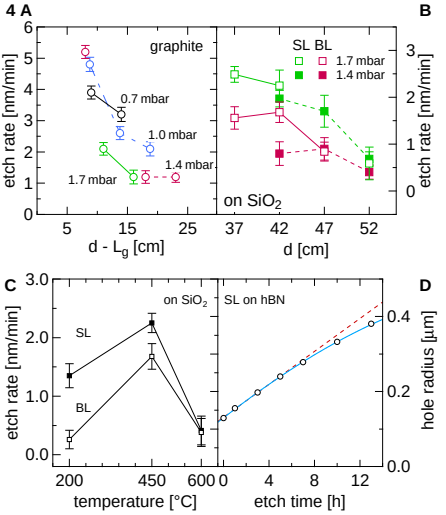

Figure 4.4: (A) Graphite anisotropic etch rate versus normalized distance d' for several configurations. Only points based on several holes allowing reliable etch rate extraction are shown. (B) Etch rate of SL and BL on Si/SiO_2 at indicated parameters. (C) Temperature dependence of the etch rate of SL and BL samples on SiO_2. (D) Average radius of a circle inscribed to the hexagonal etch pit as a function of exposure time for SL on hBN. Error bars are of the size of the markers or smaller. The dashed red line is a linear fit to the points at $\leq 5\,h$, the blue curve serves as a guide for the eye.

again towards a rate limiting H atom supply, assuming that the etching process is not qualitatively changing over time. Valuable information might be obtained from increasing the H radical density, e.g. with a larger gas flow or larger RF power.

The EBL defined circles stand very clearly visible in the center of the hexagons as an elevated region in Fig. 4.3C and D, growing in height but not diameter upon further H-plasma exposure. They appear also away from the graphene flakes directly on the hBN, wherever circles were EBL/Ar/O_2-plasma defined. More work is required to investigate the composition of these surface growths. In addition, the adhesion of graphene to the hBN surface appears to be rather poor, leading to the formation of some bubbles of small height. The bubble arrangement and severity varied after each plasma exposure step, tending to worsen over time. On one sample, the entire graphene flake of several micron size was tilted, clearly visible in the location of the graphene hexagons with respect to the circular pillars, possibly caused by AFM tip forces or at elevated temperatures.

Raman spectroscopy and temperature dependence was also investigated on SL and BL samples on hBN, before and after H plasma etching. Away from the edges, the D and D' disorder peaks were not seen, both before and after H plasma etching. This suggests that neither defect formation nor hydrogenation[28, 66, 132] is occurring in the bulk 2D during plasma etching, opening the door for high quality elec-

trical properties. On the etched perimeter, however, clear disorder peaks were observed, which could in principle be used to further investigate edge properties[71]. The center circles exhibit clear hBN features in the Raman spectra. The temperature dependence of the etch rate is shown in Figure 4.4C. The etch rates are strongly reduced at temperatures far above and below the process temperature, consistent with previous reports [23, 27].

4.6 Conclusion

In conclusion we have demonstrated the pressure and distance dependence of the anisotropic etching of graphite and graphene in a H plasma. In the remote region of the plasma ($d' > 0$) etching only occurs at present defect sites whereas for $d' < 0$ new defects can be induced, resulting in larger etch rates. Further, we have shown that the anisotropy of the etch is strongly influenced by the length scale and amplitude of the charge inhomogeneity in the substrate. Especially for SL graphene on SiO_2 the anisotropy is heavily reduced and further, the reactivity of the sheet is substantially enhanced. We have shown that this influence on the anisotropy of the

etch is drastically reduced by introducing an hBN flake in between the SiO_2 substrate and the graphene.

4.7 Acknowledgements

We would like to thank R. Maurand, B. Eren, R. Steiner and O. Yaziev for helpful discussion and support. This work was supported by the Swiss Nanoscience Institute (SNI), NCCR QSIT and Swiss NSF.

Chapter 5

Influence of a Pure H Plasma on the Mobility of SLG

The change of the mobility of SL graphene samples is investigated by performing transport measurements in different environments. One set of samples is measured in air, in vacuum and after thermal annealing in vacuum. Thermal annealing increases the sample quality, however strong shifts of the Dirac peak to negative values are observed. The second set of samples is measured in vacuum after fabrication, after thermal annealing at $400^\circ C$ *in hydrogen gas and after hydrogen plasma exposure at* $400^\circ C$*. Thermal annealing in hydrogen gas and exposure to a hydrogen plasma degrade the qualtiy of the graphene samples, most probably due to copper contaminants in the quartz tube employed.*

5.1 Introduction

Graphene sheets are heavily susceptible to charged particles in their vicinity, strongly influencing the transport properties through the flakes [106, 133]. Especially the substrate underneath, as well as fabrication residues sticking to the flake surface, disturb the intrinsic properties of graphene in an uncontrollable way [15]. Nevertheless, there are different possibilities to reduce their impact on the graphene measurements: suspended graphene flakes, fixed only by the contacts, have revealed extremely high mobilities and opened the door to the investigation of electron-electron interaction effects in graphene [16, 134–136]. Also, thermal [65, 106] and current annealing of graphene samples on substrate [17] and suspended [16] has shown to drastically reduce the disorder, minimizing the doping and shifting the Dirac peak closer to zero back gate voltages.

Similar to the disorder induced by the substrate or molecules on the sample surface, rough edges of graphene nanoribbons are predicted to strongly localize charge carriers, heavily disturbing the electrical transport measurements through the sample [60]. Reducing their disorder on a atomic level is ex-

pected to positively influence the transport measurements [9, 55]. Graphene is known to chemically interact with hydrogen atoms, forming hexagonally shaped holes at either pre-defined or intrinsic defects in the graphene sheet [23, 124]. The edges of the hexagonal holes are formed in the zigzag crystal orientation of the graphene sheet, paving the way for the fabrication of crystallographically edged graphene nanoribbons [23]. However, exposure of graphene to hydrogen atoms can also lead to the transformation of the graphene sheet into insulating graphane [28, 132, 137]. Still, thermal annealing of graphane samples have shown a reduction of the density of sp^3 carbons in the system, gradually transforming graphane back to the starting material graphene with increasing annealing temperature [28, 137]. Interestingly, the exact configuration of the plasma seems to be crucial for the hydrogenation of the flakes. In the experiments performed by Diankov and co-workers, the Raman investigations have not shown the presence of a D'-peak, arising in the presence of sp^3 carbon species [27].

When graphene nanoribbons are fabricated using a hydrogen plasma, it is therefore important to investigate the influences of the thermal annealing, as well as possible hydrogena-

tion processes during hydrogen plasma exposure on the electronic properties of the graphene samples. Here, the change in the mobility of graphene flakes due to thermal annealing and plasma exposure is examined. The mobility of the samples at 4.2 K is first measured in a dipstick and further compared to the mobility data acquired in vacuum, before and after annealing, investigating the influence of deposited gas molecules on the graphene surface. In a next step, the samples are annealed in hydrogen atmosphere in the CVD oven used for the later hydrogen plasma exposure, before mobility measurements are performed at 4.2 K. Hence, the influence of the annealing in hydrogen atmosphere can be compared to changes related to the plasma exposure. Finally, the samples are exposed to a pure hydrogen plasma and again measured in vacuum at 4.2 K.

The experiments shown in section 5.3.2 are performed in a copper contaminated quartz tube, probably influencing the interaction of the H atoms with the graphene surface. Chemical etching of graphitic surfaces in the copper polluted tube is uncontrolled. In chapter 4 a clean tube is employed and anisotropic graphitic etching is reproducible.

5.2 Sample fabrication and methods

The graphene samples were fabricated by exfoliation of natural graphite and subsequent deposition onto a SiO_2/Si as explained in the appendix. Contacts were patterned onto the flakes employing standard e-beam lithography and metal evaporation techniques (see appendix). For the contact metal either chromium/gold (subsection 5.3.1) or palladium (subsection 5.3.2) was employed. During exposure of the samples to the hydrogen plasma, the chromium/gold contacts became insulating (see below). Therefore, for the sample exposed to the plasma, the contact metal was changed to palladium.

The measurements depicted below, are four terminal van der Pauw measurements and are conducted using standard lock-in technique, flowing an AC current of 1 nA at a frequency of 133 Hz. Further, for the van der Pauw measurements performed in subsection 5.3.2, two sets of two lock-ins, acquiring data at two different frequencies (133 Hz, 211 Hz respectively), were used to probe the back gate dependence of the charge carrier density in the sample.

5.3 Mobility measurements under various conditions

5.3.1 Graphene mobility before and after thermal annealing

First, the dependence of the resistivity on the back gate voltage of the as prepared samples were measured in a dipstick at 4.2 K and $B = 0$ T. In Fig. 5.1, the data of one of the three as fabricated flakes measured is depicted, reflecting the general behavior of the samples. All three flakes are located on the same chip and were processed in the same run.

As shown in Fig 5.1A, the resistivity of the as prepared flake (dark blue trace) is strongly shifted from the charge neutrality point to a back gate voltage of around 12 V, indicating the presence of dopants. However, in panel D (dark blue trace), the mobility calculated using the field effect method is shown, reaching expected mobility values for graphene flakes on substrate [4]. As mentioned in chapter 3, most probably air molecules froze on top of the flakes during cool down, introducing charges, visible in the measurements. Therefore,

cooling the sample down in helium atmosphere should lead to a change of the doping of the flakes.

The sample is built into the VTI, which is pumped down to approximately $2.3 \cdot 10^{-2}$ mbar. Before cool down, ca. 5 mbar exchange gas (He) is filled into the VTI, to allow thermalization of the VTI with the liquid helium bath in the measurement dewar. Hence, the graphene substrate was mainly exposed to helium during cool down.

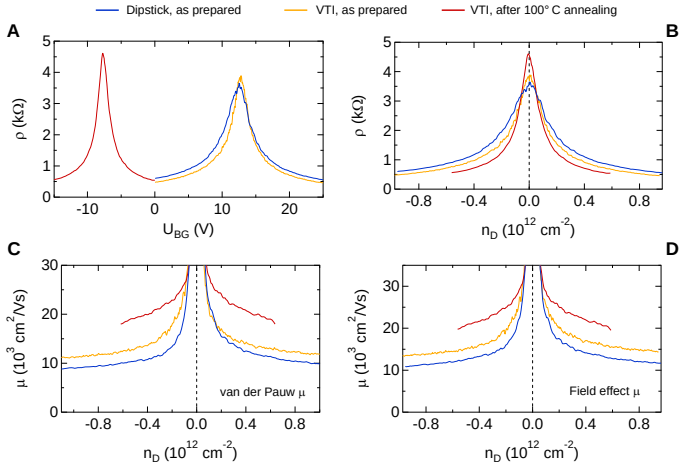

Figure 5.1: Influence of thermal annealing in vacuum on the mobility of graphene flakes. All measurements shown here are acquired at 4.2 K. Panel A: resistivity of the same flake measured as farbicated in a dipstick and in a VTI, as well as after thermal annealing at 100° C in vacuum (VTI). Panel B: resistivity of the investigated flake against charge carrier density.

The light blue traces in Fig. 5.1 depict the van der Pauw resistivity (panel A and B) and the field effect mobility (panel C) of the sample at 1.4 K, measured in the VTI. The position of the Dirac peak has not changed strongly (panel A), however its height is slightly larger and its width smaller compared to the dipstick measurements (see panel B of Fig. 5.1). The height and width of the resistivity peak can be altered by charge inhomogeneities in the substrate or charged molecules on the graphene flake, inducing a variation of the charge density throughout the probed region of the flake. When probing the resistivity in graphene an average value of ρ is obtained at each back gate value. Due to the variation of the charge density in the flake, the total resistivity is smaller than for graphene not subjected to charge inhomogeneities. Hence, reducing the charge density variation throughout the flake can increase the value of ρ [108, 113]. Frozen molecules on the sample surface might play a minor role for the induction of disorder into the graphene samples. Polar molecules, chemically bound or adsorbed to the sample surface, probably alter the charge distribution in graphene with higher impact. An effective way to release such particles is the thermal annealing of graphene samples [65, 106].

To investigate the influence of temperature on the mobility of the samples, the VTI was warmed up to RT, followed by a 5 hrs thermal annealing of the sample in situ at 100° C. During the annealing process, the resistivity in dependence of the applied back gate voltage was traced, clearly indicating a strong shift of the Dirac peak towards lower back gate voltages (see panel A in Fig. 5.1). Interestingly, the peak position did not stabilize around $U_{BG} = 0$, but moved further to negative values. Plotting the resistivity against the charge carrier density (see Fig. 5.1), nicely shows further improvement of the sample quality, compared to the measurements acquired beforehand. Also the field effect mobility of the thermally annealed sample is clearly higher than for the as prepared sample.

The shift of the Dirac peak to negative back gate values could be due to the deposition of additional molecules with opposite polarity, instead of a desorption process of absorbed particles [106, 138]. During thermal annealing of the sample, the IVC was constantly pumped and the pressure at the sample was monitored. During temperature increase from RT to 100° C, the pressure inside the IVC rose from $1.31 \cdot 10^{-2}$ mbar to around $1.81 \cdot 10^{-2}$ mbar. A pressure rise indicates the release

of molecules, however it is not clear whereof. Either molecules could desorb from the graphene surface or from components inside the VTI due to out-gasing. Therefore, the change of the Dirac peak position cannot clearly be assigned to the release of desorbed molecules from the sample surface. Further, as explained in [138], ion gauges can release molecules influencing the resistivity measurements of graphene. However, here, a Pirani gauge was used to measure the pressure, not effectively ionizing the gas particles, in contrast to the experiments performed in [138].

The sharpening of the peak and the increase in resistivity and field effect mobility (see panels B and D in Fig. 5.1) indicate smaller amount of charge inhomogeneity in the sample [108]. For larger ratios of point defect densities n_p versus charged impurity densities n_i, $\frac{n_p}{n_i}$, the mobility of the flakes increases [108]. Hence, if the density of charged impurities decreases, the ratio $\frac{n_p}{n_i}$ increase, indicating an rise in the mobility values. Most probably, charged or polar molecules influencing the charge inhomogeneity in the graphene sheet, desorbed from the flake surface. The negative charges leading to the shift of the Dirac peak to $U_{BG} < 0$ could come from molecules bound more strongly to the surface or point defects in the substrate.

To completely remove fabrication residues from the graphene surface, the flakes are usually heated to 400°, C [65, 106]. The VTI employed here is specified to heat up to 400 K, therefore, the thermal annealing experiments are conducted at 100° C, close to the maximum temperature, keeping in mind that probably not all the particles are removed. After investigating the changes in mobility due to thermal annealing, the influence of a plasma process on the graphene flakes was investigated. It has been shown by Elias and co-workers that a plasma exposure of the graphene flakes can induce defects, increasing the concentration of sp^3 bound carbon atoms, hence leading to the formation of graphane [28]. Also, transport measurements at $B = 0\,\mathrm{T}$ clearly show a degradation of the flakes. In the next subsection, the influence of the plasma used here on the transport measurements of the flakes are investigated.

5.3.2 Electrical measurements of graphene samples after plasma exposure

As mentioned above, the samples measured here are contacted with palladium contacts. During exposure of samples

with chromium/gold contacts to the hydrogen plasma, the contacts became insulating, indicating a reaction of the hydrogen with the metallic contacts. The conductivity of a thin gold film is reduced by implantation of hydrogen or helium, as shown by Soltan and co-workers [139]. Palladium, conversely, did not show the same type of interaction with the hydrogen atoms in this experiment, still being conductive after hydrogen exposure.

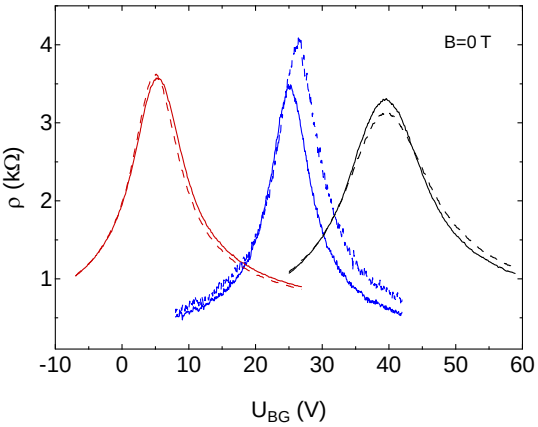

Figure 5.2: Dirac peak position of the as prepared flake (blue), after thermal annealing in a CVD oven in hydrogen atmosphere (red) and after plasma exposure in a CVD oven (black). The solid lines indicate measurements taken in region A of the flake shown in Fig. 5.4 and the dashed lines correspond to measurements in region B in Fig. 5.4. Clearly, the positions of the Dirac peak do not coincide, however, after each treatment, the peak values approach each other.

First, van der Pauw measurements of the graphene flakes after fabrication are acquired (see Fig. 5.3A1 and 5.3B1, blue traces). Both sets of measurements are taken on the same flake (Fig. 5.4A (phase images)) in the regions A and B. Panel A depicts the flake after fabrication, covered by dirt particles, most probably PMMA residues. The size of the particles is probably smaller than suggested by the image in panel A, as the AFM tip might be polluted. All the residues on the flake have the same triangular shape and similar sizes on the height images (not shown), pointing towards a polluted AFM tip. The Dirac peaks are slightly shifted to 26 V from zero back gate voltage, indicating strong hole doping of the flake (see Fig. 5.2). The shift is slightly different in the two graphene regions (solid lines: region A, dashed lines: region B), consequently, the doping in the two parts of the flake is distinct.

Panels A2 and B2 in Fig. 5.3 display the mobilities of the samples after fabrication (blue traces), calculated using the Hall voltages measured in the van der Pauw geometry at $B = \pm 0.2\,\mathrm{T}$. As for the resistivities, the mobilities in the two regions are different, showing higher values in region A, in accordance with the lower resistivity at high charge carrier densities.

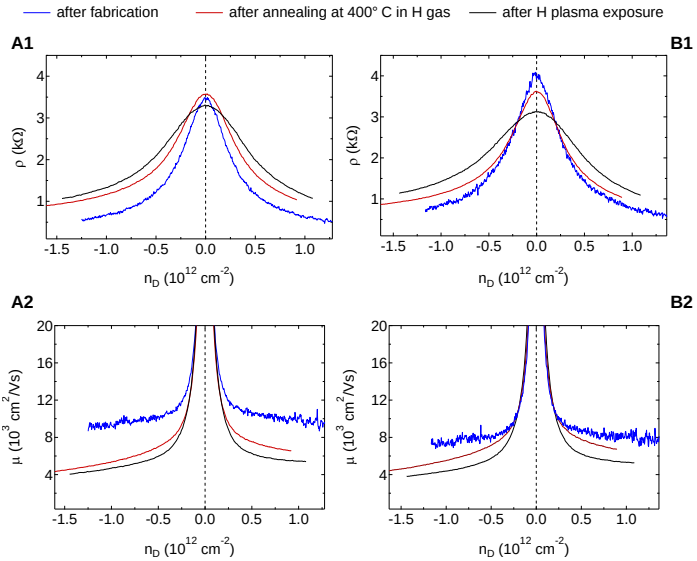

Figure 5.3: Resistivity and mobility measurements of the as prepared sample (blue), after thermal annealing in the CVD oven in H atmosphere (red) and after plasma exposure (black). The mobilities were calculated using the van der Pauw method.

Next, the samples are built into the quartz tube in the CVD oven depicted in Fig 2.15 at a distance $d = 42\,\mathrm{cm}$ and the system is pumped to a pressure of approximately $p = 5 \cdot 10^{-3}\,\mathrm{mbar}$. The hydrogen flow through the system is turned on at a system temperature of $T = 125°\,\mathrm{C}$ and the working pressure inside the tube is adjusted to $p = 0.4\,\mathrm{mbar}$ using a speedy-valve. Then, the sample is annealed at $T = 400°\,\mathrm{C}$

during 15 min without ignition of the plasma. The annealing time is defined between the moment the oven reached the set temperature of 400° C and the point where the oven is turned off and opened for cool down. Therefore, the sample is effectively exposed to temperatures between $200 - 400°$ C for approximately 60 min more. The sample is held in hydrogen atmosphere until the CVD oven has cooled down to 50° C.

In Fig. 5.3 the red traces show the change of the resistivity and the mobility after the annealing step in the plasma oven. Again, the two region are depicted in panels A and B respectively. The resistivity in the two regions have approximated each other to a similar value of approximately $\rho = 3\,\mathrm{k}\Omega$. Also, the shift of the Dirac peak from $U_{BG} = 0\,\mathrm{V}$ decreased strongly, amounting after the annealing step to about $U_{BG} = 4\,\mathrm{V}$, as seen in Fig. 5.2, red traces. The AFM image of the flake after thermal annealing is shown in Fig. 5.4 and indicates less particles on the flake surface. However, the overall value of the resistivity, as well as of the mobility has decreased, pointing to a larger amount of Coulomb scatterers and point defects. It might be due to interaction of the graphene with copper particles inside the CVD quartz tube, coming from CVD graphene growth processes

performed in the same tube. Copper is slightly less electronegative than carbon, thus the graphene flake becomes electron doped, shifting the Dirac peak to lower back gate values.

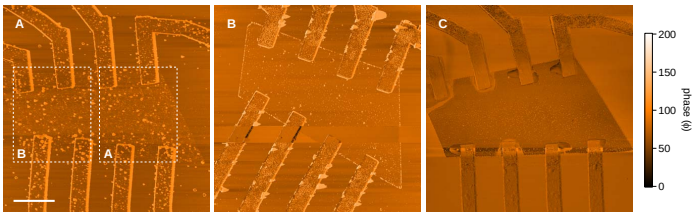

Figure 5.4: AFM images of the sample investigated here. Phase images are shown as the topography scans do not clearly depict the differences between the individual process steps. All scans are of the same size and the scale bar in panel A is 2 μm long. Regions A and B are outlined by the white dashed boxes surrounding the contacts used to perform the measurements. Panel A: sample after fabrication, before measurements. Panel B: Sample imaged after thermal annealing. Panel C: Sample after exposure to the hydrogen plasma in the CVD oven.

Further, the sample was built into the same CVD system as for the thermal annealing step at 400° C and subsequently exposed for 15 min to a pure hydrogen plasma at a distance $d = 42$ cm and at a system temperature of $T = 400°$ C. The hydrogen gas pressure was set to $p = 0.4$ mbar and the plasma power amounted to $P = 40$ W. The sample resides in the

down stream region of the plasma in this setup. The settings for the plasma exposure in this experiment cannot be compared to the plasma conditions specified in chapter 4, as the quartz tube used here was exchanged for a clean and slightly smaller tube in chapter 4. In Fig. 5.3 the black traces show the measurements of the sample after the plasma exposure. Clearly, the resistivity of the flake decreased and the Dirac peak is visibly broader than before (see Fig. 5.3). Also, the peak is shifted to approximately 38 V in back gate voltage, indicating strong doping of the flake, as depicted in Fig 5.2. Further, the mobility of the flake is slightly lower than after the thermal annealing step, again indicating the degradation of the flake.

Most probably, the graphene flake interacts with the hydrogen radicals, generated in the plasma, forming graphane [28, 137]. As explained in chapters 2.3.24, the hydrogen radicals and ions in the down stream region of the plasma can bind to the graphene surface, forming locally insulating graphane. Raman spectra taken after the hydrogen exposure, see Fig. 5.5, clearly show the rise of a D and a D' peak, indicating the presence of sp^3 bound carbon in the system [28, 66, 134]. However, in hydrogen-graphite

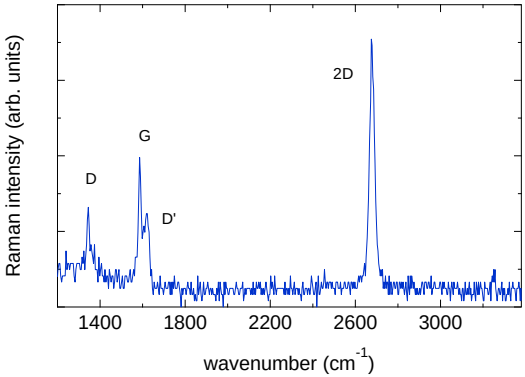

Figure 5.5: Raman measurement of the sample after hydrogen plasma exposure. The *D* peak clearly indicate the presence of defects, which are, in this case, hydrogenated carbon atoms in the hexagonal lattice of graphite.

interaction experiments performed in a clean quartz tube, no hydrogenation of the flakes were observed (see chapter 4). Hence, the copper contamination of the tube has a strongly negative influence on the mobility of the graphene flakes.

5.4 Conclusion and outlook

The samples investigated here, indicate that thermal annealing in vacuum (VTI) leads to an increase of the sample quality visible in the rise of the mobility and sharpening of the

resistivity peak. Further, an additional sample doping is observed when annealing the samples at 100°C in situ, leading to strong shifts of the Dirac peak to negative back gate values.

Thermal annealing in hydrogen gas environment at 400° C, without plasma ignition, however, seems to have a negative impact on the transport properties of the flakes, enlarging the Dirac peak slightly and shifting it closer to $U_{BG} = 0$. Exposing the flakes further to a hydrogen plasma, additionally degrades the graphene flakes and, according to the Raman measurements, forming partially hydrogenated graphene. Most probably,the copper polluted quartz tube is responsible for the doping of the flakes.

For future experiments, the quartz tube employed for annealing and cleaning purposes of the graphene flakes should be clean. The Copper particles influence the doping as well as the quality of the flakes and should clearly be avoided. On the other hand, controlled hydrogenation of graphene flakes has been shown and could also be interesting for the fabrication of thin, conductive graphene nanoribbons with a band gap [140–142].

Chapter 6

Pure H low T plasma exposure of HOPG and graphene: Graphane formation?

B. Eren, D. Hug, L. Marot, R. Pawlak,

M. Kisiel, R. Steiner, D. M. Zumbühl, E. Meyer

The content of this chapter has been published in Beilstein Journal of Nanotechnology: B. Eren et al., *Pure H low T plasma exposure of HOPG and graphene: Graphane formation?*, Beilstein Journal of Nanotechnology **3**, 852 (2012)

6.1 Abstract

Single and multilayer graphene and highly ordered pyrolytic graphite (HOPG) were exposed to a pure hydrogen (H) low temperature plasma (LTP). Characterizations include various experimental techniques such as photoelectron spectroscopy, Raman spectroscopy and scanning probe microscopy. Our photoemission measurement shows that H LTP exposed HOPG has a diamond-like valence band structure, which anticipates double side hydrogenation. With the scanning tunneling microscopy technique, various atomic scale charge density patterns were observed, which might be associated with different C-H conformers. H LTP exposed graphene on SiO_2 has a Raman spectrum in which the D peak to G peak ratio is over 4, associated with hydrogenation on both sides. A very low defect density was observed by the scanning probe microscopy measurements, which enables a reverse transformation to graphene. H LTP exposed HOPG possesses a high thermal stability, and therefore, this transformation requires annealing over 1000° C.

6.2 Introduction

As being an sp^2-hybridized single layer of carbon atoms arranged in a densely packed honeycomb lattice with a true atomic thickness (Fig. 6.1a), graphene possesses unusual electronic and mechanical properties [3, 143]. A new perspective is the chemical modification of graphene, especially the incisive idea of attaching atomic hydrogen to both sides of the graphene lattice to produce graphane (Fig. 6.1b); an sp^3-hybridized insulating derivative of graphene [28, 132, 144, 145]. Graphane offers a brand new playground for physicists and engineers, particularly as a prospect for two dimensional electronic applications. Nanowire [146] or transistor concepts consisting of only graphene and graphane could be realized. Another possible application is its characteristic for hydrogen storage. It has a volumetric capacity of 0.12 kg H_2/L which is higher than the Department of Energy target of 0.081 kg H_2/L for the year 2015 [132].

A prerequisite for graphane synthesis is the abundance of atomic hydrogen to react with unsaturated C-C bonds of graphene; subsequently leading to C-H bond formation on both sides of the graphene. The elegant yet simple solu-

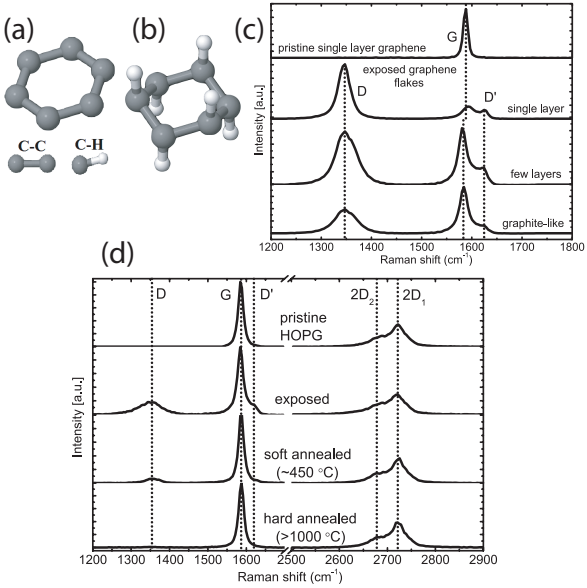

Figure 6.1: The two dimensional material consisting of carbon atoms in honeycomb orientation, graphene (a), loses its sp^2 hybridization upon hydrogenation from both sides resulting into its insulating derivative, graphane (b). This transformation might be achieved with a pure hydrogen LTP exposure, which results in a D:G height ratio of 4.5 in the Raman spectrum of single layer graphene (c). The sample was kept at 450° C during 5 minutes of exposure, where the same plasma exposure results in a smaller D:G ratio for multilayer graphene (c) and for HOPG (d), due to contributions from pristine layers beneath hydrogen implantation depth. Soft annealing at 450° C diminishes the D and D' peaks; however a complete supression, which signifies reversibility to graphene, is achieved only after an annealing over 1000° C.

tion to obtain such a chemisorption may be to use a pure hydrogen low temperature plasma (LTP) with a typical average electron temperature (T_e) of 2-5 eV, where the hydrogen would be easily dissociated (required energy as T_e: 4.52 eV) and chemisorbed on the surface, and a small portion will be ionized (required energy as T_e: 13.6 eV). The atomic ion implantation might also hydrogenate the other side of the surface layer and even some other subsurface layers. The 3.5 eV plasma used in this work results in an ion impact energy (ϵ_i) of 12.6 eV on the sample surface. With this technique, proton deposition energies can be obtained which are high enough to overcome the energy barrier (3.7 eV) to penetrate the center of the hexagonal carbon [147], without physically sputtering (36 eV) the carbon atoms [91, 148, 149]. Moreover hydrogen ions can even be implanted deeper into the first 4-5 layers of HOPG, suggested by the SRIM simulations [150].

The question is: Will graphane form after the plasma exposure and if it does, is it possible to distinguish its existence from other possible surface rearrangements caused by the exposure? Before starting, it should be clearly stated that graphane is a reserved word for graphene which is fully hydrogenated from both sides. In reality, there will always

be hydrogen deficiencies and point defects and the obtained material would not be a perfect graphane. Therefore, hydrogenated graphene will be used for the rest of this article referring to a graphane-like structure.

The interaction of hydrogen with graphitic surfaces had been investigated various times in the last decades. The earlier research was concentrated on the physisorption of hydrogen molecule on such surfaces [151–153]. This was followed by theoretical [154], and experimental works focused on the chemisorption of atomic hydrogen [155–159]. A new research focus is the investigations of hydrogen containing plasmas with graphitic surfaces [28, 29]. Particularly the work of Elias *et al.* is interesting, in which graphane growth was claimed after exposure of free-standing graphene to a plasma containing 10% hydrogen [28]. In this work, single and multilayer graphene and highly ordered pyrolytic graphite (HOPG) were exposed to a pure hydrogen LTP and various techniques such as photoelectron spectroscopy, Raman spectroscopy and scanning probe microscopy were employed for characterizations. However, due to the insufficient electrical conductance, it was not possible to use photoelectron spectroscopy and scanning tunneling microscopy techniques

for graphene on SiO_2.

On the contrary to plasma treatments in previous works [28, 29], mixing a second gas was avoided in this work. Introduction of a high-Z gas such as argon would have cooled down the plasma due to increasing number of recombinations, which would have hindered hydrogen implantation. This might be the reason why graphane formation was claimed only for free-standing graphene by Elias et al. [28]. Moreover to this point, low energy argon ions also result in changes in the atomic structure of HOPG, and therefore are not desired in this work [160].

6.3 Results and Discussion

6.3.1 Raman spectroscopy

Raman spectroscopy is a frequently used tool for the analysis of graphitic materials. The Raman spectrum of graphite consists of the D and G peaks, around 1350 cm^{-1} and 1585 cm^{-1} respectively, which arise from vibrations of sp^2-hybridized carbon atoms [66, 161–163]. The D peak is caused by breathing-like modes corresponding to transverse

optical phonons near the K point of the Brillouin zone. It is an intervalley double-resonance Raman process which is initiated only by a deviation from the defectless two dimensional character [161–163]. On account of this, both hydrogenation and any kind of disorder manifest itself as the rise of this peak and a distinction between these two phenomena is not possible. Its overtone, the 2D peak which appears around 2700 cm^{-1}, is a second order process involving two inelastic scatterings and it is always present. The shape of this 2D peak is defined by the number of graphene layers (i.e. two peaks at 2682 cm^{-1} and 2723 cm^{-1} for graphite whereas a single peak at 2671 cm^{-1} for single layer graphene) [66]. The G peak represents the optical E_{2g} phonons at the center of the Brillouin zone. The cross-section for the C-C sp^3 vibrations, when available, are negligible for visible excitation.

Upon hydrogen plasma exposure on a single layer graphene (Fig. 6.1c 2^{nd} panel), a sharp D' peak around 1620 cm^{-1} appears as a result of intervalley double-resonance process due to deviation from the defectless two dimensional character as well as a D peak around 1350 cm^{-1}. The G peak preserves its position at 1585 cm^{-1} and a significant broadening

is not observed. The sharpness of these peaks signifies that amorphization is negligible [162]. A D:G height ratio of 4.5 is observed which anticipates a strong atomic rearrangement. In the work of Elias *et al.* [28], such a D:G ratio, being almost twice as much as of the ratio obtained after single surface hydrogenation, was interpreted as graphane formation. On the contrary to this, the plasma exposure on HOPG results in appearance of the D and D' peaks with lower relative intensities (Fig. 6.1d 2^{nd} panel), which we attribute to the contribution of the bulk layers where no hydrogenation takes place. This assumption is consolidated with the observation of a decreasing D:G ratio for increasing number of graphene layers which were simultaneously exposed to a hydrogen plasma (Fig. 6.1c 3^{rd} and bottom panels). The plasma exposure time between 5 and 60 minutes did not result in a significant difference in the Raman spectrum of the HOPG (not shown here). The D and D' peaks of the Raman spectrum of the hydrogen plasma exposed HOPG can be diminished or completely suppressed by annealing at 450 °C (soft annealing) for 30 minutes or over 1000° C for 10 minutes (hard annealing) respectively (Fig. 6.1d 3^{rd} and bottom panels). All annealings were performed in ultra high vacuum (UHV) conditions.

The latter value is around 200° C lower than the theoretical calculations [164], which predicts a full transformation from graphane back to graphene. On the contrary to Ref. [28], we did not observe a significant change of the Raman spectrum of LTP exposed single layer graphene after it is being annealed at 400° C for 24 hours in an argon atmosphere.

6.3.2 Atomic force microscopy

Though Raman spectroscopy is a strong tool for the analysis of graphitic materials, it does not provide a direct evidence of hydrogenation. In order to understand the nature of the D and D' peaks of the Raman spectra, Atomic force microsopcy (AFM) and photoemission spectroscopy of HOPG were conducted before and after exposing it to plasma. Although the pristine HOPG exhibits a relatively flat surface, the hydrogen plasma exposed HOPG shows two important differences: (i) The surface becomes rougher, (ii) blisters start to form which are more pronounced for longer time plasma exposures (Fig. 6.2a and b). Regarding these AFM measurements, it is clear that both surface roughening and blister formation contribute to D and D' peaks of the Raman spectrum. The

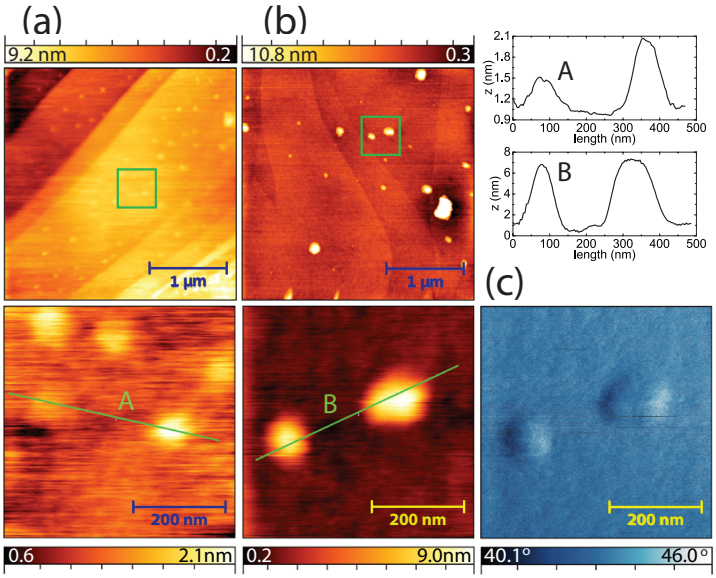

Figure 6.2: AFM measurements of the HOPG after hydrogen plasma exposure at 450° C, where round shaped blisters appear on the topography images of the HOPG surface, with a relative height depending on the plasma exposure time ((a) 5 minutes, (b) 60 minutes). Line profiles of two blisters in (a) and (b) are presented as A and B. Blisters also reveal a phase contrast different from the rest of the surface (c).

surface roughening can neither be attributed to the physical sputtering since the impact energy of the ions is well below theoretical threshold ($\epsilon_i \sim 36$ eV) [148, 149], nor the chemical etching which would have been forming large hexagonal pits [23, 165]. We think that, some of the implanted hydrogen (including molecular ions) recombines to form hydrogen gas intercalated between two graphite layers which builds up mechanical stress and deforms the entire surface. Moreover, this gas is free to diffuse in the lateral direction between the layers [166], which results in accumulation of hydrogen gas at certain points. Subsequently, the graphite layers start to deform more rigorously and blisters start to appear on the surface. The different phase contrast of the blisters from the rest of the surface suggests that they have different local elastic properties than elsewhere on the HOPG (Fig. 6.2c). It is, however, not clear whether these blisters still contain hydrogen gas underneath them during storage of HOPG in ambient conditions. Similar blister formation was observed after thermal sorption of hydrogen into graphite and hydrogen gas storage was claimed via thermal desorption experiments [167]. AFM topography images of single layer graphene on SiO_2 do not reveal any significant roughening or blister formation

(not shown here). The changes in the Raman spectrum of graphene is solely due to atomic rearrangements, either as a result of hydrogenation or corrugation in the atomic level. Since it was shown that low energy argon plasma treatment also results in similar atomic rearrangements due to corrugation [160], but no rise of the D peak [28], it can be claimed that hydrogen plasma treatment of the graphene layer results in its hydrogenation.

6.3.3 Photoelectron spectroscopy

X-ray and ultraviolet photoelectron spectroscopy (XPS and UPS) were used to monitor the changes in the core level and valence band structures of the HOPG after plasma exposure and subsequently after soft annealing. After exposure to hydrogen plasma, the core level C 1s spectrum gets broadened due to roughening, whereas it recovers its initial width after soft annealing (Fig. 6.3a). It was already stated that even there is a C-H bonding, this change in the shape of the C 1s peak is not due to a chemical shift as a result of this bonding, but is rather due the increase in the difference between upper valence band edge and the Fermi level (E_f) [168]. Such a

broadening was also observed for HOPG which was exposed to a low energy argon plasma, and the reason behind it was stated as geometrical defects (roughening) without any contribution from vacancy formation or hydrogenation [160]. In a similar manner, the broadening of the C 1s peak in our case is also due to displacement of the carbon atoms and its recovery is due to flattening after soft annealing. The satellite peak due to π-π^* transition exists for all the spectra (Fig. 6.3a inset).

As previously studied [168–170], the valence band spectrum of pristine HOPG (Fig. 6.3b upper panel) contains 5 peaks around 3.2, 5.3, 6.7, 8.5 and 14.2 eV below E_f. The peak at a binding energy (B.E.) around 14.2 eV is a secondary peak arising from photoelectrons scattered into unoccupied states. The peak at a B.E. of 3.2 eV is attributed to π-π^* transition which makes graphite a semimetal. The other three peaks lie where the π and σ bands overlap but they have their contribution mainly from the σ band. After exposure to hydrogen plasma, the UPS spectrum looks very similar to the spectrum obtained 20 years ago by Ugolini *et al.*, where HOPG was exposed to hydrogen ions of a Penning ion source [168]. Standalone from this spectrum (Fig. 6.3b

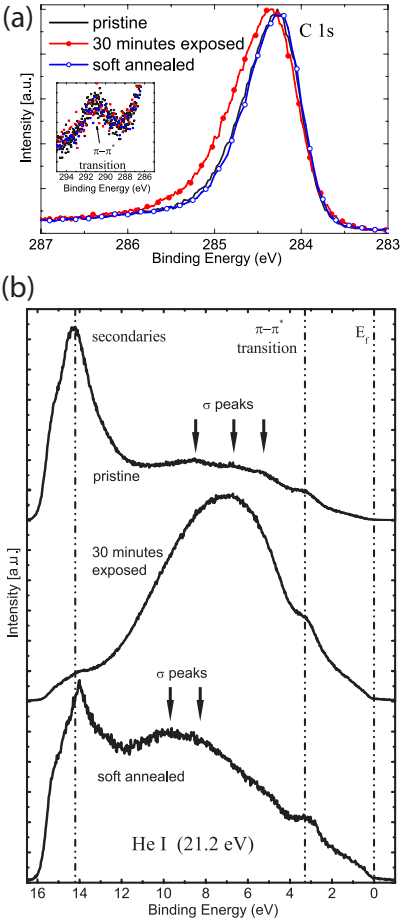

Figure 6.3: XPS (a) and UPS (b) spectra of the HOPG before exposure, after 30 minutes of exposure and after an annealing at 450° C were used to monitor the transformation from graphene to hydrogenated graphene. In (b), the positions of the σ peaks and the eyeguides for the E_f, the secondary electrons and the π-π^* transition are provided.

middle panel), an energetically favorable hydrogenated network of carbon atoms was suggested even at that time. The π-π^* peak at 3.2 eV still exists denoting that the structure is layered. The remnant of the secondary peak indicates that the structure still consists of carbon rings. Since the UPS spectrum of graphite is highly dependent on the polar angle (i.e. the angle between the entrance slit of the analyzer and surface normal) [171], intensity contributions from different polar angles are smeared out and appear as one broad peak 7 eV below E_f as a result of surface roughening after plasma exposure. After soft annealing (Fig. 6.3b bottom panel), the secondary peak raises due to the flattening of the layers. The broadening effect is alleviated and the σ peaks reappear at shifted positions at 8.3 and 10.2 eV below E_f. As suggested by the theoretical calculation of hydrogenated graphite from Allouche *et al.* [170], full hydrogenation of graphite results in a σ band structure very similar to diamond, an sp^3 hybridized carbon allotrope [169, 172]. From this point of view, we can claim that this UPS spectrum is the valence band spectrum of hydrogenated HOPG, analogous to cubic diamond. In the next section, it is shown that the surface still has slight corrugation, which could also have a small contribution to the

UPS spectrum as the remnant of the broad peak at 7 eV. After soft annealing, the D and D' peaks in the Raman spectrum of the HOPG are diminished (Fig. 6.1d 3^{rd} panel), where this partial suppression is due to flattening; however the contribution from the atomic rearrangement of the C atoms, which is possibly due the C-H bonding, is still present. The shift of the σ peak positions towards sp^3 hybridization approves this assumption.

6.3.4 Scanning tunneling microscopy

In order to corroborate the discussions in spectroscopy techniques further, scanning tunneling microscopy (STM) technique was utilized. STM image of a pristine HOPG consists of a hexagonal pattern generated by the charge density of the electrons [173]. After exposure to hydrogen plasma, the surface still consists of a hexagonal pattern but on a highly corrugated plane (Fig. 6.4a). Soft annealing leads to a flatter surface, however it still has a corrugation in the form of ripples and valleys at certain points (Fig. 6.4b). This surface corrugation matches well with the theoretical calculation of a suspended graphane layer, where it is estimated that this

layer has to be corrugated in the form of ripples with an amplitude of a few hundred picometers [164]. The hexagonal ring patterns in Fig. 6.5 appear in different distorted forms. Our STM images are similar to those obtained locally around the step edges of graphite, where the step edges were terminated with atomic hydrogen [57]. Since STM probes the local density of states [173], this distortion in the ring patterns might arise from surface corrugation [57]. On the other hand, it should not be disregarded that graphane has different possible stable C-H conformations and these conformers do have distorted ring structures [132, 144], which might also explain the variety of different distorted STM contrasts observed even on relatively flat surfaces. Moreover, it can be seen that same atomic patterns can be observed on both light and dark contrast sites.

The STM results confirm that we have obtained a new network of carbon atoms on a rippled plane, different from surface [159] and local step edge hydrogenations [57]. However, it has to mentioned that before the introduction of hypothetical graphane in 2007, a very similar hydrogen LTP exposure to ours was performed by Ruffieux *et al* [174]. With the STM method, they recorded very similar current patterns. They

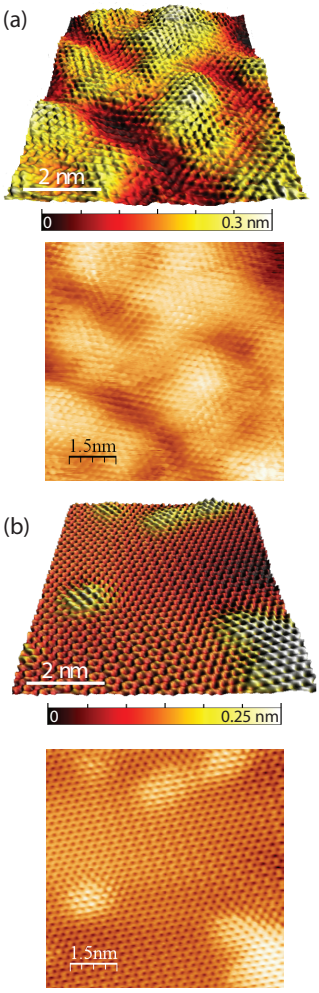

Figure 6.4: STM images of the HOPG after 5 minutes of hydrogen plasma exposure at 450° C (a) and after an annealing at 350 – 400° C for 60 minutes (b), clearly show the flattening of the surface as a result of soft annealing (V_{tip} = 50 mV and I = 70 pA).

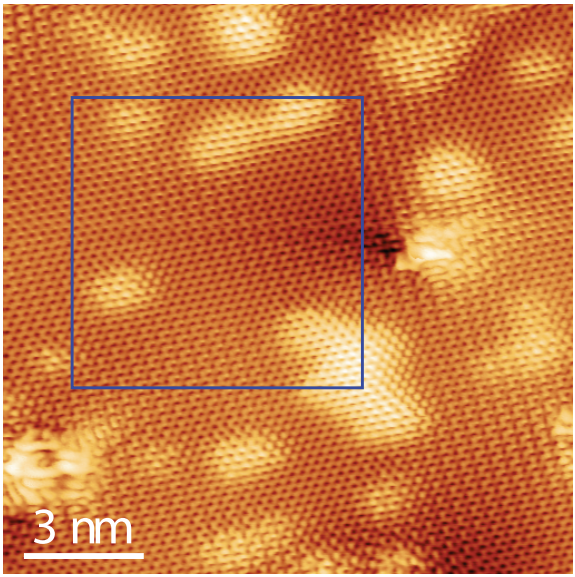

Figure 6.5: Top view STM image of the surface consisting of various atomic-scale patterns where a very low defect density can be observed. The inset is also shown in Fig. 6.4b.

have attributed these patterns solely to defects induced by the hydrogen plasma. With respect to this point, STM method by itself is not conclusive enough to substantiate hydrogenation of HOPG.

6.4 Conclusions and Outlook

1- Hydrogen LTP exposed HOPG and graphene are characterized with various techniques including photoelectron spectroscopy, Raman spectroscopy and scanning probe microscopy. Hydrogen LTP exposed HOPG surface consists of various atomic scale STM patterns, which may be due to different possible C-H conformations of hydrogenated graphene layers. On the other hand, surface corrugation or point defects caused after LTP exposure also have a contribution to these patterns. Regarding its valence band structure measured with UPS, hydrogen LTP exposed HOPG has similar features to cubic diamond. Raman spectroscopy of hydrogen LTP treated single layer graphene reveals a D peak to G peak ratio over 4, which is due to hydrogenation. Graphane is a reserved word for graphene which is hydrogenated from both sides. Though such case

cannot be perfectly realized due to the hydrogen deficiencies and point defect created during the plasma treatment, our results, when considered all together, point to double side hydrogenation of the graphene layers.

2- Graphite might be an alternative solution for hydrogen storage. Since hydrogen LTP exposed HOPG possesses a high thermal stability, unloading of chemically stored hydrogen requires annealing over 1000° C which may not be very feasible. However, hydrogen gas which had caused blisters on the surface might still be stuck between the graphane layers, where the required unloading temperature is around 450° C.

6.5 Experimental

6.5.1 Plasma creation and exposure

The experiments were conducted in the plasma exposure facility at the University of Basel [175]. Plasma was created 75 cm away from the sample in a Pyrex tube through a matching network by a 13.56 MHz RF generator at a typical power of 49 W. This RF power was coupled to the tube by an outer electrode acting as a surfatron [176]. The plasma

source was mounted to a metallic UHV chamber, where a metallic carousel with heatable and biasable sample holders is situated at the heart of this chamber. 3 Pa of hydrogen (6.0 pureness) pressure was used, where the background pressure was 5×10^{-6} Pa. Optical emission spectrum of the plasma yields no peaks other than those of hydrogen and self-ionized mass spectroscopy does not reveal any other ions than those of hydrogen (not shown here). The hydrogen plasma was characterized with a commercial Hiden ESPion Langmuir probe. The probe measurements were performed 5 cm away from the sample where an average T_e of 3.5 $\pm$ 0.5 eV and an ion flux of $1.5 \pm 0.5 \times 10^{15}$ $cm^{-2}s^{-1}$ were obtained. The exact plasma chemistry of the hydrogen ions (H^+, $H_2{}^+$, $H_3{}^+$) was not known, therefore an estimate of 2 a.m.u. was used as the average ion mass, which introduces $\sim 10\%$ uncertainty to T_e calculation. ϵ_i was calculated as a sum of energy gained traversing plasma sheath (from balancing ion and electron fluxes at the sample surface) and the initial ion energy: $\epsilon_i = (T_e/2)ln(M/2\pi m) + 0.5(T_e)$ which corresponds to 3.34 T_e for H^+ and 3.88 T_e for H_3^+ ions. For simplicity, ϵ_i was taken as 3.6 T_e which is 12.6 $\pm$ 1.8 eV in our case. We think that, double side hydrogenation might be achieved un-

der these plasma conditions. It is also possible to achieve single surface hydrogenation, anisotropic chemical etching [23] or physical sputtering of HOPG by changing the plasma parameters or sample conditions.

Implantation is a homogeneous process taking place all over the HOPG subsurface layers. With a pessimistic approach, one can assume that only 10% of the impinging ions are atomic, where half of them gets backscattered, physisorbed or chemisorbed on the surface, leaving only 0.75×10^{13} $cm^{-2}s^{-1}$ of them getting implanted as atomic hydrogen. Also taking the H-H combinations in the HOPG into account, the necessary ion fluence would reach several minutes to hydrogenate the subsurface layers of the HOPG, where the surface density is 3.8×10^{15} cm^{-2} and hydrogen uptake is 1:1 for the graphane formation.

During hydrogen plasma exposure, samples were electrically floating while they were being heated resistively. HOPG samples were cleaved in air before they were introduced to UHV environment. Temperature calibration was done in a separate exposure using a chromel alumel thermocouple mounted on the sample as well as it was being controlled with a pyrometer during actual exposures.

6.5.2 Characterization methods

Raman spectroscopy measurements were performed using a WITec alpha 300 confocal Raman microscope. The wavelength of the excitation laser was 532 nm and the power of the laser was kept at 2.1 mW without noticeable sample heating or damaging. The laser spot size was approximately 360 nm at 100 $\times$ magnification. The spectral resolution was 3 cm^{-1} and each spectrum was an average of 20 accumulations with an integration time of 0.5 seconds per accumulation. Graphene flakes for Raman spectroscopy measurements were prepared by exfoliation of HOPG using a PDMS stamp and transferring them on SiO_2 [177]. The number of layers was determined from the 2D peak of the Raman spectra which was acquired prior to plasma treatment.

An intermittent contact mode AFM experiment was performed by means of a Nanosurf FlexAFM operated in ambient conditions. The quantities that have been measured are the cantilever oscillation amplitude (A_{free}=20 nm) and phase related to the driving signal. The distance to the sample was controlled in a feedback loop, maintaining the cantilever oscillation amplitude equal to a given setpoint value

(typically 0.5-0.65 · A_{free}). The topography image was acquired by changing the xy position of the cantilever tip over the scanned surface. The full range of the scanner was equal to 10 μm × 10 μm. A commercially available Nanosensors PPP-NCLPt silicon cantilever was used. The fundamental frequency, spring constant and quality factor of the cantilever were equal to f_0 = 142 kHz, k = 20 N/m, Q = 300 respectively. We have avoided performing electron microscopy on the HOPG samples because the electron beam energy might ionize H_2O and NH_3 adsorbents and cause additional effects [178].

XPS measurements were performed in UHV conditions with a VG ESCALAB 210 spectrometer using monochromatized Al Kα radiation (1486.6 eV) with an energy resolution better than 0.5 eV. A helium discharge lamp emitting in ultraviolet range (He I, 21.2 eV) was used for UPS measurements. The samples were transferred to photoemission chamber without breaking the high vacuum conditions. The base pressure in the chamber was around 1 × 10^{-7} Pa during acquisition. Normal electron escape angle (i.e polar angle = 0 °) and a step size of 0.025 eV were used. The Au $4f_{7/2}$ line was measured at a binding energy of 83.78 eV, hence all our XPS peaks are

shifted -0.22 eV. Wide scan XPS spectra from 0 to 1200 eV showed only carbon, which precludes a possible interpretation of the results as a reaction with an unknown element.

STM was performed with a commercial qPlus STM/AFM microscope (Omicron Nanotechnology GmbH) at 77 K under UHV conditions and operated by a Nanonis Control Systems from SPECS GmbH. All STM images were recorded at constant current mode with the bias voltage applied to the tip. The samples were heated to 80-400 °C prior to measurements in UHV.

6.5.3 Acknowledgements

The authors would like to thank the Swiss Federal Office of Energy and the Federal Office for Education and Science for their financial support. This work was also supported by the Swiss National Foundation (SNF), the National Centre of Competence in Research on Nanoscale Science (NCCR Nano) and National Centre of Competence in Research on Quantum Science and Technology (NCCR QSIT).

6.6 Comment

It is important to differentiate between the word graphane, meaning fully, double sided hydrogenated graphene, and hydrogenated graphene, only describing partially (not further specified) graphene.

The work presented in section 6.3.1 is compared to the experiments made by Elias and co-workers [28]. We do agree with Elias and co-workers that in their work, fully hydrogenated graphene was only found for free standing graphene. Due to the presence of the substrate, the hydrogen atoms reach only the top side of the graphene sheet easily. To hydrogenate the lower side, the atoms need to penetrate the graphene for which low energy ions are needed as mentioned in the main text and section 2.4.1 [147]. In contrary to [28], a double sided hydrogenation of the samples can occur in the system employed here, due the hydrogen ion energy being large enough to break C-C bonds.

Interestingly, the surface corrugation visible in the AFM images shown in Fig 6.2 were only visible in the system discussed in this chapter, in contrary to the systems of chapter 3,4,5.

Similar structures were not seen in graphite exposures performed in the plasma enhanced CVD system mentioned in chapter 4. The plasma chamber employed here (chapter 6) is metallic, whereas for the CVD system a quartz tube was used. It is known that the recombination rate at metallic surfaces are higher than on quartz glass [77]. This could lead to a lower density of hydrogen atoms in the vicinity of the graphite surface. Further, the ionic species in the plasma used in this chapter have higher energies, due to the lower pressure. The ion energies evaluated with Langmuir probe measurements indicate 12.6 eV in this work whereas in chapter 4, the ion energies most probably are lower. Therefore, the hydrogen implantation and hydrogenation of the graphite surface discussed here, probably occurs via the first step of the chemical erosion process: the ions in the system hit the surface of the graphite and break C-C bonds, allowing the ions to diffuse underneath the top graphite layer and lead to an accumulation of recombined hydrogen molecules underneath the graphite surface. Due to the low hydrogen atom concentration, most of the C-C carbon bonds close immediately after breaking, reforming the hexagonal carbon structure. As mentioned in the main text, the reason for the occurrence of the disorder peaks

in the Raman measurements of the graphite samples is not clear. It could be due to the partial hydrogenation or to the corrugation of the graphite surface. In the plasma enhanced CVD system of chapter 4, on the other hand, graphite samples in the vicinity of the plasma showed large hexagonal holes of a few layers in depth. Due to the lower ion energies, the graphite erosion takes probably place via ion assisted chemical sputtering (see subsection 2.4.2), binding the ion to the surface graphite. If chemical erosion also occurs, the probably slightly higher hydrogen atom concentration leads to an immediate saturation of the broken C-C bonds [91–93]. Both processes lead to the erosion of the graphitic surface, allowing any accumulated hydrogen to escape from underneath the top graphite layer.

Chapter 7

Evidence for Disorder Induced Delocalization in Graphite

Lucas Casparis, Andreas Fuhrer, Dorothée Hug,

Dominikus Kölbl, Dominik M. Zumbühl

The content of this chapter is submitted to : L. Casparis, A. Fuhrer, D. Hug, D. Kölbl, D. M. Zumbühl , *Evidence for Disorder Induced Delocalization in Graphite*, arXiv:1301.2727v1 (2013)

7.1 Abstract

We present electrical transport measurements in natural graphite and highly ordered pyrolytic graphite (HOPG), comparing macroscopic samples with exfoliated, nanofabricated specimen of nanometer thickness. Nano-samples exhibit a very large c-axis resistivity ρ_c – much larger than expected from simple band theory – and non-monotonic temperature dependence, similar to macroscopic HOPG, but in stark contrast to macroscopic natural graphite. A recent model of disorder induced delocalization is consistent with the data. Micro-Raman spectroscopy reveals clearly reduced disorder in exfoliated samples and HOPG, as expected within the model – therefore presenting further evidence for a novel paradigm of electronic transport in graphite.

7.2 Introduction

Graphite is a paradigmatic layered material and has been investigated intensively for many decades. The in-plane resistivity ρ_{ab} is rather well described by a simple Drude model. However, the resistivity ρ_c along the c-axis, perpendicular

to the graphite basal planes, as well as its temperature dependence $\rho_c(T)$, are not described by the simple band structure model [179, 180], and currently lack theoretical understanding despite extended efforts. The resistive anisotropy $R_A = \rho_c/\rho_{ab}$ is a convenient dimensionless parameter characterizing transport properties.

Carbon atoms in the graphite basal planes are strongly bound by covalent bonds, while much weaker Van der Waals forces bind the graphene sheets along the c-axis. Non-trivial disorder such as stacking faults and crystalline grains result in a mosaic angle and complicate electronic transport. Simple band theory [179] predicts $R_A = m_c/m_{ab} \sim 140$, the ratio of the corresponding band masses, which holds in presence of isotropic disorder. This agrees well with measurements in natural graphite (NG) [30, 31]. In highly oriented pyrolytic graphite (HOPG), the anisotropy was found to be much larger, even exceeding 10'000 in some experiments [32, 33]. Moreover, band theory [179] predicts a monotonic metallic temperature dependence for both ρ_{ab} and ρ_c, resulting in a temperature independent anisotropy R_A. This is seen in NG [34], but not in HOPG, where ρ_c is non-monotonic with a maximum around 40 K [32, 33, 181], similar to ρ_c in

other layered materials, such as $NaCo_2O_4$ [182] and Cuprates [183]. A large anisotropy far exceeding 100 combined with the non-metallic temperature dependence – together referred to as anomalous behavior – are currently not understood and present a fundamental problem in condensed matter physics [34–36].

7.3 Fabrication and methods

In this Letter, we use exfoliation and nano-fabrication techniques to investigate electrical transport in graphite flakes (see Fig. 7.1), comparing samples with thicknesses in the nanometer range with macroscopic samples and further comparing HOPG with Indian and Madagascar NG. Surprisingly, while conforming to the band-structure results in macroscopic NG flakes, NG displays anomalous behavior in nanostep samples – namely a large resistive anisotropy as well as a non-metallic temperature dependence. HOPG, on the other hand, shows no size dependence, behaving anomalously in all samples. We note that there are no previous ρ_c data for nanometer thickness specimen, to the best of our knowledge. Interestingly, the in-plane resistivity

of all samples is in good agreement with reported values [30–32], and shows no size-dependence, making it clear that the large anisotropies in the anomalous samples are to be attributed to a large ρ_c. These measured anisotropies appear consistent with a recent model based on disorder induced delocalization by *Maslov et al.* [37, 184], further corroborated by a disorder characterization of our samples using micro-Raman spectroscopy. Conduction path mixing due to a finite mosaic angle can account for the non-monotonic temperature dependence [185], altogether presenting first experimental evidence for a novel paradigm of electrical transport in graphite.

To produce nanostep samples, we use the design shown in Fig. 7.1(a). We exfoliate graphite onto a SiO_2/Si wafer and identify suitable flakes with two plateaus differing in height using an optical microscope. The lower plateau height d and the step height h are determined from an AFM image and cross-sections, see Fig. 7.1(b,d), giving heights between 14 and 150 nm. To extend the range to larger step heights, we use e-beam lithography and oxygen-plasma etching to carve steps up to $h = 450$ nm.

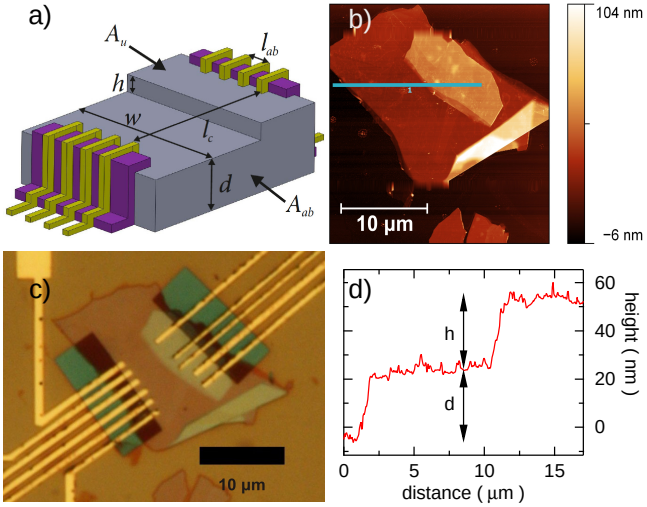

Figure 7.1: Nano-graphite samples. (a) Device schematic. Ti/Au contacts (yellow) for 4-wire measurements are patterned on each plateau, isolated from the graphite walls by a SiO_2 layer (purple). AFM picture (b) and optical microscope image (c) of an HOPG flake with two plateaus. (d) Cross section along the blue line in (b), giving plateau heights.

For contacting the plateaus, we first cover parts of the exterior edges of both plateaus with SiO_2 of at least 80 nm thickness [186] in order to prevent short-circuiting the c-axis. Contacts (typically a few hundred nanometers in width) and bonding pads are patterned in a final e-beam step, evaporating a Ti/Au layer thicker than 110 nm (SiO_2 thickness plus 30 nm). A typical device is shown in Fig. 7.1(c). All resistances are

measured with a standard 4-wire lock-in technique. This layout allows measurements of both ρ_{ab} and ρ_c on the same device, as needed to obtain the anisotropy, but requires resistivity corrections due to geometry inherent conduction path mixing.

7.4 Size dependent resistivity measurements

The in-plane resistivity $\rho_{ab} = R_{ab}A_{ab}/l_{ab}$ is estimated from the 4-wire resistance R_{ab} with current and voltage probes on the same plateau and assuming a simple rectangular shape of the graphite sample, with voltage probe distance l_{ab} and total graphite cross section A_{ab} (see Fig. 7.1(a)). This is a good approximation for thin samples, if the anisotropy is smaller than $l_{ab}/d \sim 250$. For large anisotropy – as seen in most samples – the extracted ρ_{ab} presents an upper bound due to an effectively thinner conduction layer, since the current cannot penetrate easily along the highly resistive c-axis. The ρ_{ab} extracted here (see Table 7.1, and Fig. 7.2) agree rather well with literature [30–32, 187], typically giving $\rho_{ab} \sim 1\,\mu\Omega\,m$.

Moreover, ρ_{ab} appears independent of the graphite thickness and is similar for NG and HOPG samples, as seen in Fig. 7.2, open symbols.

Next, we determine the c-axis resistivity ρ_c. Since l_c, the contact to contact distance across the step, is much larger than the step height h (see Fig. 7.1(a)), we need to subtract the in-plane contributions to the measured resistance R_c to obtain the corrected resistance R_{corr} using

$$R_{corr} = R_c - \rho_{ab} \cdot \left(\frac{l_{cl}}{w_l \cdot d} + \frac{l_{cu}}{w_u \cdot (d+h)} \right), \qquad (7.1)$$

with upper/lower contact to step distance $l_{cl/cu}$ and corresponding plateau widths $w_{l/u}$. ρ_c is then obtained from $\rho_c = R_{corr} A_u / h$, where A_u is the upper plateau area. We note that as previously for ρ_{ab}, we again overestimate the thickness d for large anisotropy. However, here, this effectively cancels the overestimated ρ_{ab}, making the extracted ρ_c quite robust. The correction is often substantial, reducing ρ_c and the anisotropy by a large factor (see Table 7.1).

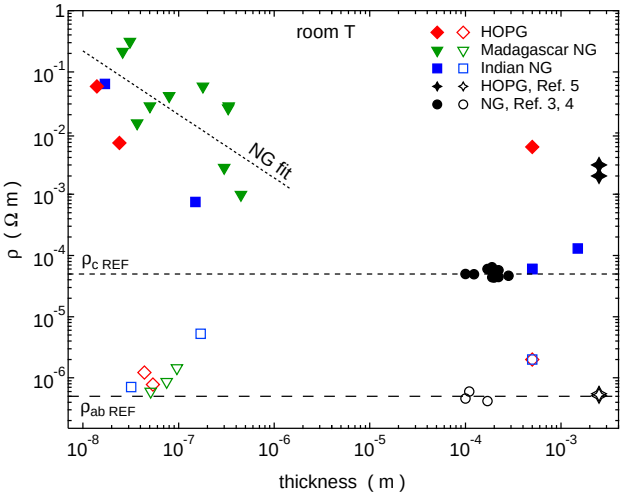

Figure 7.2: Influence of graphite thickness on ρ_c (solid markers) and ρ_{ab} (empty markers) at room temperature, comparing HOPG (red) with Madagascar NG (green) and Indian NG (blue). For ρ_{ab}, the abscissa value used is $d+h$, the overall flake thickness, see Table 7.1. Previous measurements of macroscopic samples (black) were added for both HOPG [32] (stars) and NG [30, 31] (circles) for comparison. Dashed horizontal lines indicate literature values $\rho_{ab\,\mathrm{REF}}$ for ρ_{ab} and $\rho_{c\,\mathrm{REF}}$ for ρ_c. Further, the best power-law fit to all NG nanostep data (dotted line, linear fit on log data, slope of -1.0 ± 0.4) is added to indicate a potential trend, see text.

The resulting ρ_c are displayed in Fig. 7.2 as a function of height (filled symbols), giving very large ρ_c and correspondingly large anisotropy R_A for all nano-graphites, both NG

and HOPG. Interestingly, a power-law fit (linear fit on the log-log graph, slope -1 ± 0.4) through all NG nanostep ρ_c data points seems to indicate a trend reducing ρ_c with increasing step height towards the macroscopic ρ_c value in NG samples. HOPG nanostep data is excluded from the fit, since HOPG has no apparent size dependence when going from macroscopic to nanostep samples (filled red diamonds). However, the wide spread of the data and the resulting error bars on the fit-slope are significant; to make a more definite statement, samples with step heights between $1\,\mu$m and $100\,\mu$m might give more insight [188].

Table 7.1: Nano-sample parameters, see text for definitions, and Fig. 7.1 for an illustration. Samples listed here are represented in Figs. 7.2 and 7.3. Fig. 7.2 includes data from additional exfoliated Madagascar (Mad.) samples.

Material	ρ_{ab} [$\mu\Omega m$]	R_c [Ω]	l_{cl} [μm]	w_l [μm]	l_{cu} [μm]	w_u [μm]	d [nm]	h [nm]	R_{corr} [Ω]	A_u [μm^2]	ρ_c [mΩm]	R_A
HOPG 1	1.22	11.5	4	25	2.5	25	30	14	2.3	361	58.0	47700
HOPG 2	0.78	12.1	6	20	2	20	30	24	2.9	57	6.88	8840
Mad. 1	1.45	27.4	1.2	10	2.3	10	16	80	13.1	248	40.5	27900
Mad. 2	0.60	26.0	4.2	8	3.3	5	14	37	5.6	95	14.5	24000
India 1	0.71	18.9	1	20	3	20	15	17	10.7	100	63.2	89300
India 2	5.27	37.0	2.4	20	2	15	20	150	1.27	88	0.78	142

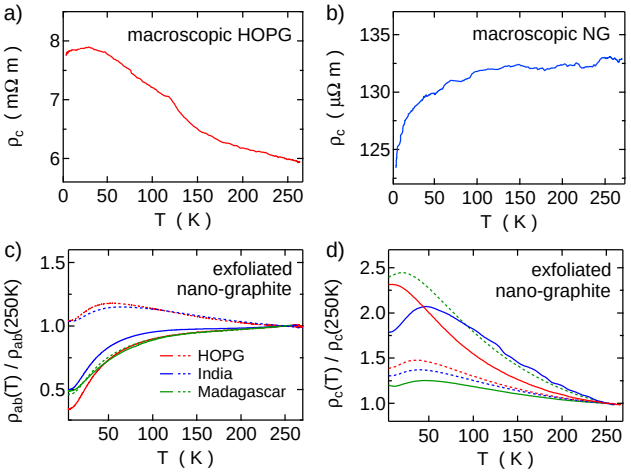

Figure 7.3: Temperature dependence of resistivities. $\rho_c(T)$ in macroscopic HOPG (a) and macroscopic Indian (b) NG. (c) $\rho_{ab}(T)$ in nanoscale samples for HOPG (red) and NG India (blue) and Madagascar (green). Two samples are presented for each graphite type, corresponding to Table 7.1 (solid, sample 1; dashed, sample 2) (d) $\rho_c(T)$ for the same samples.

To allow a comparison with previous experiments, we also investigate macroscopic NG and HOPG samples, again measuring both ρ_{ab} and ρ_c. Due to the geometry used, corrections are small and not necessary for the macroscopic samples. The values obtained are also added to Fig. 7.2, together with typical values from literature [30–32]. We find decent agreement between our macroscopic data and previous measurements,

reproducing here again the large discrepancy in ρ_c between HOPG and NG in macroscopic samples.

7.5 Temperature dependent resistivity measurements

Next, we turn to the temperature dependence $\rho_c(T)$ of the macroscopic samples [189]. For HOPG, we find a non-metallic ρ_c at high T ($d\rho_c/dT < 0$), see Fig. 7.3 (a). Around 40 K, ρ_c displays a rather shallow maximum, in good agreement with previous HOPG measurements [32]. In contrast, macroscopic Indian NG behaves weakly metallic and monotonic down to 4 K (shown in Fig. 7.3 (b)), also in agreement with previous NG data [30]. Overall, our data from macroscopic samples fully agrees with the literature, giving us confidence that a comparison of the exfoliated samples with literature is appropriate.

The temperature dependence of the exfoliated nano-graphite samples are shown in Fig. 7.3 (c) and (d), normalized to the high-T value. In most samples, $\rho_{ab}(T)$ is metallic and monotonous, as expected, and in agreement with

macroscopic data [30, 190]. In two specimens, ρ_{ab} is weakly non-monotonic. This seems to occur occasionally in nanoscale samples, as previously reported [191, 192]. Interestingly, $\rho_c(T)$ of all nanostep samples is qualitatively the same, showing a non-metallic and non-monotonic temperature dependence, qualitatively identical to macroscopic HOPG, and clearly different from the macroscopic NG data. We emphasize that the non-metallic $\rho_c(T)$ combined with the large anisotropy R_A constitutes anomalous behavior for all nanoscale samples. In contrast, only macroscopic HOPG is anomalous, not macroscopic NG.

Motivated by an anisotropy far exceeding the band structure expectation, we consider a recent theory by Maslov et al. [37]. A similar effect was also previously observed for photons [184]. Within this theory, c-axis transport is strongly suppressed in samples with weak bulk disorder due to 1D Anderson localization along the c-axis induced by randomly spaced barriers (e.g. stacking faults). This gives a very large ρ_c and anisotropy R_A, as observed in the anomalous samples. In samples with sufficiently strong bulk disorder, however, c-axis localization is destroyed by bulk scattering out of the c-axis direction, leading to reduced ρ_c and smaller R_A,

as seen in the macroscopic NG samples. Interestingly, here, disorder can *suppress* Anderson localization, rather than enhancing it, as is usually the case. Therefore, HOPG and nanostep samples are expected to have weak bulk disorder, whereas macroscopic NG specimen either have significantly more bulk disorder (suppressing c-axis localization), or fewer c-axis barriers, insufficient for localization (barriers spacing exceeding coherence length).

7.6 Discussion

To characterize disorder, we have measured spatially resolved micro-Raman spectra, see Fig. 7.4. We plot $\xi = I_D/I_G$, the ratio of the G-peak intensity I_G and D-peak intensity I_D after background subtraction, obtaining an intensity independent characterization of disorder. For graphite, $0 \leq \xi \lesssim 1$. A large ξ indicates a high degree of disorder (large I_D). Due to a finite integration time, ξ has measurement noise of $\sim 1/50$, i.e. $\xi \lesssim 1/50$ indicates an invisible D-peak and weak disorder. We note that for macroscopic samples, the Raman measurements probe only a thin surface layer. For the nanostep samples, on the other hand, a significant depth is characterized [193],

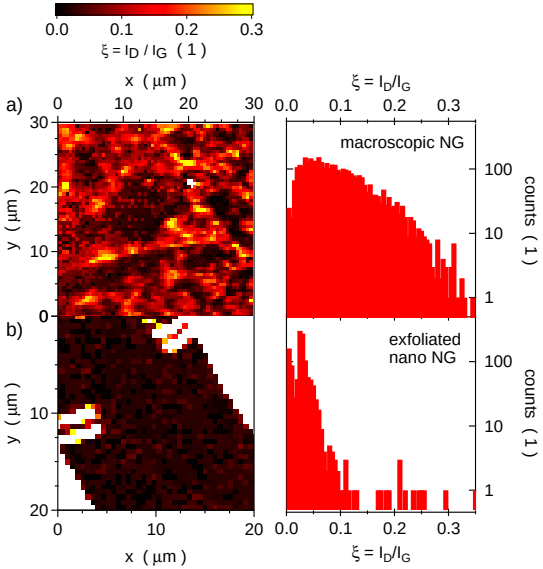

Figure 7.4: Disorder characterization with micro-Raman spectroscopy. Ratio $\xi = I_D/I_G$ of the D-peak and the G-peak intensities, scanned (resolution $\sim 0.5\,\mu$m) on (a) macroscopic Madagascar NG and (b) exfoliated Madagascar flake, plotted on the same color-scale, as indicated. White is off the graphite flake. Corresponding histograms of ξ gathered over the shown scan areas are shown to the right of each scan.

presenting a good measurement of graphitic bulk disorder.

In macroscopic and nanostep HOPG, disorder is very low ($\xi \lesssim 1/50$ essentially everywhere, not shown), while macroscopic Madagascar NG samples are clearly more dirty, consistent with expectations from the model. Micron sized regions of strong disorder mix with cleaner areas in pristine

NG, see Fig. 7.4(a) for a typical scan. A histogram is adjacent to the scan, revealing a broad distribution extending up to $\xi \sim 1/3$. In contrast, an exfoliated Madagascar flake displays significantly reduced disorder, see Fig. 7.4(b). Several exfoliated NG samples were inspected, all exhibiting ξ significantly smaller than in macroscopic NG samples.

We note that exfoliating macroscopic NG only once already results in strongly reduced disorder. Clearly, exfoliating somehow acts expose clean surfaces [194] and to remove bulk disorder, though the mechanism is not clear. This could potentially explain the size dependence mentioned in Fig. 7.2: thinner samples tend to require more exfoliation steps, therefore becoming cleaner, more localized, and obtaining a larger ρ_c. Ultimately, for sufficiently small h, 1D localization should break down and ρ_c decrease strongly – not visible in the present data, presumably because h is still too large. Overall, the Raman data is in good agreement with the predictions of the model, namely weak disorder in all exfoliated and all HOPG samples, as opposed to strong disorder in NG macroscopic samples.

Finally, we turn to the anomalous temperature dependence of ρ_c. If the c-axis resistivity ρ_c is very large, the c-axis conduc-

tance path could easily be mixed with the ab-conductivity σ_{ab} due to the finite mosaic angle θ, effectively short circuiting the intrinsic c-axis conductivity σ_c. Assuming small tilting $\theta \ll 1$, the measured conductivity $\widetilde{\sigma_c}$ can be written as [185]

$$\widetilde{\sigma_c}(T) = \sigma_c(T) + \left\langle \theta^2 \right\rangle \cdot \sigma_{ab}(T), \tag{7.2}$$

where $\langle \theta^2 \rangle$ is the variance of θ. In low bulk-disorder samples at low temperatures, the intrinsic σ_c is very small (strongly localized) and $\widetilde{\sigma_c}(T)$ obtains a significant component from σ_{ab}, including the (weakly) metallic temperature dependence $\sigma_{ab}(T)$, leading to a slight increase of $\rho_c(T)$ upon increasing T. At higher T, localization is weakened (due to phonon scattering, equivalent to increasing bulk disorder for increasing T), σ_c is enhanced and becomes increasingly more dominant, leading to a decreasing ρ_c above some cross-over T. For a mosaic angle of about 0.8° (values between 0.2° and 2° were measured, not shown), the crossover would occur around 40 K, in agreement with the data. For disordered samples, on the other hand, the intrinsic σ_c is dominating $\widetilde{\sigma_c}(T)$ since localization is already lifted by disorder, resulting in the usual metallic temperature dependence, as seen in macroscopic NG [34].

7.7 Conclusion

In conclusion, we observe anomalous behavior, namely high ρ_c and non-monotonic $\rho_c(T)$, in both NG and HOPG exfoliated samples. This is in stark contrast to macroscopic samples, where the anomalous behavior is only seen in HOPG, consistent with previous experiments. A recently proposed transport theory [37] can consistently explain this convergence on the nanoscale, the macroscopic data, and the temperature dependence. Further, finding indeed low disorder in exfoliated and HOPG samples, and high disorder in macroscopic NG, as expected within the model. We note additionally that neutron irradiation experiments [32, 35] inducing bulk disorder also give consistent results, namely reduced ρ_c after irradiation of HOPG, further corroborating the model. We therefore present first, clear evidence of disorder induced delocalization as a new paradigm of electronic transport in graphite.

Though beyond the scope of the present work, it would be very interesting to subject the model to further scrutiny: studying intermediate steps filling the thickness gap in Fig. 7.2, but also even smaller thicknesses, ultimately down

to few- or bi-layer graphene, potentially revealing the localization length. This might be facilitated by bottom contacts with layers deposited on top, followed by top contacts. We note that the minimum thickness in the present samples is 14 nm, corresponding to about 50 graphene layers. Further, a characterization of graphite disorder would be of great interest, e.g. investigating stacking faults and angles, intercalation, grain and boundary formation, aiming at identifying the localization mechanism, leading ultimately to a microscopic understanding of electrical transport in graphite. The results presented here were obtained in graphite, but it would be intriguing to learn if similar arguments apply to some of the numerous other layered materials.

We are very grateful to D. Maslov for initiating the experiments and numerous invaluable discussions and to S. Tongay for performing XRD and Raman measurements. Further, we thank F. Dettwiler, D. Maradan and P. Jurcevic for experimental help. This work was supported by the Swiss Nanoscience Institute (SNI), Swiss NSF, ERC starting grant and NCCR QSIT.

Chapter 8

Outlook

Graphene Hall bars 550 nm in width with 180 nm wide voltage probes were measured electrically in a magnetic field up to 14 T. The samples show strong charge inhomogeneities and edge disorder in the transport measurements. The main contribution to the disorder is the small size ($20 - 60$ nm) of the voltage and contact probes whereas charge disorder mainly arises due to the underlying silicon substrate and deposited molecules on the surface, inducing randomly charged puddles into the system.

Magnetoransport measurements in graphene Hall bars thinner than 550 nm could be performed using larger voltage probes. Current annealing of the samples could further be

applied to reduce the charged impurities on the sample surface. Also, suspending graphene Hall bars could be performed depositing the graphene flake onto an organic lift-off resist (LOR) [195]. Exposing the resin at the position of the graphene Hall bar and subsequent development of the resin would suspend the ribbons (see [195] for detailed fabrication).

To reduce the influence of the edge roughness on the graphene ribbons, the chemical etching of graphene exposing the samples to the remote region of a pure H plasma was investigated. Anisotropic etching was seen for graphite, BL graphene on SiO_2 and SL and BL graphene samples on hBN flakes. The crystallographic orientation of the hexagonal etch pits indicate a preferred etching direction along one type of edge.

The edge quality of the hexagonal pits in SL and BL graphene flakes could be investigated with low temperature and high vacuum AFM measurements. Due to attenuated edge vibration and clean surfaces the investigation of the edges at an atomic scale could be possible [196].

Scanning tunneling microscopy is also an option worth envisaging, as atomic resolution can be obtained at ambient conditions. As a consequence, the samples need to be deposited

onto a conductive substrate, which could be performed using PDMS stamps, as explained in the appendix [177]. The graphite surfaces are first pre-patterned with e-beam lithography and subsequently etched in the H plasma at the parameters used for SL graphene etching. In a next step, the upper graphite layers are transfer printed with a PDMS stamp onto a flat, conductive substrate, e.g. gold(111), before the edge structure of the hexagonal holes are scanned with the STM.

Another method for the investigation of the edge quality are angle dependent Raman measurements. As mentioned in subsection 2.1.5, Raman traces of pure graphene zigzag edges do not display a *D*-peak, in contrast to pure armchair and disordered edges [68, 70, 71].

The influence of thermal annealing in vacuum and in H gas as well as of the H plasma exposure in a copper contaminated quartz tube was investigated. A similar experiment should be repeated in a clean quartz tube as the samples fabricated in chapter 4, did not show any sign of hydrogenation in Raman measurements. Comparing the conductivity of H plasma etched and RIE fabricated ribbons both deposited on hBN flakes, could allow a statement about the quality difference of the two processes.

In a next step, the H plasma etched graphene nanoribbons could be suspended, allowing further differentiation of substrate and edge induced disorder by comparing the measurement results with lithographically fabricated, suspended ribbons. Exfoliated graphite flakes on a SiO_2 substrate could be pre-patterned with e-beam lithography, similarly to the SL graphene flakes in chapter 4 and etched in the H plasma. The SiO_2 substrate can subsequently be removed with a buffered oxide etch [16].

Changing the gas type from hydrogen to nitrogen for the plasma etching of graphite, alters the orientation of the pits by 90° C, indicating the change of edge type from zigzag to armchair and could be a process for the chemical fabrication of *AC* ribbons [124].

Hydrogenation of SL graphene flakes on silicon dioxide substrates was performed in chapter 6. Theoretical calculations predict that fully hydrogenated graphene, namely graphane, is a large band gap semiconductor with an energy gap of $E_{gap} = 3.4 - 5.4\,\mathrm{eV}$ depending on the calculation methods [132, 197]. Also, hybrid graphene/graphane structures are theoretically expected to allow experimental investigation of intriguing physical effects. The quantum spin valley

Hall (QSVH) effect could be measured in a graphene ribbon, formed in between two graphane stripes [142]. The graphene/graphane interfaces act as barriers for the π charge carriers, due to the large band gap of graphane, effectively forming a graphene ribbon in the non-hydrogenated region. In contrast to lithographically formed ribbons, the edge states emerging at the interface are dispersive, allowing the generation of the QSVH effect [142]. Local hydrogenation of graphene, using a silicon stencil mask, has been achieved recently, enforcing the possibility of the fabrication of mixed graphene/graphane structures [141].

In chapter 7 the increase of the c-axis resistivity of natural graphite samples with decreasing sample size was observed, strongly contrasting the results obtained for HOPG and macroscopic natural graphite samples in previous experiments and confirmed in this work. The origin of the ρ_c augmentation for small sized samples is explained with a variation of the defect density in the sample. As mentioned in the main text (see chapter 7), samples with intermediate sizes are missing and would give a more complete picture of the disorder influence. Further, the large steps in the micrometer sized samples were fabricated using RIE, itself introducing

disorder to the graphite surface. Hence, the graphite flakes could be sandwiched in between top and bottom gates, as mentioned in chapter 7. To increase the yield of graphite flakes deposited onto pre-fabricated bottom contacts, again, the transfer method developed by Dean and co-workers could be employed [19]. Hence also graphite flake of known height can be chosen and investigated.

Appendix

Fabrication

In this section of the appendix I would like to share the experiences I made during fabrication of the samples we investigated. In the first part, the preparation of the silicon/silicon dioxide wafer substrate is explained, followed by the exfoliation techniques used to cleave graphite into graphene flakes. Further, the recipes for the different electron beam lithography steps used to pattern the graphene Hall bars and circular holes needed for the hydrogen plasma etchings are explained.

Graphene sample preparation

Preparing graphene samples is, at first sight, quickly learned and easily implemented. Cleaving graphene using a scotch tape and transferring it onto a substrate is not the difficult part. However, fabricating large flakes, samples with clean surfaces, low ohmic contacts and sophisticated suspended graphene devices is not straight forward. A lot of experience and well established recipes lower amount of frustrating moments, having to "start all over again". Here, I would like to give an overview of all the working recipes we used and established during the processing of our samples. I hope it will make fabrication life of succeeding PhD candidates easier and allows them to spend more time on measurements than I could.

Substrate preparation

To fabricate our graphene samples we used highly doped silicon wafers [198] with a 295 nm SiO_2 insulating layer on top. The height specified by the company checked with elipsometry measurements and amounted to 285 nm. It is essential

that the silicon layer of the wafers is highly doped, as we used it as a back gate, changing the charge carrier density of the graphene samples during measurement. Further, the thickness of the insulating SiO_2 capping changes the visibility of the deposited graphene flakes [62, 63]. Depending on the oxide thickness, the flakes are invisible in the microscope, making the isolation of the SL graphene flakes extremely difficult.

As the fabrication of our devices include several electron beam lithography (EBL) steps, a precise localization of our flakes is important. Therefore, a localization grid [199] is deposited at first onto the Si/SiO_2 wafer using optical lithography and standard metal evaporation techniques. In table 8.1 every step for the grid fabrication is listed separately. There are a few delicate steps in the grid fabrication I would like to mention here.

Optical lithography parameters such as exposure and development times do change over time and can depended on the age of the resist. Therefore it is always advisable to perform test runs with junk wafer pieces before starting processing a whole wafer. To approach the correct parameters for the resist, one can start with the parameters used for the last grid

fabrication and adapt them as needed. Therefore, one should take the parameters listed in table 8.1 as approximate values only.

The UV resist we use here is very sensitive and exposure, as well as subsequent development usually takes solely $1 - 2\,\mathrm{s}$, meaning that there is not much time for the various steps. The best way for the development of whole wafers is to use flat glass petri dishes and wafer tweezers. When immersing the wafer into the development solution, one has to be careful to submerge the whole wafer quickly in the developer, as otherwise parts of the wafer will be over developed whereas other parts will not be developed enough.

Substrate cleaning and UV grid fabrication recipe			
Step	Process	Details	Parameters
1	3 solvent cleaning process		
		TCE	10 min ultrasound (100%)
		Acetone	10 min ultrasound (100%)
		IPA	10 min ultrasound (100%)
			rinse with IPA, blow dry
2	UV resist spinning	Prebake	Hot plate, 100° C, 5 min
		Spinning	4000 rpm, 40 s, 4 s ramp
		Bake	Hot plate, 120° C, 7 min
3	Expose to UV light	Wavelength	Chanel 1 (352 nm)
		Hard contact	3 s
		Exposure time	1 s
4	Development	Developer	
		Development time	2 s
		Stop development	H_2O, 30 s, blow dry
5	Metal deposition	Base pressure	$< 5 \cdot 10^{-6}$ mbar, Sharon
		Titanium	5 nm
		Gold	45 nm
		lift off	warm (50° C) acetone, 1 h
			rinse with IPA, blow dry

Table 8.1: Preparation of the Si/SiO_2 wafer for graphene deposition. Using optical exposure processes a grid pattern with number is fabricated on the surface of a whole or small pieces of a Si/SiO_2 wafer. The Grid is needed for the localization of the graphene flakes after their deposition.

After development of the UV structures, metal is evaporated onto the sample surface, as explained below. To clean the surface thoroughly from the resin residues, the wafer pieces should be exposed to UV light again, in the floud exposure mode for 1 h. During the floud exposure of the wafer, the resin residues is deteriorated and can be washed off in the developer immediately afterwards. To ensure the total removal of the resin residues, the wafers were left in the developer for 2 h before they where rinsed with water and blown dry. Much better results were obtained than for cleaning using reactive ion etching (see Fig 8.1).

Nitto and scotch tape technique

The starting material is a bulk piece of graphite from which the upper layers are cleaved using an adhesive tape. One can use an adhesive or a Nitto [200] tape, good results are obtained with both. The first cleaving is only performed to clean the sample and the tape is not further used. A second cleaving is executed with a fresh tape which is subsequently folded several times to distribute the graphite flake on its surface. For the fabrication of clean samples it seemed to be

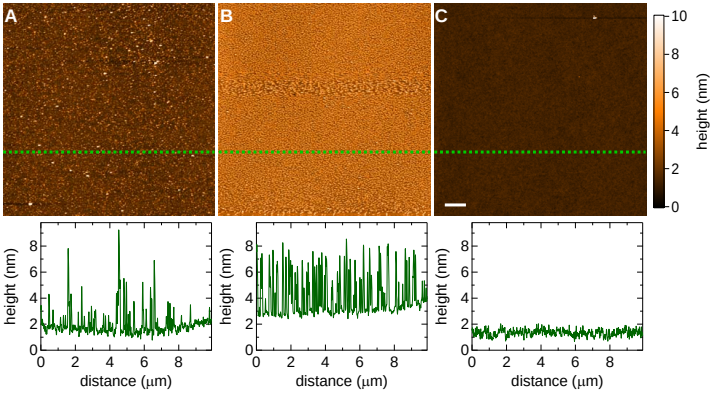

Figure 8.1: Differences in surface cleanliness. Panel A: wafer surface after UV grid deposition and lift off. Panel B: wafer surface after traditional RIE cleaning. Panel C: wafer surface after grid fabrication, flood exposure of wafer to UV light and additional 1 h development in UV resin developer. The roughness of the surface is smaller than after an RIE step, clearly visible in the line traces.

beneficial to start off with a single flake, placed on one side of the tape and cleaving its top side using the other half of the tape. The cleaving process can be repeated until an area as big as the waver piece used to deposit the graphite onto, is covered by thin graphite flakes. Often some unwanted thicker graphite pieces are found on the cleaving tape. Taking a new piece of tape (transfer tape), pressing it onto the cleaving tape and pulling the two apart, results in thinner flakes and mostly clean surfaces of the graphite flakes on the new tape.

The transfer tape is then deposited with the graphite flake side on top the prepared wafer piece and pressed onto its surface using the protecting cover of a pair of tweezers. For a good yield of large graphene flakes it seems important to pull the cover over the sample in the direction in which the tape is pulled off the wafer later. Holding the sample with tweezers, the tape is taken off the wafer by pulling it in vertical direction. Now the wafer piece can be pre-scanned using the optical microscope, checking if some suitable single layer graphene flake are found along the way. If the yield of SL flakes is not satisfactory, a fresh tape can be used to cleave the graphite flakes on the substrate again. Then, the sample is dripped into a beaker with aceton for approximately an hour to get a good deal of the glue residues off the sample surface. In any case, for further processing it is not of importance if not all the residues are off the SiO_2 surface. However, graphene flakes with glue residues should not be processed further, as the influence of the glue on the samples is not clear.

PDMS

Another technique for the fabrication of graphene flakes, especially long and thin ribbons [201], is the transfer printing of graphite using a PDMS (polydimethyl siloxane) stamp [202]. The graphite surfaces are expected to be cleaner compared to the flakes fabricated with the tape. It is, however, much more time consuming than the tape method, as one has to prepare the stamp, which take about half a day. To save time in the long run, several stamps can be prepared simultaneously.

For the fabrication of the stamp a mold is needed as the starting components are liquid and harden during backing. Plastic petri dishes with a diameter of about 4cm can be employed as a mold. To ensure a flat stamp surface, a piece of SiO_2 is glued at the bottom of the petri dish. The SiO_2 wafer piece should be well fixed to the mold, using e.g. a two component glue, as the silicon wafer piece can break during stamp removal. In this case a new stamp has to be made as the SiO_2 shiver can damage the graphene during deposition.

PDMS stamp recipe		
Step	Process	Details
1	Pour components into a glass vial	silicon elastomer (15 ml), curing agent (0.2 ml)
2	Stir the mixture until liquid is filled with air bubbles	ca. 5 min, glass rod
3	Pour mixture into mold and let it rest until bubble diffused out of the liquid	ca. $1-2$ h
4	Bake mixture	1 h at $60°C$
5	Cut stamp out of mold and clean it	IPA, 10 min ultrasound, blow dry

Table 8.2: Summary of the PDMS fabrication. The whole processing time is around 4 hrs. It is therefore advisable to fabricate several stamps at the same time.

In table 8.2 the recipe for the fabrication of the PDMS stamps is shown. The two components for the stamp are purred into a glass vial holding 20 ml in a 1 : 3 ratio and then mixed using a glass rod. Thorough mixing of the components is important and should be done until small air bubbles fill the whole liquid. The mixture is then purred into the mold containing the SiO_2 wafer piece and is covered with a slightly larger petri dish. The mixture should be let at rest for about 2 h until no bubbles can be seen anymore. Then, the mold is placed into an oven at $60°C$ for 2 hours to harden it. Changing the baking time and length influences the flexibility of the stamp: longer baking time and higher temperatures increases the stiffness of the stamp. This can influence the transfer process of graphene: stiffer stamps e.g. are more difficult to handle. However, the PDMS graphene fabrication was not employed long enough to allow for a fully developed recipe for best possible transfer results.

After the baking, the PDMS stamp is taken out of the mold by cutting along the mold wall with a scalpel. The stamp can now be carefully pulled out, not bending it too hard as it still is adhered to the SiO_2 substrate at the bottom of the mold. If, for some reason, the stamp strongly sticks to

the wafer piece, one can separate the connection between the stamp and the wafer piece with the scalpel. As soon as the stamp is isolated, the parts not having been in contact with the SiO_2 wafer are cut off the stamp and put aside for the transfer process afterwards. Then, the stamp, together with the cut off parts, are dripped into a beaker with IPA, cleaned in ultrasound (100%) during 10 min and blow dried.

A bulk piece of graphite is cleaned by pressing one of the cut off PDMS parts put aside before hand, onto the surface of the graphite piece. The adhesion of the graphite to the PDMS piece can be regulated via the speed with which it is removed from the graphite surface. In general, the slower the PDMS piece is taken off a substrate, the less material sticks to the PDMS. Hence, if the PDMS piece is taken off the graphite piece fast, more graphite is cleaved form the bulk piece onto the PDMS surface. The process is repeated using the flat stamp on the cleaned part of the graphite, pulling the stamp rapidly form the graphite surface. Thereupon, the flat stamp is pressed onto the cleaned substrate and slowly pulled off, to enlarge the number of flakes transferred. In a last step, the samples are left in a beaker with acetone for one hour, rinsed with IPA and then blown dry.

hBN fabrication and transfer

The recipe described here was developed by and explained in [19] and includes several tricky steps which need to be executed carefully to ensure good results. For the fabrication of hexagonal boron nitride (hBN) samples two Si/SiO_2 wafer pieces with localization grid are needed. On one sample hBN fakes are exfoliated and suitable flakes of a few tens of nanometers in height are isolated using the optical microscope. Before scanning the sample, one can sonicate it quickly in IPA, removing badly sticking flakes from the sample surface. On the other wafer, a water soluble PVA and a PMMA layer are spined on top of each other as described in table 8.3.

PVA and PMMA resist spinning recipe for graphene transfer			
Step	Process	Details	Parameters
1	PVA resist, 100 nm	Spinning	3000 rpm, 40 s, 0 s ramp
2	PMMA resist, 150 nm	Spinning	4000 rpm, 40 s, 4 s ramp
		Bake	Hot plate, 75° C, 4 min

Table 8.3: Recipe for the spinning of the water soluble PVA and the PMMA layer used for the transfer of graphene samples from a SiO_2 substrate onto a hBN flake. Prebaking is usually made to evaporate possible water layers on the substrate surface.

Then, graphene is exfoliated onto the wafer piece with the PVA/PMMA layer using the tape method and localized using the optical microscope. Due to thickness variation of the PVA/PMMA layer, the flakes are difficult to spot and their thickness is hard to evaluate. A CCD camera, transferring the live image of the microscope to a screen where the contrast of the images can be adjusted, makes the searching much more comfortable and reliable. Two small triangles of blue scotch tape, glued onto the PVA/PMMA layer in the vicinity of the flake help identifying their position after removal of the wafer piece. The best way to cut and glue the triangles onto the sample surface is to use fine and pointy tweezers. With the use of a scalpel, the PVA/PMMA layer should be thoroughly removed, not less than 2 mm on three sides and on the remaining side at least 5,mm. It is important to scratch the resist layers fully off the wafer piece at the edges, otherwise the PVA layer comes not into contact with the water at all sides and the PMMA layer with the graphene flakes cannot be released. To release the PMMA layer used for transfer, water is filled into a petri onto which the sample is carefully deposited, slightly pressing the 5 mm cleaned edge underneath the water level. The water layer should be a

little bit deeper than the height of the wafer piece, such that the wafer can fall off easily. However, if the water layer is too deep, the wafer might tear the PMMA layer underneath the water surface when falling. In this case the graphene flake is lost and exfoliation has to be restarted. As soon as the PVA layer gets into contact with the water, dissolution of the PVA starts. Slowly, the wafer tilts downwards, leaving the hydrophobic PMMA layer on top of the water. Often the PMMA layer sticks heavily to the wafer surface at the positions of the triangles. Pushing a little bit against the wafer piece with a toothpick can solve the problem and release the wafer. When it is fully released, the PMMA layer with the graphene is fished out of the water employing a glass plate with a hole surrounded by a metal ring. Carefully, the glass plate is lowered underneath the PMMA layer still floating on the water surface and, using the blue triangles, the flake can easily be positioned in the middle of the hole. Lifting the glass plate slowly up, the PMMA layer get stuck to the glass surface. If the PMMA layer slips from its position, the glass plate can be lowered into the water again, releasing the PMMA layer.

Next, to remove the water, the glass plate is either left over night to dry, or, it can be placed onto a hot plate at 80° C for 2 hrs. Now the actual transfer has to be performed. For this, an old mask aligner is employed, as the position of the hBN and the graphene flake can easily be aligned. The wafer piece with the hBN flake is positioned at the exposure position whereas the glass plate with the graphene flake is fixed at the "mask" position such that the graphene flake is exposed. Now wafer with the hBN flake can be heated to around 120° C. As soon as the stage holding the hBN wafer has reached the wanted temperature, the graphene and hBN flakes are positioned on top of each other and slowly approached. The wafer is pressed onto the glass plate for several minutes before it is released again. Mostly, the hBN wafer sticks to the glass plate and needs to be shaken off softly. After a successful transfer, the PMMA layer needs to be removed by dripping the sample into hot (50° C) acetone for an hour and rinsing it subsequently with IPA before blow drying the sample.

In this section different ways of fabricating graphene flakes are summarized. First, the well known scotch tape technique was explained, using either a real scotch tape or a piece of Nitto tape to exfoliate the graphene flakes. Further, the production

of graphene using a PDMS stamp was elucidated, together with the processing steps needed for the PDMS stamp. The fabrication of the PDMS stamp can influence the outcome of the exfoliation, as its flexibility changes with backing time and temperature. In the last part of this section, the full transfer process for graphene exfoliation on hBN is outlined as it was used for the fabrication of the samples shown in this thesis. On the one hand, this method needs a lot of concentrated work involving ones concentration fully. On the other hand, however, the resulting sample compensate the effort with less disorder and better controllability towards chemical reactivity.

Before continuing with sample fabrication, the cleanliness and quality of the surface of the flakes needs to be investigated. Here, we used an AFM to perform the evaluations and exactly outline the geometry of the flakes and locating possible cracks in the flake. The next section summarizes the AFM measurements made.

AFM imaging

After deposition of the graphene flakes onto a SiO_2 or hBN substrate and localization of the flakes using the optical microscope, the quality of the flakes for transport measurements should be estimated. A rather time consuming but exact method is atomic force microscopy (AFM) scanning of the graphitic surface. The AFM allows one depict the surface morphology of the flakes with a resolution of a few nanometers in lateral direction and a few picometers in height. Therefore, residues on the flake surface, as well as cracks and holes can be depicted.

Before starting with the AFM scans, the electronics of the AFM machine should be turned on at least half an hour before scanning is begun, together with the computer programm for the AFM measurements to allow equilibration of the laser. AFM images are in fact measurements of the changes in z-position of the scanning tip when moving over the investigated surface. The height measurement is performed by shining a laser at the reflecting back side of the scanning tip and detecting it on a detector consisting of four segments. Due to the up and down movement of the AFM tip, the laser is

deflected in vertical direction on the detector, allowing the measurement of height changes of a few nanometers. During the equilibration of the laser, the AFM tip can be mounted to the tip holder. Now, the holder can be fixed to the AFM stage and the laser can already be placed at the far end of the AFM tip to allow equilibration of the tip and the laser. The positioning needs some training but there are some tricks. First, one can check if the tip is in the vicinity of the laser by moving the laser only to the left and right. Most of the time, the laser hits the tip, indicated by a signal on the detector. Then, fine adjustment of the laser position starts and the sum signal at the detector should be increased. If, however, the laser is not in close vicinity to the tip, it is easier to start by moving the laser to the base of the tip, where it is cut out of the silicon chip. Still, a signal should be received on the detector. Then, the laser is slowly moved forward along the tip until no signal is seen on the detector and then slightly back such that the laser is back on the tip. Now, the laser can slowly be moved, say to the left at the edge of the tip. Moving the laser to the front, it will fall off the tip. In this moment, the laser should again be moved to the left until it is on the tip. This process can be repeated until the laser is

at the front of the tip. Then, the signal on the detector can be maximized.

Further, the sample can be prepared by either putting it directly underneath the AFM and fixing using vacuum. For this, the sample needs to be large, as the hole for vacuum fixation is large. Small sample can be attached to a magnetic chip using doubly sided scotch tape and a piece of sticky post-it. The doubly sided scotch tape is glued onto the magnetic chip and the post-it is deposited with the sticky side on top. Then, the sample can be place onto the post-it. The scotch tape is too strong for direct deposition of the flake onto it.

The actual scanning of a sample seems to be very easy, however, usually one encounters quickly subtle difficulties which need some experience to be solved. Often encountered problems are listed here, however, much more can occur.

If the electronic regulation of the tip movement is not correctly adjusted, this can generate oscillation of the tip which are visible in the scans (see Fig. 8.2A). Less vibrations can be obtained when the $P - I$ values are lowered slightly. However, it strongly depends on the sample and on the environment what the exact values of the regulators are. Further, in

some cases the tip does not approach the surface of the sample correctly, it just stops approaching too far away. Also, jumps of the tip during scanning can occur. It is not clear to the author what causes this, however, both situations were observed with higher probability for samples exposed to a hydrogen plasma. It is not clear what causes both effects and how one can get rid of them.

Further, often the scanning tip pics up some dirt particles lying on the substrate leading to so-called tip-effects. As visible in Fig. 8.2B, the particle on the image all look the same. In fact, at each position of another dirt particle on the substrate, not the structure of the substrate is depicted but rather a mixture between the substrate and the particle on the tip. In such cases it makes sense to change to a new tip. Also, sometimes stripes are seen on the images, changing shape with each scan (see Fig. 8.2). Such lines can occur when particles are moved on the surface by the tip, pushing the particle in each line slightly forward.

Sometimes the graphene samples we measured also showed structures on their surface resembling a water bubble lying underneath the flake. The bubble also changes shape during scanning, indicating that the material is not tightly bound to

the sample surface. It is known, that water deposits sometimes on SiO_2 substrates [64] and it was also seen to accumulate underneath graphene sheets on mica [203]. To get rid of the water, the samples can be annealed at 100° C for half an hour approximately.

After having chosen a suitable flake using the AFM and Raman measurements, the actual device can be fabricated using e-beam lithography to pattern the wished structures into the graphene or fabricate contacts onto the flake.

Ebeam structures

After the localisation and identification of suitable graphene flakes, the contacting or shaping of the samples need to be made. Ebeam lithography allows for the fabrication of almost any kind of geometry with sizes between a few hundred of micrometers down to around a few nanometers ($\approx$ 15 nm). Here, the recipes used for the fabrication of the graphene Hall bars, the contacts to various samples and the processing of the holes needed to hydrogen plasma etch our graphene flakes are listed.

Before starting with the e-beam lithography itself, the resits

is spun onto the surface of the samples. Here, we always used negative tone resist, therefore, the exposed resist will be washed away during development. Depending on the size of the structures, the chosen thickness of the resist will vary. In general, smaller samples will be easier to achieve using thin layers of PMMA and high acceleration voltages. When exposing the resist to the e-beam, the accelerated electrons break the bonds of the molecules, allowing the development of the structures. However, the electrons can additionally get multiply scattered during their travel through the resist which further exposes the resist also at the edges of the small structures. If the resist is thin, the electrons get less scattered and add less to this type of unwanted exposure, also called a proximity effect. Additionally, backscattered electrons, mainly form the SiO_2 can again further expose the resist, leading to larger structures as intentionally designed. The influence of the backscattered electrons is less strong, if high accelerating voltages are used. In table 8.4 the various PMMA spinning recipes are shown, listed from the smallest e-beam structures to the largest.

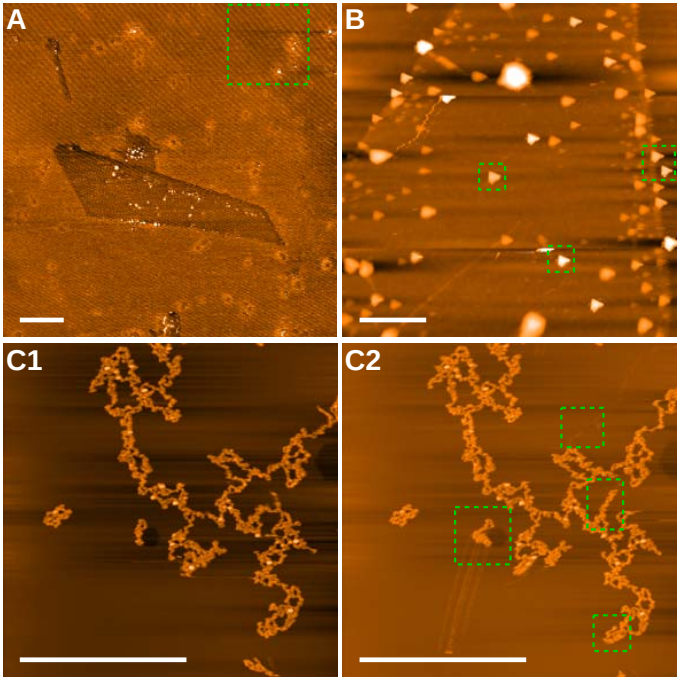

Figure 8.2: Oscillations and tip effects as seen during fabrication. Panel A: AFM scan of a graphene flake on SiO_2. The green dashed square indicates the oscillation in the scan. Panel B: AFM scan of a graphene flake on SiO_2. Tip effect due to a dirty tip, clearly depicted by the triangular shape of the scanned dots on the sample. Panel C1 and C2: loose molecules on a graphite substrate are pushed by the tip. In each scan the position of the dirt particles change. All the scale bars are $1\,\mu$m long

PMMA resist spinning and e-beam exposure recipe for e-beam structures			
Step	Process	Details	Parameters
Hall bar devices, chapter 3			
1	Hall bar, 1.5% PMMA	Prebake	Hot plate, 180° C, 2 min
		Spinning	5500 rpm, 40 s, 4 s ramp
		Bake	Hot plate, 180° C, 4 min
2	Contacts large and pads, 310 nm	Spinning	3000 rpm, 40 s, 8 s ramp
		Bake	Hot plate, 180° C, 5 min
Circular holes of chapter 4			
1	Circular holes	Spinning	5500 rpm, 40 s, 8 s ramp
		Bake	Hot plate, 100 − 180° C, 5 min
Contacts fabricated in chapter 5			
1		Spinning	3000 rpm, 40 s, 8 s ramp
		Bake	Hot plate, 180° C, 5 min
4	Contacts large and pads, 310 nm	Spinning	3000 rpm, 40 s, 8 s ramp
		Bake	Hot plate, 180° C, 5 min

Table 8.4: Recipe for the spinning of PMMA for the fabrication of various structures needed in this work. Here, no prebaking step was made, as this can lead to the rolling up of graphene sheets which then are lost for further fabrication [204]. Also, the ramp up speed for the PMMA spinning turned out to be a crucial factor for the stability of the flakes. The slower the ramp up speed, the rather the flakes are holding onto the substrate [204]. However, slower ramp up speed can lead to slightly thicker PMMA layers.

After spinning the PMMA resist onto the sample surface, gold particles of sizes between 50 nm and 200 nm are deposited with a toothpick at the corners of the wafer chip. The gold particles are used to focus the electron beam, allowing the writing of 15 nm structures. Further, the lower left corner of the sample can be labeled by carefully scratching two lines onto the substrate surface, enabling the alignment of the sample and machine coordinate systems. Then the sample can be fixed onto the sample holder by clamping the sample with one of the metal clamps of the holder, which is then mounted into the e-beam machine.

Below all the different exposures are listed:

- Hall bar etching: EHT=30 kV, aperture=10 μm, working distance=9.1 mm, area dose=800 μ As/cm^2, area step size=10 nm
- Hall bar contacts fine: EHT=20 kV, aperture=10 μm, working distance=9.1 mm, area dose=350 μ As/cm^2, area step size=15 nm
- Hall bar contacts large: EHT=20 kV, aperture=120 μm, working distance=17.7 mm, area dose=350 μ As/cm^2, area step size=15 nm

- Circular holes: EHT=30 kV, aperture=10 μm, working distance=9.1 mm, area dose=800 μ As/cm^2, area step size=3.9 nm

- van der Pauw contacts fine: EHT=20 kV, aperture=10 μm, working distance=9.1 mm, area dose=300 μ As/cm^2, area step size=6.3 nm

- van der Pauw contacts large: EHT=20 kV, aperture=120 μm, working distance=17.7 mm, area dose=350 μ As/cm^2, area step size=62.3 nm

After e-beam patterning of the sample, the PMMA resin is developed for 90 s in the *ma*− developer, and the development process is stopped in IPA, immersing the sample into the liquid for 30 s. Then, the position of the written structures can be checked by looking at the sample in the optical microscope, employing the dark field mode to make structures smaller than a few tens of microns visible. After the development of the e-beam structure, either the samples are etched into their final shape or metal is evaporated onto the developed structures.

Reactive ion etching of graphene

The patterned e-beam resin can be used as a mask for reactive ion etching (RIE) in an oxygen/argon plasma, protecting the graphene flakes against the reactive ions of the plasma. The recipe used to etch the graphene flakes is listed in table 8.5 below. A mixture of oxygen and argon is used as oxygen interacts chemically and argon physically with the PMMA or graphene during the etch process. Varying the amount of argon and oxygen changes the main type of interaction. For graphene etching a higher percentage of oxygen is favorable, on the other hand, for cleaning purposes, a higher amount of argon is advantageous. However, one should be careful when using graphene for cleaning of SiO_2 substrates. The author investigated the roughening of the substrate during RIE exposure of silicon wafers and found, that the roughness increases by a factor of 3. Therefore, the wafer surfaces were not cleaned using RIE.

Base pressure	Working pressure	Gas	Gas flow	Power	DC bias	Time
mbar	mTorr			W	V	s
$5 \cdot 10^{-5}$	25	O_2/Ar	8/16	30	160	10

Table 8.5: Etch procedure for the etching of graphene Hall bars and for the fabrication of predefined circular defects for subsequent H plasma exposure.

Metal evaporation and bonding

Having developed the ebeam structures and, if necessary etched the graphene flakes in a RIE step, the samples can be built into the evaporator (Sharon evaporator in this case). First, the chamber of the evaporator needs to be opened to reach the sample holder. The sample can be fixed to the holder by either using sticky carbon tapes or metallic plates fixed with screws. The plates have the advantage that parts of the resin is not covered with metal, facilitating the lift-off of the metal in the following step. Further, the samples break less easily when removing them from the sample holder after evaporation. However, during mounting, the plates can scratch over the surface if one is not careful enough, destroying the e-beam structures written or even the graphene flake lying underneath. Putting a finger next to the metal plate, on the side right side when mounting it, on the other when taking it off the holder, one can reduce the damages done to the samples.

After having built the sample holder into the evaporator, one has to check if the correct materials are in the respective crucibles and if there is enough of each present. Especially

the gold target should be weighed, as not less than 25 gramms of pure gold should be in the liner. If there is not enough, please refill the target. Further, the crystal life should be checked and, if necessary exchanged. Then, the chamber can be closed and pumped down.

When evaporating gold, one should turn up the current slowly, as the heat capacitance of the material is small and the target does not uniformly heat up. If the current is heated too fast, the evaporation rate will not be stable and, at some point, overshoot to extremely high values. Also turning the current back to zero should be performed slowly, such that the molten gold can uniformly cool down. Further, the gold target should, for the same reason be heated by moving the ebeam over the largest area of the target possible. Otherwise, only a very small part of the target is heated and a hole can be burned into the material, leading to the breaking of the liner and the mixing of the liner material and the gold. In this case, a new gold target has to be bought, which is expensive. Another material which needs some caution when evaporating is chromium: it does not evaporate really, it rather sublimates. After evaporation, the sample is taken out of the evaporator and metal lift-off can

be performed in warm acetone (50° C).

As soon as the sample has passed through all the fabrication steps needed, it can be prepared for electrical measurements by bonding it to a chip carrier. First, the chip carrier has to be cleaned, using the three solvent cleaning mentioned in table 8.1. Then, the sample is glued into the chip carrier by applying a small droplet of silver paint in the middle of the chip carrier and softly pressing the chip onto the droplet. If too much silver paint is deposited, it can spread and move up the sides of the chip, connecting the back plane of the chip with the top of the sample. As the back plane of the carrier is used to apply voltages to the back gate of the chip, depending on the position of the contact pads and bond wires, short cuts can occur between the back gate and the contacts. After approximately $5 - 10$ min the paint has dried (one can check by softly pushing the wafer with a pair of tweezers) and bonding can start.

Bibliography

[1] P.R. Wallace, *The Band Theory of Graphite*, Phys. Rev. **71**, 622 (May 1947).

[2] K. Tanaka, K. Okahara, M. Okada, and T. Yamabe, *Electronic properties of bucky tube model*, Chem. Phys. Lett. **191**, 469 (April 1992).

[3] K.S. Novoselov, A.K. Geim, S.V. Morozov, D. Jiang, Y. Zhang, S.V. Dubonos, I.V. Grigorieva, and A.A. Firsov, *Electric Field Effect in Atomically Thin Carbon Films*, Science **306**, 666 (October 2004).

[4] K.S. Novoselov, A.K. Geim, S.V. Morozov, D. Jiang, M.I. Katsnelson, I.V. Grigorieva, S.V. Dubonos, and A.A. Firsov, *Two-dimensional gas of massless Dirac fermions in graphene*, Nature **438**, 197 (November 2005).

[5] Y. Zhang, Y.-W. Tan, H.L. Stormer, and P. Kim, *Experimental observation of the quantum Hall effect and Berry's phase in graphene*, Nature **438**, 201 (November 2005).

[6] K. Nakada, M. Fujita, G. Dresselhaus, and M.S. Dresselhaus, *Edge state in graphene ribbons: Nanometer size effect and edge shape dependence*, Phys. Rev. B **54**, 17954 (December 1996).

[7] M. Fujita, K. Wakabayashi, K. Nakada, and K. Kusakabe, *Peculiar Localized States at Zigzag Graphite Edge*, J. Phys. Soc. Jpn. **65**, 1920 (July 1996).

[8] L. Brey and H.A. Fertig, *Electronic states of graphene nanoribbons studied with the Dirac equation*, Phys. Rev. B **73**, 235411 (June 2006).

[9] Y.-W. Son, M.L. Cohen, and S.G. Louie, *Energy Gaps in Graphene Nanoribbons*, Phys. Rev. Lett. **97**, 216803 (November 2006).

[10] Y.-W. Son, M.L. Cohen, and S.G. Louie, *Half-metallic graphene nanoribbons*, Nature **444**, 347 (November 2006).

[11] M. Han, B. Özyilmaz, Y. Zhang, and P. Kim, *En-*

ergy Band-Gap Engineering of Graphene Nanoribbons, Phys. Rev. Lett. **98**, 206805 (May 2007).

[12] B. Özyilmaz, P. Jarillo-Herrero, D. Efetov, and Pf. Kim, *Electronic transport in locally gated graphene nanoconstrictions*, Appl. Phys. Lett. **91**, 192107 (November 2007).

[13] F. Molitor, J. Güttinger, C. Stampfer, D. Graf, T. Ihn, and K. Ensslin, *Local gating of a graphene Hall bar by graphene side gates*, Phys. Rev. B **76**, 245426 (December 2007).

[14] F. Sols, F. Guinea, and A. Neto, *Coulomb Blockade in Graphene Nanoribbons*, Phys. Rev. Lett. **99**, 166803 (October 2007).

[15] J. Martin, N. Akerman, G. Ulbricht, T. Lohmann, J.H. Smet, K. von Klitzing, and A. Yacoby, *Observation of electron hole puddles in graphene using a scanning single-electron transistor*, Nat. Phys. **4**, 144 (November 2007).

[16] K.I. Bolotin, K.J. Sikes, Z. Jiang, M. Klima, G. Fudenberg, J. Hone, P. Kim, and H.L. Stormer, *Ultrahigh*

electron mobility in suspended graphene, Solid State Commun. **146**, 351 (June 2008).

[17] J. Moser, A. Barreiro, and A. Bachtold, *Current-induced cleaning of graphene*, Appl. Phys. Lett. **91**, 163513 (October 2007).

[18] T. Taniguchi and K. Watanabe, *Synthesis of high-purity boron nitride single crystals under high pressure by using Ba BN solvent*, J. Cryst. Growth **303**, 525 (May 2007).

[19] C.R. Dean, A.F. Young, I. Meric, C. Lee, L. Wang, S. Sorgenfrei, K. Watanabe, T. Taniguchi, P. Kim, K.L. Shepard, and J. Hone, *Boron nitride substrates for high-quality graphene electronics*, Nat. Nanotech. **5**, 722 (August 2010).

[20] A.M. Goossens, S.C.M. Driessen, T.A. Baart, K. Watanabe, T. Taniguchi, and L.M.K. Vandersypen, *Gate-Defined Confinement in Bilayer Graphene-Hexagonal Boron Nitride Hybrid Devices*, Nano Letters **12**, 4656 (September 2012).

[21] X. Li, X. Wang, L. Zhang, S. Lee, and H. Dai, *Chemi-*

cally Derived, Ultrasmooth Graphene Nanoribbon Semiconductors, Science **319**, 1229 (February 2008).

[22] L. Jiao, X. Wang, G. Diankov, H. Wang, and H. Dai, *Facile synthesis of high-quality graphene nanoribbons*, Nat. Nanotechnol. **5**, 321 (April 2010).

[23] R. Yang, L. Zhang, Y. Wang, Z. Shi, D. Shi, H. Gao, E. Wang, and G. Zhang, *An Anisotropic Etching Effect in the Graphene Basal Plane*, Adv. Mater. **22**, 4014 (September 2010).

[24] X. Wang and H. Dai, *Etching and narrowing of graphene from the edges*, Nature Chemistry **2**, 661 (June 2010).

[25] L. Xie, L. Jiao, and H. Dai, *Selective Etching of Graphene Edges by Hydrogen Plasma*, J. Amer. Chem. Soc. **132**, 14751 (October 2010).

[26] J. Cai, P. Ruffieux, R. Jaafar, M. Bieri, Th. Braun, S. Blankenburg, M. Muoth, A.P. Seitsonen, M. Saleh, X. Feng, K. Müllen, and R. Fasel, *Atomically precise bottom-up fabrication of graphene nanoribbons*, Nature **466**, 470 (July 2010).

[27] G. Diankov, M. Neumann, and D. Goldhaber-Gordon,

Extreme Monolayer-Selectivity of Hydrogen-Plasma Reactions with Graphene, ACS Nano **7**, 1324 (February 2013).

[28] D.C. Elias, R.R. Nair, T.M.G. Mohiuddin, S.V. Morozov, P. Blake, M.P. Halsall, A.C. Ferrari, D.W. Boukhvalov, M.I. Katsnelson, and A.K. Geim, *Control of graphene's properties by reversible hydrogenation: evidence for graphane*, Science **323**, 610 (January 2009).

[29] M. Wojtaszek, N. Tombros, A. Caretta, P.H.M. van Loosdrecht, and B.J. van Wees, *A road to hydrogenating graphene by a reactive ion etching plasma*, J. Appl. Phys. **110**, 063715 (September 2011).

[30] W. Primak and L.H. Fuchs, *Electrical Conductivities of Natural Graphite Crystals*, Phys. Rev. **95**, 22 (July 1954).

[31] L. Edman, B. Sundqvist, E. McRae, and E. Litvin Staszewska, *Electrical resistivity of single crystal graphite under pressure: An anisotropic three dimensional semimetal*, Phys. Rev. B **57**, 6227 (March 1998).

[32] I.L. Spain, A.R. Ubbelohde, and D.A. Young, *Electronic Properties of Well Oriented Graphite*, Phil. Trans. R. Soc. Lond. A **262**, 345 (October 1967).

[33] T. Tsuzuku, *Anisotropic Electrical Conductivity in Relation to the Stacking Disorder in Graphite*, Carbon **17**, 293 (1979).

[34] I.L. Spain, *Chemistry and Physics of Carbon*, Vol.19, Marcel Dekker, New York, 1981.

[35] B.T. Kelly, *Physics of Graphite*, Applied Science Publisher, 1981.

[36] D.Z. Tsang and M.S. Dresselhaus, *The c-axis Electrical Conductivity of Kish Graphite*, Carbon **14**, 43 (1976).

[37] D.L. Maslov, V.I. Yudson, and A.M. Somoza, *Delocalization by Disorder in Layered Systems*, Phys. Rev. Lett. **102**, 216601 (May 2009).

[38] D.S.L. Abergel, V. Apalkov, J. Berashevich, K. Ziegler, and T. Chakraborty, *Properties of graphene: a theoretical perspective*, Adv. Phys. **59**, 261 (July 2010).

[39] S. Das Sarma, S. Adam, E.H. Hwang, and E. Rossi, *Electronic transport in two-dimensional graphene*, Rev. Mod. Phys. **83**, 407 (May 2011).

[40] P. Atkins and J. de Paula, *Physical Chemistry*, Oxford Univerity Press, 8th edition, 2006.

[41] J.W. McClure, *Energy band Graphite*, IBM J. **8**, 255 (July 1964).

[42] G.W. Semenoff, *Condensed-Matter Simulation of a Three-Dimensional Anomaly*, Phys. Rev. Lett. **53**, 2449 (August 2013).

[43] M.I. Katsnelson, *Graphene: Carbon in Two Dimensions*, Cambridge University Press, 2012.

[44] H. Raza, *Graphene Nanoelectronics*, Springer, 2012.

[45] Th. Ihn, *Semiconducting Nanostructures: Quantum States and Electronic Transport*, Oxford University Press, 2010.

[46] M.I. Katsnelson, K.S. Novoselov, and A.K. Geim, *Chiral tunnelling and the Klein paradox in graphene*, Nat. Phys. **2**, 620 (August 2006).

[47] E.H. Hall, *On a New Action of the Magnet on Electric Currents*, Amer. J. Math. **2**, 287 (September 2007).

[48] C.J.W. Beenakker and H. van Houten, *Quantum Transport in Semiconductor Nanostructures*, Solid State Phys. **44**, 1 (1991).

[49] Ch. Kittel, *Einführung in die Festkörperphysik*, Oldenbourg Verlag München Wien, 2005.

[50] Y. Zheng and T. Ando, *Hall conductivity of a two-dimensional graphite system*, Phys. Rev. B **65**, 245420 (June 2002).

[51] L.J. van der Pauw, *A Method of measuring the resistivity and Hall coefficient on lamellae of arbitray shape*, Philips Technical Review **20**, 220 (1958).

[52] J.D. Irwin, *Basic Engineering Circuit Analysis*, Macmillan, New York, 1987.

[53] J. Klinovaja and D. Loss, *Giant Spin-Orbit Interaction Due to Rotating Magnetic Fields in Graphene Nanoribbons*, Phys. Rev. X **3**, 011008 (January 2013).

[54] A. Saffarzadeh and R. Farghadan, *A spin-filter device based on armchair graphene nanoribbons*, Appl. Phys. Lett. **98**, 023106 (January 2011).

[55] R. Farghadan and E. Saievar-Iranizad, *Spin polarized transport in zigzag edge graphene nanoribbon junctions*, J. Appl. Phys. **111**, 014304 (June 2012).

[56] W.M. Lomer, *The valence bands in two-dimensional graphite*, Proc. R. Soc. A **227**, 330 (January 1955).

[57] Y. Kobayashi, K. Fukui, T. Enoki, K. Kusakabe, and Y. Kaburagi, *Observation of zigzag and armchair edges of graphite using scanning tunneling microscopy and spectroscopy*, Phys. Rev. B **71**, 193406 (May 2005).

[58] T.H.P. Chang, *Proximity effect in electron-beam lithography*, J. Vac Sci. Technol. **12**, 1271 (November 1975).

[59] A.N. Broers, A.C.F. Hoole, and J.M. Ryan, *Electron beam lithography Resolution limits*, Microelectron. Eng. **32**, 131 (1996).

[60] E. Mucciolo, A. Castro Neto, and C. Lewenkopf, *Conductance quantization and transport gaps in disordered graphene nanoribbons*, Phys. Rrev. B **79**, 075407 (February 2009).

[61] P. Gallagher, K. Todd, and D. Goldhaber-Gordon, *Disorder induced gap behavior in graphene nanoribbons*, Phys. Rev. B **81**, 115409 (March 2010).

[62] P. Blake, E.W. Hill, A.H. Castro Neto, K.S. Novoselov, D. Jiang, R. Yang, T.J. Booth, and A.K. Geim, *Making graphene visible*, Appl. Phys. Lett. **91**, 063124 (August 2007).

[63] D.S.L. Abergel, A. Russell, and V.I. Falko, *Visibility of*

graphene flakes on a dielectric substrate, Appl. Phys. Lett. **91**, 063125 (August 2007).

[64] M. Lafkioti, B. Krauss, T. Lohmann, U. Zschieschang, H. Klauk, K. von Klitzing, and J.H. Smet, *Graphene on a Hydrophobic Substrate: Doping Reduction and Hysteresis Suppression under Ambient Conditions*, Nano Lett. **10**, 1149 (April 2010).

[65] M. Ishigami, J.H. Chen, W.G. Cullen, M.S. Fuhrer, and E.D. Williams, *Atomic Structure of Graphene on SiO2*, Nano Lett. **7**, 1643 (June 2007).

[66] A.C. Ferrari, J.C. Meyer, V. Scardaci, C. Casiraghi, M. Lazzeri, F. Mauri, S. Piscanec, D. Jiang, K.S. Novoselov, S. Roth, and A.K. Geim, *Raman Spectrum of Graphene and Graphene Layers*, Phys. Rev. Lett. **97**, 187401 (October 2006).

[67] L.M. Malard, M.A. Pimenta, G. Dresselhaus, and M.S. Dresselhaus, *Raman spectroscopy in graphene*, Phys. Rep. **473**, 51 (April 2009).

[68] A.C. Ferrari and D.M. Basko, *Raman spectroscopy as a versatile tool for studying the properties of graphene*, Nat. Nanotechnol. **8**, 235 (April 2013).

[69] C. Thomsen and S. Reich, *Double resonant Raman scattering in graphite*, Phys. Rev. Lett. **85**, 5214 (December 2000).

[70] L. Cancado, M. Pimenta, B. Neves, M. Dantas, and A. Jorio, *Influence of the Atomic Structure on the Raman Spectra of Graphite Edges*, Phys. Rev. Lett. **93**, 247401 (December 2004).

[71] C. Casiraghi, A. Hartschuh, H. Qian, S. Piscanec, C. Georgi, A. Fasoli, K.S. Novoselov, D.M. Basko, and A.C. Ferrari, *Raman Spectroscopy of Graphene Edges*, Nano Lett. **9**, 1433 (April 2009).

[72] Z.H. Ni, T. Yu, Z.Q. Luo, Y.Y. Wang, L. Liu, C.P. Wong, J. Miao, W. Huang, and Z.X. Shen, *Probing Charged Impurities in Suspended Graphene Using Raman Spectroscopy*, ACS Nano **3**, 569 (March 2009).

[73] M. Moisan, C. Beaudry, and P. Leprince, *A new HF Device for the Production of Long Plasma Columns at a High Electron Density*, Phys. Lett. A **50**, 125 (November 1974).

[74] M. Moisan, C. Beaudry, and P. Leprince, *A Small Microwave Plasma Source For Long Column Production*

Without Magnetic Field, IEEE Trans. Pla. Sci. **3**, 55 (June 1975).

[75] M. Moisan, P. Leprince, C. Beaudry, and E. Bloyet, *Devices and Methods of Using HF Waves to Energize a Column of Gas Enclosed in an Insulating Casing*, United States Patent **4049940** (September 1977).

[76] M. Moisan, Z. Zakrzewski, and R. Pantel, *The theory and characteristics of an eficient surface wave launcher (surfatron) producing long plasma columns*, Appl. Phys. **12**, 219 (July 1978).

[77] R.K. Grubbs and S.M. George, *Attenuation of hydrogen radicals traveling under flowing gas conditions through tubes of different materials*, J. Vac. Sci. Technol A **24**, 486 (2006).

[78] A. von Keudell, *Einführung in die Plasmaphysik, Vorlesungsskript*, University of Bochum, 2012.

[79] A. von Keudell, *Einführung in die Plasmaphysik II: Niedertemperaturplasmen, Vorlesungsskript*, University of Bochum, 2012.

[80] M. Selby and G.M. Hieftje, *Taming the surfatron*, Spectroch. Acta B **42**, 285 (June 1987).

[81] V.M.M. Glaude, M. Moisan, R. Pantel, P. Leprince, and J. Marec, *Axial electron density and wave power distributions along a plasma column sustained by the propagation of a surface microwave*, J. Appl. Phys. **51**, 5693 (November 1980).

[82] J. Margot and M. Moisan, *Plasma processing of Semiconductors*, Kluwer Academic Publishers, 1997.

[83] J. Margot-Chaker, M. Moisan, M. Chaker, V.M.M. Glaude, P. Lauque, J. Paraszczak, and G. Sauve, *Tube diameter and wave frequency limitations when using the electro magnetic surface wave in the m=1 (dipolar) mode to sustain a plasma column*, J. Appl. Phys. **66**, 4134 (November 1989).

[84] M. Moisan and Z. Zakrzewski, *Plasma sources based on the propagation of electromagnetic surface waves*, J. Phys. D **24**, 1025 (1991).

[85] R.L. Merlino, *Understanding Langmuir probe current-voltage characteristics*, American J. Phys. **75**, 1078 (December 2007).

[86] U. Stroht, *Plasmaphysik*, Vieweg und Teubner Verlag, 2011.

[87] W.V. Smith, *The Surface Recombination of H Atoms and OH Radicals*, J. Chem. Phys. **11**, 110 (March 1943).

[88] Y.C. Kim and M. Boudart, *Recombination of O, N and H atoms on Silica: Kinetics and Mechanism*, Langmuir **7**, 2999 (January 1991).

[89] R.K. Janev, D. Reiter, and U. Samm, *Collision Processes in Low Temperature Hydrogen Plasmas*, Forschungszentrum Jülich GmbH, Zentralbibliothek, 2003.

[90] S. Weissman and E.A. Mason, *Estimation of the Mutual Diffusion Coefficient of Hydrogen Atoms and Molecules*, J. Chem. Phys. **36**, 794 (February 1962).

[91] T.A.R. Hansen, J.W. Weber, P.G.J. Colsters, D.M.H.G. Mestrom, M.C.M. van de Sanden, and R. Engeln, *Synergistic etch rates during low-energetic plasma etching of hydrogenated amorphous carbon*, J. Appl. Phys. **112**, 013302 (July 2012).

[92] A. Horn, A. Schenk, J. Biener, B. Winter, C. Lutterloh, M. Wittmann, and J. Küppers, *H atom impact induced*

chemical erosion reaction at C: H film surfaces, Chem. Phys. Lett. **231**, 193 (December 1994).

[93] B.V. Mech, A.A. Haasz, and J.W. Davis, *Model for the chemical erosion of graphite due to low-energy H^+ and D^+ impact*, J. Appl. Phys. **84**, 1655 (August 1998).

[94] J. Biener, A. Schenk, B. Winter, C. Lutterloh, A. Horn, and J. Küpper, *Elementary steps of the interaction of C: H film surfaces with thermal H/D atoms*, Vacuum **46**, 903 (1995).

[95] J. Roth, *Chemical erosion of carbon based materials in fusion devices*, J. Nucl. Mater. **266**, 51 (1999).

[96] M. Wittmann and J. Küppers, *A model of hydrogen impact induced chemical erosion of carbon based on elementary reaction steps*, J. Nucl. Mater. **227**, 186 (1996).

[97] Z.J. Pan and R.T. Yang, *The mechanism of methane formation from the reaction between graphite and hydrogen*, J. Catal. **123**, 206 (1990).

[98] M.Y. Han, J.C. Brant, and Ph. Kim, *Electron Transport in Disordered Graphene Nanoribbons*, Phys. Rev. Lett. **104**, 056801 (February 2010).

[99] D. Kölbl and D.M. Zumbühl, *Transport spectroscopy of disordered graphene quantum dots etched into a single graphene flake*, arXiv:1307.8163 (2013).

[100] X. Liu, J. Oostinga, A. Morpurgo, and L.M.K. Vandersypen, *Electrostatic confinement of electrons in graphene nanoribbons*, Phys. Rev. B **80**, 121407 (September 2009).

[101] F Molitor, C Stampfer, J Güttinger, A Jacobsen, T Ihn, and K Ensslin, *Energy and transport gaps in etched graphene nanoribbons*, Semicond. Sci. Technol. **25**, 034002 (March 2010).

[102] C. Stampfer, J. Güttinger, S. Hellmüller, F. Molitor, K. Ensslin, and T. Ihn, *Energy Gaps in Etched Graphene Nanoribbons*, Phys. Rev. Lett. **102**, 506403 (February 2009).

[103] D.K. Ki and A.F. Morpurgo, *Crossover from Coulomb Blockade to Quantum Hall Effect in Suspended Graphene Nanoribbons*, Phys. Rev. Lett. **108** (June 2012).

[104] B. Huard, N. Stander, J. Sulpizio, and D. Goldhaber-Gordon, *Evidence of the role of contacts on the ob-*

served electron-hole asymmetry in graphene, Phys. Rev. B **78**(12), 121402 (September 2008).

[105] D.B. Farmer, R. Golizadeh-Mojarad, V. Perebeinos, Y.-M. Lin, G.S. Tulevski, J.C. Tsang, and P. Avouris, *Chemical Doping and Electron-Hole Conduction Asymmetry in Graphene Devices*, Nano Letters **9**(1), 388 (January 2009).

[106] F. Schedin, A.K. Geim, S.V. Morozov, E.W. Hill, P. Blake, M.I. Katsnelson, and K.S. Novoselov, *Detection of individual gas molecules adsorbed on graphene*, Nat. Mater. **6**, 652 (July 2007).

[107] J.-H. Chen, C. Jang, S. Adam, M.S. Fuhrer, E.D. Williams, and M. Ishigami, *Charged-impurity scattering in graphene*, Nat. Phys. **4**, 377 (April 2008).

[108] E. Hwang, S. Adam, and S. Das Sarma, *Carrier Transport in Two-Dimensional Graphene Layers*, Phys. Rev. Lett. **98**, 186806 (May 2007).

[109] Y.-W. Tan, Y. Zhang, K. Bolotin, Y. Zhao, S. Adam, E.H. Hwang, S. Das Sarma, H.L. Stormer, and Ph. Kim, *Measurement of Scattering Rate and Minimum*

Conductivity in Graphene, Phys. Rev. Lett. **99**, 246803 (December 2007).

[110] S. Adam, E.H. Hwang, V.M. Galitski, and S. Das Sarma, *A self-consistent theory for graphene transport*, Proc. Natl. Acad. Scie. **104**, 18392 (2007).

[111] S. Adam, E.H. Hwang, and S. Das Sarma, *Scattering mechanisms and Boltzmann transport in graphene*, Physica E **40**, 1022 (March 2008).

[112] J.-H. Chen, W. Cullen, C. Jang, M. Fuhrer, and E. Williams, *Defect Scattering in Graphene*, Phys. Rev. Lett. **102** (June 2009).

[113] J. Robinson, H. Schomerus, L. Oroszlany, and V. Falko, *Adsorbate-Limited Conductivity of Graphene*, Phys. Rev. Lett. **101**, 196803 (November 2008).

[114] B. Trauzettel, D.V. Bulaev, D. Loss, and G. Burkard, *Spin qubits in graphene quantum dots*, Nat. Phys. **3**, 192 (February 2007).

[115] C. Tao, L. Jiao, O.V. Yazyev, Y.C. Chen, J. Feng, X. Zhang, R.B. Capaz, J.M. Tour, A. Zettl, S.G. Louie, H. Dai, and M.F. Crommie, *Spatially resolving edge*

states of chiral graphene nanoribbons, Nat. Phys. **7**, 616 (May 2011).

[116] M. Pan, E.C. Girao, X. Jia, S. Bhaviripudi, Q. Li, J. Kong, V. Meunier, and M.S. Dresselhaus, *Topographic and Spectroscopic Characterization of Electronic Edge States in CVD Grown Graphene Nanoribbons*, Nano Lett. **12**, 1928 (April 2012).

[117] X. Zhang, O.V. Yazyev, J. Feng, L. Xie, C. Tao, Y.C. Chen, L. Jiao, Z. Pedramrazi, A. Zettl, S.G. Louie, H. Dai, and M.F. Crommie, *Experimentally Engineering the Edge Termination of Graphene Nanoribbons*, ACS Nano **7**, 198 (January 2013).

[118] O.V. Yazyev, *Emergence of magnetism in graphene materials and nanostructures*, Rep. Prog. Phys. **73**, 056501 (May 2010).

[119] J.B. Oostinga, B. Sacepe, M.F. Craciun, and A.F. Morpurgo, *Magnetotransport through graphene nanoribbons*, Phys. Rev. B **81**, 193408 (May 2010).

[120] D.V. Kosynkin, A.L. Higginbotham, A. Sinitskii, J.R. Lomeda, A. Dimiev, B.K. Price, and J.M. Tour, *Longi-*

tudinal unzipping of carbon nanotubes to form graphene nanoribbons, Nature **458**, 872 (April 2009).

[121] X. Yang, X. Dou, A. Rouhanipour, L. Zhi, H.J. Raeder, and K. Muellen, *Two-Dimensional Graphene Nanoribbons*, J. Amer. Chem. Soc. **130**, 4216 (April 2008).

[122] P. Nemes-Incze, G. Magda, K. Kamaras, and L.P. Biro, *Crystallographically Selective Nanopatterning of Graphene on SiO2*, Nano Res **3**, 110 (December 2009).

[123] B. Krauss, P. Nemes-Incze, V. Skakalova, L.P. Biro, K. Klitzing, and J.H. Smet, *Raman Scattering at Pure Graphene Zigzag Edges*, Nano Lett. **10**, 4544 (October 2010).

[124] B McCarroll and D.W. McKee, *The reactivity of graphite surfaces with atoms and molecules of hydrogen, oxygen and nitrogen*, Carbon **9**, 301 (1971).

[125] Z. Shi, R. Yang, L. Zhang, Y. Wang, D. Liu, D. Shi, E. Wang, and G. Zhang, *Patterning Graphene with Zigzag Edges by Self-Aligned Anisotropic Etching*, Adv. Mater. **23**, 3061 (July 2011).

[126] G. Dixon-Lewis, M.M. Sutton, and A. Williams, *The*

kinetics of hydrogen atom recombination, Disc. Faraday Soc. **33**, 205 (1962).

[127] K.E. Shuler and K.J. Laidler, *The Kinetics of Heterogeneous Atom and Radical Reactions. I. The Recombination of Hydrogen Atoms on Surfaces*, J. Chem. Phys. **17**, 1212 (December 1949).

[128] Y. Zhang, V.W. Brar, C. Girit, A. Zettl, and M.F. Crommie, *Origin of spatial charge inhomogeneity in graphene*, Nat. Phys. **5**, 722 (August 2009).

[129] R. Decker, Y. Wang, V.W. Brar, W. Regan, H.Z. Tsai, Q. Wu, W. Gannett, A. Zettl, and M.F. Crommie, *Local Electronic Properties of Graphene on a BN Substrate via Scanning Tunneling Microscopy*, Nano Lett. **11**, 2291 (June 2011).

[130] J. Xue, J. Sanchez Yamagishi, D. Bulmash, Ph. Jacquod, A. Deshpande, K. Watanabe, T. Taniguchi, Pablo Jarillo Herrero, and B.J. LeRoy, *Scanning tunnelling microscopy and spectroscopy of ultra-flat graphene on hexagonal boron nitride*, Nat. Mater. **10**, 282 (February 2011).

[131] Q.H. Wang, Z. Jin, K.K. Kim, A.J. Hilmer, G.L.C.

Paulus, C.J. Shih, M.H. Ham, J.D. Sanchez-Yamagishi, K. Watanabe, T. Taniguchi, J. Kong, P. Jarillo-Herrero, and M.S. Strano, *Understanding and controlling the substrate effect on graphene electron-transfer chemistry via reactivity imprint lithography*, Nature Chemistry **4**, 724 (August 2012).

[132] J. Sofo, A. Chaudhari, and G. Barber, *Graphane: A two-dimensional hydrocarbon*, Phys. Rev. B **75**, 153401 (April 2007).

[133] S. Engels, A. Epping, C. Volk, S. Korte, B. Voigtländer, K. Watanabe, T. Taniguchi, S. Trellenkamp, and C. Stampfer, *Etched graphene quantum dots on hexagonal boron nitride*, Appl. Phys. Lett. **103**, 073113 (August 2013).

[134] X. Du, I. Skachko, A. Barker, and E.Y. Andrei, *Approaching ballistic transport in suspended graphene*, Nat. Nanotechnol. **3**, 491 (July 2008).

[135] K.I. Bolotin, F. Ghahari, M.D. Shulman, H.L. Stormer, and Ph. Kim, *Observation of the fractional quantum Hall effect in graphene*, Nature **462**, 196 (November 2009).

[136] P. Rickhaus, R. Maurand, M.H. Liu, M. Weiss, K. Richter, and Ch. Schönenberger, *Ballistic interferences in suspended graphene*, Nature Communications **4**, 2342 (August 2013).

[137] B. Eren, D. Hug, L. Marot, R. Pawlak, M. Kisiel, R. Steiner, D.M. Zumbuhl, and E. Meyer, *Pure hydrogen low-temperature plasma exposure of HOPG and graphene: Graphane formation?*, Beilstein J. Nanotechnol. **3**, 852 (December 2012).

[138] Ch. Caillier, D.-K. Ki, Y. Lisunova, I. Gaponenko, P. Paruch, and A.F. Morpurgo, *Chemical species generated by high-vacuum ion gauges cause strong doping of graphene*, arXiv:1302.5318 (2013).

[139] A.S. Soltan, P. Jung, and A.A. Gadallah, *Resistivity and implantation distribution of hydrogen and helium in metals*, J. Phys. Condens. **4**, 9573 (July 1992).

[140] A.D. Hernandez-Nieves, B. Partoens, and F.M. Peeters, *Electronic and magnetic properties of superlattices of graphene/graphane nanoribbons with different edge hydrogenation*, Phys. Rev. B **82**, 165412 (October 2010).

[141] B. Eren, T. Glatzel, M. Kisiel, W. Fu, R. Pawlak,

U. Gysin, C. Nef, L. Marot, M. Calame, and Ch. Schönenberger, *Hydrogen plasma microlithography of graphene supported on a Si/SiO_2 substrate*, Appl. Phys. Lett. **102**, 071602 (February 2013).

[142] M.J. Schmidt and D. Loss, *Edge states and enhanced spin-orbit interaction at graphene/graphane interfaces*, Phys. Rev. B **81**, 165439 (April 2010).

[143] A.K. Geim and K.S. Novoselov, *The Rise of Graphene*, Nat. Mater. **6**, 183 (March 2007).

[144] O. Leenaerts, B. Partoens, and F.M. Peeters, *Hydrogenation of bilayer graphene and the formation of bilayer graphane from first principles*, Phys. Rev. B **80**, 245422 (December 2009).

[145] D. Boukhvalov, M. Katsnelson, and A. Lichtenstein, *Hydrogen on graphene: Electronic structure, total energy, structural distortions and magnetism from first-principles calculations*, Phys. Rev. B **77**, 035427 (January 2008).

[146] A.K. Singh and B.I. Yakobson, *Electronics and Magnetism of Patterned Graphene Nanoroads*, Nano Lett. **9**, 1540 (April 2009).

[147] Y.G. Zhou, X.T. Zu, F. Gao, J.L. Nie, and H.Y. Xiao, *Adsorption of hydrogen on boron-doped graphene: A first-principles prediction*, J. Appl. Phys. **105**, 014309 (January 2009).

[148] J. Bohdansky, J. Roth, and H.L. Bay, *An analytical formula and important parameters for low-energy ion sputtering*, Journal of Applied Physics **51**, 2861 (May 1980).

[149] Y. Yamamura and H. Tawara, *Energy dependence of ion-induced sputtering yields from monatomic solids at normal incidence*, Atomic Data and Nuclear Data Tables **62**, 149 (March 1996).

[150] Ziegler, J.F., 2006 SRIM-2006 computer code; online: http://www.srim.org.

[151] A.C. Dillon, K.M. Jones, T.A. Bekkedahl, C.H. Kiang, D.S. Bethune, and M.J. Heben, *Storage of hydrogen in single-walled carbon nanotubes*, Nature **386**, 377 (March 1997).

[152] A. Züttel, P. Sudan, Ph. Mauron, T. Kiyobayashi, Ch. Emmenegger, and L. Schlapbach, *Hydrogen storage in*

carbon nanostructres, Intern. J. Hyd. Energy **27**, 203 (February 2002).

[153] F. Lamari Darkrim, P. Malbrunot, and G.P. Tartaglia, *Review of hydrogen storage by adsorption in carbon nanotubes*, Intern. J. Hyd. Energy **27**, 193 (2002).

[154] T. Yildirim, O. Gülseren, and S. Ciraci, *Exohydrogenated single-wall carbon nanotubes*, Phys. Rev. B **64**, 075404 (July 2001).

[155] B.N. Khare, M. Meyyappan, A.M. Cassell, C.V. Nguyen, and J. Han, *Functionalization of Carbon Nanotubes Using Atomic Hydrogen from a Glow Discharge*, Nano Lett. **2**, 73 (January 2002).

[156] P. Ruffieux, O. Gröning, M. Bielmann, P. Mauron, L. Schlapbach, and P. Gröning, *Hydrogen adsorption on sp^2-bonded carbon: Influence of the local curvature*, Phys. Rev. B **66**, 245416 (December 2002).

[157] D. Neumann, G. Meister, U. Kürpick, A. Goldmann, J. Roth, and V. Dose, *Interaction of atomic hydrogen with the graphite single crystal surface*, Appl. Phys. A **55**, 489 (August 1992).

[158] A. Nikitin, H. Ogasawara, D. Mann, R. Denecke,

Z. Zhang, H. Dai, K. Cho, and A. Nilsson, *Hydrogenation of Single-Walled Carbon Nanotubes*, Phys. Rev. Lett. **95**, 225507 (November 2005).

[159] L. Hornekaer, Z. Sljivancanin, W. Xu, R. Otero, E. Rauls, I. Stensgaard, E. Laegsgaard, B. Hammer, and F. Besenbacher, *Metastable Structures and Recombination Pathways for Atomic Hydrogen on the Graphite (0001) Surface*, Phys. Rev. Lett. **96**, 156104 (April 2006).

[160] A.L. Thomann, P. Brault, B. Rousseau, and H. Estrade-Szwarckopf, *Stable C atom displacements on HOPG surface under plasma low-energy argon-ion bombardment*, Appl. Phys. A **77**, 591 (August 2003).

[161] F. Tuinstra and J.L. Koenig, *Raman Spectrum of Graphite*, J. Chem. Phys. **53**, 1126 (1970).

[162] A.C. Ferrari and J. Robertson, *Interpretation of Raman spectra of disordered and amorphous carbon*, Phys. Rev. B **61**, 14095 (May 2000).

[163] A.C. Ferrari, *Raman spectroscopy of graphene and graphite: Disorder, electron phonon coupling, doping*

and nonadiabatic effects, Solid State Com. **143**, 47 (April 2007).

[164] M. Neek Amal and F.M. Peeters, *Lattice thermal properties of graphane: Thermal contraction, roughness, and heat capacity*, Phys. Rev. B **83**, 235437 (June 2011).

[165] Y. Zhang, Z. Li, P. Kim, L. Zhang, and C. Zhou, *Anisotropic Hydrogen Etching of Chemical Vapor Deposited Graphene*, ACS Nano **6**, 126 (October 2012).

[166] C.P. Herrero and R. Ramirez, *Diffusion of hydrogen in graphite: a molecular dynamics simulation*, J. Phys. D, Appl. Phys. **43**, 255402 (June 2010).

[167] Z. Waqar, *Hydrogen accumulation in graphite and etching of graphite on hydrogen desorption*, J. Mater. Sci. **42**, 1169 (January 2007).

[168] D. Ugolini, J. Eitle, and P. Oelhafen, *Electron spectroscopy measurements on hydrogen implanted graphite and comparison to amorphous hydrogenated carbon films (a:CH)*, Appl. Phys. A **54**, 57 (January 1992).

[169] J.C. Lascovich, V. Rosato, and A. Santoni, *The study of the microscopic scale structure of carbon-based materials: a comparison between Auger-derived density of*

states structures and molecular dynamics simulations, Surf. Sci. **467**, 139 (2000).

[170] A. Allouche and Y. Ferro, *First principles study of electronic properties of hydrogenated graphite*, Phys. Rev. B **74** (December 2006).

[171] T. Takahashi, H. Tokailin, and T. Sagawa, *Angle resolved ultraviolet photoelectron spectroscopy of the unoccupied band structure of graphite*, Phys. Rev. B **32**, 8317 (December 1985).

[172] L. Diederich, Olivier M. Küttel, Eliane Schaller, and Louis Schlapbach, *Photoemission from the negative electron affinity (100) natural hydrogen terminated diamond surface*, Surface science **349**, 176 (1996).

[173] I.P. Barta, N. Garcia, H. Rohrer, H. Salemink, E. Stoll, and S. Ciraci, *A Study of Graphite Surface with STM and Electronic Structure Calculations*, Surf. Sci. **181**, 126 (March 1987).

[174] P. Ruffieux, M. Melle Franco, O. Gröning, M. Bielmann, F. Zerbetto, and P. Gröning, *Charge-density oscillation on graphite induced by the interference of electron waves*, Phys. Rev. B **71**, 153403 (April 2005).

[175] M. Wisse, B. Eren, L. Marot, R. Steiner, and E. Meyer, *Spectroscopic reflectometry of mirror surfaces during plasma exposure*, Rev. Sci. Instr. **83**, 013509 (January 2012).

[176] B. Eren, L. Marot, M. Langer, R. Steiner, M. Wisse, D. Mathys, and E. Meyer, *The effect of low temperature deuterium plasma on molybdenum reflectivity*, Nuclear Fusion **51**, 103025 (October 2011).

[177] M.J. Allen, V.C. Tung, L. Gomez, Z. Xu, L.M. Chen, K.S. Nelson, Ch. Zhou, R.B. Kaner, and Y. Yang, *Soft Transfer Printing of Chemically Converted Graphene*, Adv. Mater. **21**, 2098 (March 2009).

[178] J.D. Jones, K.K. Mahajan, W.H. Williams, P.A. Ecton, Y. Mo, and J.M. Perez, *Formation of graphane and partially hydrogenated graphene by electron irradiation of adsorbates on graphene*, Carbon **48**, 2335 (July 2010).

[179] S. Ono and K. Sugihara, *Theory of the Transport Properties in Graphite*, J. Phys. Soc. Japan **21**, 861 (1966).

[180] K. Sugihara and H. Sato, *Electrical Conductivity of Graphite*, J. Phys. Soc. Japan **18**, 332 (1963).

[181] H. Kempa, P. Esquinazi, and Y. Kopelevich, *Field In-*

duced Metal Insulator Transition in the c Axis Resistivity of Graphite, Phys. Rev. B **65**, 241101 (May 2002).

[182] T. Valla, P.D Johnson, Z. Yusof, B. Wells, Q. Li, S.M. Loureiro, R.J. Cava, M. Mikami, Y. Mori, M. Yoshimura, and T. Sasaki, *Coherence Incoherence and Dimensional Crossover in Layered Strongly Correlated Metals*, Nature **417**, 627 (June 2002).

[183] A.N. Lavrov, L.P. Kozeeva, M.R. Trunin, and V.N. Zverev, *Competition and coexistence of antiferromagnetism and superconductivity in* $RBa_2Cu_3O_6 + x$ *(R=Lu, Y) single crystals*, Phys. Rev. B **79**, 214523 (June 2009).

[184] S. Zhang, J. Park, V. Milner, and A.Z. Genack, *Photon Delocalization Transition in Dimensional Crossover in Layered Media*, Phys. Rev. Lett. **101**, 183901 (October 2008).

[185] D.M. Maslov, *Private communitcation.*

[186] To accommodate the wide range of sample heights, we take the upper plateau height plus 50 nm as the SiO_2 layer thickness. For the thickest samples, angle evapora-

tion was used additionally to ensure complete coverage of the edges.

[187] S. Tongay, J. Hwang, D.B. Tanner, H.K. Pal, D. Maslov, and A.F. Hebard, *Supermetallic Conductivity in Bormine-Intercalated Graphite*, Phys. Rev. B **81**, 115428 (March 2010).

[188] Producing samples in this range of thickness probably requires a fabrication technique other than exfoliation and presents further technical difficulties.

[189] In a dipstick, a calibrated Cernox chip thermometer was mounted directly adjacent to the sample, ensuring a very similar temperature. The dip stick was moved slowly between liquid ^{4}He and the room temperature top flange while continuously measuring both sample and thermometer, resulting in many points in T. Cool down and warm up curves were measured and compared, giving nearly identical results, and confirming the accuracy of this method. To obtain $\rho_c(T)$, we perform the correction following Eq. 7.1 at every temperature, using $\rho_{ab}(T)$.

[190] D.E. Soule, *Magnetic Field Dependence of the Hall Ef-*

fect and Magnetoresistance in Graphite single Crystals, Phys. Rev. **112**, 698 (November 1958).

[191] Y.B. Zhang, J.P. Small, W.V. Pontius, and P. Kim, *Fabrication and electric-field-dependent transport measurements of mesoscopic graphite devices*, Appl. Phys. Lett. **86**, 073104 (February 2005).

[192] J. Barzola Quiquia, J.L. Yao, P. Rödiger, K. Schindler, and P. Esquinazi, *Sample Size Effects on the Transport Characteristics of Mesoscopic Graphite samples*, Phys. Stat. Sol. A **205**, 2924 (December 2008).

[193] The SiO_2 spectrum is no longer visible for a graphite thickness $\gtrsim 50\,\mathrm{nm}$.

[194] G. Binnig, H. Fuchs, Ch. Gerber, H. Rohrer, E. Stoll, and E. Tosatti, *Energy-dependent state-density corrugation of a graphite surface as seen by scanning tunneling microscopy*, Euophys. Lett. **1**, 31 (January 1986).

[195] N. Tombros, A. Veligura, J. Junesch, J. van den Berg, P.J. Zomer, M. Wojtaszek, I.J. Vera Marun, H.T. Jonkman, and B.J. van Wees, *Large yield production of high mobility freely suspended graphene electronic de-*

vices on a polydimethylglutarimide based organic polymer, J. Appl. Phys. **109**, 093702 (May 2011).

[196] S. Kawai, T. Glatzel, S. Koch, B. Such, A. Baratoff, and E. Meyer, *Ultrasensitive detection of lateral atomic-scale interactions on graphite (0001) via bimodal dynamic force measurements*, Phys. Rev. B **81**, 085420 (February 2010).

[197] S. Lebegue, M. Klintenberg, O. Eriksson, and M. Katsnelson, *Accurate electronic band gap of pure and functionalized graphane from GW calculations*, Phys. Rev. B **79**, 245117 (June 2009).

[198] Silicon Materials, $1 - 5\,\mathrm{m\Omega hm}$ resistiviy, $295 \pm 15\,\mathrm{nm}$ oxide.

[199] Many thanks to Nico Minder, who designed the first grid and to Romain Maurand who thought of making a new, wafer scale grid.

[200] Nitto Denko Corporation, www.nitto.com, last visited: 13.10.2013.

[201] M. Moreno-Moreno, A. Castellanos-Gomez, G. Rubio-Bollinger, J. Gomez-Herrero, and N. Agrait, *Ultra-*

long Natural Graphene Nanoribbons and Their Electrical Conductivity, Small **5**, 924 (2009).

[202] Sylgard® 184, two component silicon elastomer: silicon elastomer and curing agent. www.dowcorning.com, last visited: 13.10.2013.

[203] K. Xu, P. Cao, and J.R. Heath, *Graphene Visualizes the First Water Adlayers on Mica at Ambient Conditions*, Science **329**, 1188 (September 2010).

[204] P. Blake, *Private communitcation.* (2010).

Curriculum Vitae

Dorothée Hug

Education

05.2009–12.2013	**PhD in experimental physics,** University of Basel, Department of Physics
09.2007–03.2009	**Master in Nanoscience,** Major in Physics, University of Basel, Switzerland
09.2004–05.2007	**Bachelor in Nanoscience,** University of Basel, Switzerland
08.1998–07.2003	**Highschool,** Gymnasium am Münsterplatz (GM) Basel, Switzerland

Publications

2014	**D. Hug**, S. Zihlmann, M. Rehmann, L. Marot and D. M. Zumbühl, *Defining Zigzag Edges in Single Layer Graphene with a Hydrogen Plasma*, in preparation
2013	L. Casparis, **D. Hug**, D. Koelbl and D. M. Zumbühl, arXiv:1301.2727v1
2012	B. Eren, **D. Hug**, L. Marot, R. Pawlak, M. Kisiel, R. Steiner, D. M. Zumbühl and E. Meyer, Beilstein J. Nanotech., **3**, 852–859 (2012)
2010	X. L. Liu, **D. Hug** and L. M. K. Vandersypen, Nano Lett., **10**, 1623 (2010)